
Doctoral


Science

2019

Microwave Synthesis and Characterisation of Zinc Sulfide Nanomaterials for Photocatalytic and Anti-Bacterial Applications

Damian W. Synnott
Technological University Dublin

Follow this and additional works at: <https://arrow.tudublin.ie/sciendoc>

 Part of the [Chemistry Commons](#)

Recommended Citation

Synnott, D.W. (2019) Microwave Synthesis and Characterisation of Zinc Sulfide Nanomaterials for Photocatalytic and Anti-Bacterial Applications, Doctoral Thesis, Technological University Dublin. DOI: 10.21427/4a98-z521

This Theses, Ph.D is brought to you for free and open access by the Science at ARROW@TU Dublin. It has been accepted for inclusion in Doctoral by an authorized administrator of ARROW@TU Dublin. For more information, please contact yvonne.desmond@tudublin.ie, arrow.admin@tudublin.ie, brian.widdis@tudublin.ie.



This work is licensed under a [Creative Commons Attribution-Noncommercial-Share Alike 3.0 License](#)

**Microwave Synthesis and Characterisation of Zinc Sulfide
Nanomaterials for Photocatalytic and Anti-Bacterial Applications**

By

Damian W. Synnott BSc (Hons)



A thesis submitted to the Technological University Dublin for the
award of Doctor of Philosophy

Supervised by:

Prof. Suresh C. Pillai

Dr. Michael K. Seery

This thesis is focused on the development of a novel ambient pressure microwave synthesis of ZnS based materials for photocatalytic and anti-bacterial technologies.

Chapter 1 introduces the problems with anti-biotic resistant bacteria and the impact that these species are causing within healthcare systems. One of the approaches to tackling these problems is the development of self-cleaning materials to replace the harsh cleaning agents currently in use to sterilize the surfaces of buildings and materials used in healthcare environments. Chapter 1 also introduces semiconductors, semiconductor photocatalysis and the mechanism of action, improving photocatalytic action and how to semiconductor photocatalysts have been used for anti-bacterial activities.

Chapter 1 discusses zinc sulfide and its various properties that make it attractive as a platform for photocatalytic materials with its wide band gap that can be modified to make it work in an indoor environment where UV light is not present.

Chapter 2 describes the synthesis techniques employed in developing ZnS and doped ZnS materials using an ambient pressure aqueous method. This chapter also explores the techniques employed to characterise the materials prepared by the microwave technique.

Chapter 3 covers to development of the ambient pressure aqueous microwave synthesis method including the variation of reagents, microwave irradiation power, irradiation time and volume of reagents and how these factors impacted the characteristics of the material. These characteristics include the crystallinity, size of the material, absorbance profile and its photocatalytic and antibacterial properties. The work of this chapter was published in *Applied Catalysis B: Environmental* in 2013 and was the subject of a talk which won the best Applied Chemistry talk at the Irish Universities Chemistry Colloquium at Queens University Belfast in 2010.

Chapter 4 is a study on effect of metal doping of the Group 13 metals – aluminium, gallium and indium – on ZnS. The optimum conditions for microwave synthesis established in chapter 3 were used with varying amounts of dopant levels to determine the optimum doping concentration to enhance the photocatalytic activity and antibacterial activity under indoor light conditions. Luminescence spectroscopy and X-ray photoelectron spectroscopy were employed to determine the mechanism of doping by the three different metals and the difference of the ionic radii of the metals was shown to affect how the metals interact with the ZnS crystal. The work of this chapter is prepared for publication and will be submitted in late 2018.

Chapter 5 presents a study of silver and indium co-doped ZnS prepared by microwave synthesis. The materials were characterised and shown to have a slight improved photocatalytic activity in comparison to indium doped ZnS and a greatly improved activity toward undoped ZnS prepared under the same conditions. There is also a study on the effect of silver doping concentrations on the crystallisation of ZnS and how the level of silver determines whether cubic blende or wurtzite phase material is formed. The work in chapter 5 was published in the *Nanotechnology* in 2013.

Declaration Page

I certify that this thesis which I now submit for examination for the award of Doctor of Philosophy, is entirely my own work and has not been taken from the work of others, save and to the extent that such work has been cited and acknowledged within the text of my work.

This thesis was prepared according to the regulations for graduate study by research of the Dublin Institute of Technology and has not been submitted in whole or in part for another award in any other third level institution.

The work reported on in this thesis conforms to the principles and requirements of the DIT's guidelines for ethics in research.

Signature _____ Date _____

Damian Synnott

Table of Contents

1 Introduction	1
1.1 Overview	2
1.1.1 Healthcare Associated Infections	2
1.1.2 Species of Concern	5
1.1.3 Prevention of Healthcare Associated Infections	8
1.2 Semiconductors	10
1.3 Semiconductor Photocatalysis	13
1.3.1 Mechanism of Photocatalysis	13
1.3.2 Anti-bacterial Properties of Semiconductor Photocatalysts	16
1.4 Improving Photocatalysis	17
1.4.1 Doping	17
1.4.2 Controlling the Size of the Photocatalyst	19
1.4.3 Reducing Recombination	20
1.5 Zinc Sulfide	21
1.5.1 Physical Properties of Zinc Sulfide	21
1.5.2 Band Structure of Zinc Sulfide	23
1.5.3 Applications of Zinc Sulfide	25
1.6 Synthesis Techniques	27
1.6.1 Hydrothermal	27
1.6.2 Solvothermal	28
1.6.3 Sol-gel	28
1.6.4. Chemical Precipitation	29
1.6.5 Template-Assisted Synthesis	29
1.7 Microwave Synthesis	30
1.7.1 The Electromagnetic Spectrum	30
1.7.2 Microwaves	33
1.7.3 Microwaves and Chemical Synthesis	35
1.8 Nanosized Versus Bulk Material	40
1.9 Project Hypothesis	42
2 Experimental Procedures and Characterisation Techniques	43
2.1 Materials	44
2.2 Equipment	44
2.3 Synthesis of the Semiconductor	45
2.3.1 Preparation of Zinc Sulfide	45
2.3.2 Preparation of Aluminium Doped Zinc Sulfide	47
2.3.3 Preparation of Gallium Doped Zinc Sulfide	47
2.3.4 Preparation of Indium Doped Zinc Sulfide	48
2.3.5 Preparation of Silver and Indium Co-Doped Zinc Sulfide	48
2.4 Characterisation Techniques	49
2.4.1 Powder X-ray Diffraction Analysis	49
2.4.2 X-ray Photoelectron Spectroscopy	50
2.4.3 UV-Visible Absorption Spectrometry (UV-Vis)	51
2.4.4 Transmission Electron Microscopy	52
2.4.5 Field Emission Scanning Electron Microscopy	53
2.4.6 Luminescence Spectroscopy	54

2.4.7 BET Specific Surface Area Analysis	54
2.4.8 Raman Spectroscopy	55
2.5 Photocatalytic Testing	56
2.5.1 Methylene Blue Degradation	56
2.6 Anti-bacterial Testing	58
2.6.1 Agar Test Method	58
2.6.2 Suspension Test	59
3 Preparation and Characterisation of Microwave-Assisted Synthesised Zinc Sulfide	60
3.1 Introduction	61
3.2 Microwave Synthesis	62
3.3 Characterisation	64
3.3.1 X-ray Diffraction	64
3.3.2 Scanning Electron Microscopy	67
3.3.3 Transmission Electron Microscopy	68
3.3.4 X-ray Photoelectron Spectroscopy	69
3.3.5 Diffuse Absorbance and Luminescence	71
3.3.6 Photocatalytic Testing	76
3.3.7 Antibacterial Testing	80
3.4 Conclusion	88
4 Group 13 metal doped ZnS	90
4.1 Introduction	91
4.2 Photocatalyst Synthesis	95
4.3 Characterisation	96
4.3.1 X-ray Diffraction	96
4.3.2 Diffuse Absorbance	99
4.3.3 Photoluminescence	102
4.3.4 Surface Area Analysis	104
4.3.5 X-ray Photoelectron Spectroscopy	106
4.3.6 Photocatalytic Activity	110
4.3.7 Anti-bacterial Study	112
4.4 Temperature Study	115
4.5 Conclusions	122
5 Silver and Indium co-doped ZnS	123
5.1 Introduction	124
5.2 Characterisation	126
5.2.1 X-ray Diffraction	127
5.2.2 X-ray Photoelectron Spectroscopy	128
5.2.3 Scanning Electron Microscopy	130
5.2.4 Optical Characterisation	132
5.3 Photocatalysis Testing	135
5.4 Role of Silver in Phase Change	137
5.5 Anti-bacterial Activity	140
5.6 Conclusions	142
6 Future Work	143
Publications and Presentations by the Author	151
References	152

List of Figures

Figure 1.1 Diagram of the band structure of conductors, semiconductors and insulators where E_g represents the band gap	10
Figure 1.2 Schematic representation of semiconductor photocatalysis showing the generation of ROS at the conduction and valence bands and degradation of pollutant molecules	13
Figure 1.3 Diagram of (a) p-type semiconductor, (b) n-type semiconductor	17
Figure 1.4 Model showing (a and b) the handedness of the fourth interatomic bond, (c and d) the respective eclipsed and staggered dihedral conformations and (e and f) the atomic arrangement along the close packing axis	22
Figure 1.5 Band potentials of wide band gap semiconductors	24
Figure 1.6 The electromagnetic spectrum showing its component parts separated by wavelength and frequency	30
Figure 1.7 Schematic view of the interior of a magnetron	34
Figure 1.8 Mechanism of heating of water by microwave irradiation	39
Figure 2.1 Chemical Structure of Methylene Blue	56
Figure 2.2 Schematic diagram of the anti-bacterial agar test method	58
Figure 3.1 X-ray diffraction patterns of ZnS prepared at 150 W irradiation power at different irradiation times and precursor concentration	64
Figure 3.2 X-ray diffraction patterns for samples ZnS300-30-02, ZnS450-20-01, ZnS600-30-02 and ZnS720-15-02	65
Figure 3.3 Scanning electron microscope image of ZnS450-40-02	67
Figure 3.4 (a) and (b) TEM images of ZnS720-30-01 and (c) and (d) HRTEM images of ZnS600-30-02	68
Figure 3.5 X-ray photoelectron spectra of (a) S 2p, (b) Zn 2p ₁ , (c) Zn 2p ₃ peaks of ZnS450-20-01	70
Figure 3.6 XPS survey scan of ZnS450-20-01	71
Figure 3.7 Diffuse absorbance spectra of (A) ZnS300-60-01 (B) ZnS450-40-01 and (C) ZnS600-30-02	73
Figure 3.8 Luminescence spectra of ZnS450W excited at 275 nm	74
Figure 3.9 Schematic energy level diagram of microwave prepared ZnS	75
Figure 3.10 Emission spectrum of the 60 W light bulb used for the photocatalysis and anti-bacterial studies	76
Figure 3.11 Absorbance spectra of methylene blue in the presence of ZnS720-15-02 over 2 hours	79
Figure 3.12 Comparison of blanks and a selection of ZnS samples degradation rates	79
Figure 3.13 Petri dishes of (a) blank agar plate inoculated with E. coli and S. aureus exposed to light and (b) blank agar plate inoculated with E. coli and S. aureus not exposed to light	82
Figure 3.14 Petri dishes of (a) Sigma-Aldrich ZnS agar plate inoculated with E. coli and S. aureus to light and (b) Sigma-Aldrich ZnS agar plate inoculated with E. coli and S. aureus not exposed to light	82
Figure 3.15 Petri dishes of (a) TiO ₂ agar plate inoculated with E. coli and S. aureus exposed to light and (b) TiO ₂ agar plate inoculated with E. coli and S. aureus not exposed to light and (c) different exposure of TiO ₂ agar plate inoculated with E. coli and S. aureus exposed to light to enable visualisation of bacteria which is similar in colour to the titanium dioxide	83

Figure 3.16 Petri dishes of (a) ZnS300-30-02 agar plate inoculated with E. coli and S. aureus exposed to light and (b) ZnS300-30-02 agar plate inoculated with E. coli and S. aureus not exposed to light	84
Figure 3.17 Bacterial concentration of reference and ZnS300W sample to test the degradation rate of the photocatalyst	86
Figure 4.1 X-ray diffraction patterns of ZnS and aluminium doped ZnS prepared by microwave synthesis	96
Figure 4.2 X-ray diffraction patterns of ZnS and gallium doped ZnS prepared by microwave synthesis	97
Figure 4.3 X-ray diffraction patterns of ZnS and indium doped ZnS prepared by microwave synthesis	97
Figure 4.4 UV-Vis diffuse absorbance spectra of ZnS and Al-ZnS samples prepared by microwave synthesis	99
Figure 4.5 Diffuse absorbance spectra of ZnS and gallium doped ZnS prepared by microwave synthesis	100
Figure 4.6 Diffuse absorbance spectra of ZnS and indium doped ZnS prepared by microwave synthesis	101
Figure 4.7 Emission spectra of (a) ZnS600-30-02 and (b) 0.2 % In-ZnS (c) 0.4 % In-ZnS (d) 0.8 % In-ZnS (e) 1 % In-ZnS and (f) 2 % In-ZnS	103
Figure 4.8 XPS spectra for 2 % In – ZnS (A) Zn 2p ₁ peak (B) Zn 2p ₃ peak (C) S 2p peak and (D) In 3d peaks	109
Figure 4.9 Photocatalytic degradation of methylene blue under irradiation from a 60 W bulb in the presence of 0.4 % In doped ZnS	111
Figure 4.10 X-ray diffraction patterns of 2 % Al – ZnS calcined at 200, 400 and 600 °C for 2 h (# = ZnO wurtzite peak, * = ZnS sphalerite peak)	115
Figure 4.11 X-ray diffraction patterns of 2 % Ga – ZnS calcined at 200, 400, 500 and 600 °C for 2 h (# = ZnO wurtzite peak, * = ZnS sphalerite peak)	116
Figure 4.12 X-ray diffraction patterns of 2 % In – ZnS calcined at room temperature, 200, 400 and 600 °C for 2 h (# = ZnO wurtzite peak, * = ZnS sphalerite peak)	117
Figure 4.13 Photocatalytic degradation of methylene blue under irradiation from a 60 W light bulb in the presence of 0.8 % In ZnS calcined at 400 °C	120
Figure 4.14 Photocatalytic degradation of methylene blue under irradiation from a 60 W light bulb in the presence of 0.4 % Ga ZnS calcined at 600 °C	121
Figure 5.1 X-ray diffraction patterns of (a) ZnS (b) 1 % Ag – ZnS (c) 2 % Ag – ZnS (d) 4 % Ag – ZnS and (e) 8 % Ag – ZnS	127
Figure 5.2 X-ray photoelectron spectrum of Ag-3d for 4 % Ag – 0.4 % In ZnS	129
Figure 5.3 SEM images of (A) 0.4 % Ag – 0.4 % In ZnS and (B) 8 % Ag – 0.4 % In ZnS	131
Figure 5.4 Diffuse absorbance spectra of (A) 0.4% Ag 0.4% In ZnS, (B) 1% Ag – 0.4 % In ZnS, (C) 2% Ag – 0.4% In ZnS, (D) 4% Ag – 0.4% In ZnS and (E) 8% Ag – 0.4% In ZnS	133
Figure 5.5 Emission spectra of (A) 0.4 % Ag – 0.4 % In ZnS and (B) 8 % Ag – 0.4 % In ZnS	134
Figure 5.6 Proposed band structure of ZnS with the defects caused by zinc and sulfur vacancies acting as donor levels in the band gap	135
Figure 5.7 XRD spectra of (A) 2% Ag-0.4% In ZnS, (B) 2% Ag-0.4% In ZnS calcined at 400 °C, (C) 2% Ag - 0.4% In ZnS calcined at 500 °C and (D) 2% Ag – 0.4% In ZnS calcined at 600 °C	138

Figure 5.8 X-ray diffraction pattern of ZnS samples doped with silver at varied amounts	139
Figure 6.1 General view of a semiconductor-semiconductor heterojunction	146
Figure 6.2 Example of XRD data of a ZnS/Bi ₂ S ₃ heterojunction prepared in the microwave at 600 W for a period of 10 and 20 min	146
Figure 6.3 Structure of Delafossite material demonstrated with CuAlO ₂	148
Figure 6.4 X-ray diffraction patterns for AgInO ₂ and AgGaO ₂ and combinations of In and Ga in the B position for delafossites	149

List of Tables

Table 1.1 Physical properties of zinc sulfide	21
Table 1.2 Polar and non-polar solvents with their boiling points and dielectric constants	38
Table 2.1 Sample preparation of ZnS	46
Table 3.1 Estimated particle size from Z-ray diffraction and miller indices calculations for ZnS prepared by microwave synthesis	66
Table 3.2 Absorption edge and band gaps of ZnS prepared by microwave heating at different power, irradiation time and precursor concentrations	72
Table 3.3 Photocatalytic rate of half life of methylene blue in the presence of ZnS prepared by microwave heating at different power, irradiation time and precursor concentrations	78
Table 3.4 Anti-bacterial results of ZnS300-30-02 and controls	81
Table 3.5 Concentration of the bacterial suspension test for the reference and test samples	85
Table 4.1 Physical and chemical properties of the Group 13 metals	93
Table 4.2 Surface area of photocatalysis as calculated from BET analysis	106
Table 4.3 Binding energies for XPS analysis of indium doped samples	110
Table 4.4 Photocatalytic degradation rate of methylene blue under irradiation from a 60 W light bulb in the presence of the photocatalysts	110
Table 4.5 Anti-bacterial activity of aluminium doped ZnS samples	112
Table 4.6 Anti-bacterial activity of gallium doped ZnS samples	113
Table 4.7 Anti-bacterial activity of indium doped ZnS samples	114
Table 4.8 Photocatalytic rates of group 13 metal doped ZnS samples pre-calcined at room temperature, 200 °C, 400 °C and 600 °C	118
Table 5.1 X-ray photoelectron binding energies for silver and indium co-doped samples	130
Table 5.2 Photocatalytic rates of microwave prepared ZnS and standard samples	137
Table 5.3 Anti-bacterial testing results for silver and indium codoped ZnS and controls	140

1. INTRODUCTION

1.1 Overview

1.1.1 Healthcare Associated Infections

There is an increasing need worldwide for the application and development of low cost materials and technologies to decrease the burden of illness related to infectious diseases caused by airborne¹, waterborne² and surface residing bacteria³. This is especially a problem where people are immuno-compromised in places such as hospitals and other healthcare facilities. Healthcare associated infections, HAIs are a major source of concern across the globe with two million infections, leading to ninety thousand deaths occurring annually in the United States alone.^{4,5}

In Ireland the HSE has calculated that over 8,000 patients acquire a HAI annually at a cost of €118 million. This figure is estimated based the cost of extra hospital days, estimated between 117,552 and 411,432 days and extra deaths of between 1,081 and 3,820 annually. There is also an associated cost of lost productivity and ongoing healthcare needs following release from the healthcare facility.⁶

The European Centre for Disease Control (ECDC) monitors the levels of bacterial infection in Europe and reports each year on the level of infections and the percentage of infections caused by anti-microbial resistant bacterium. Anti-microbial resistance can be present from when anti-microbial compounds are first introduced depending on the mechanism of action. Alternatively resistance can be gained over time which can be an issue with the overuse of antibiotics. The resistance can be gained by;

- Mutational modification of anti-microbial targets such as topoisomerases and ribosomal proteins
- Mutational loss of outer membrane proteins preventing uptake of anti-microbial agents
- Mutational up-regulation of efflux systems in the bacteria

- Acquisition of plasmid-mediated resistive genes

The current guidelines for prevention of infections, especially those from anti-microbial resistant pathogens include screening and other infection prevention and control measures. Screening involves patient isolation and contact precautions including hand washing before and after contact with patients and their environments. A study in Scotland conducted in 2009 found that 3.9% of all patients admitted to hospitals were colonised with Methicillin-Resistant *Staphylococcus aureus* (MRSA) and only about half of these could be isolated due to either short-term stays or lack of isolation units.⁷ The other infection prevention and control measures include education, monitoring, preventing overcrowding, adequate staff levels, hand hygiene and the use of personal protective equipment (PPE). The guidelines also state that all hospital surfaces should be made of a durable, washable material.⁸

The patient environment is an important factor in controlling infection and the spread of pathogens. A recent Irish study has shown that some HAIs are spread *via* droplets, rather than an airborne transmission route and these droplets can survive on surfaces. One particular outbreak of MRSA occurred in a maternity ward as patients changed their babies due to the changing table being the source of the infectious bacteria. Dry conditions with dust on environmental surfaces act as reservoirs for MRSA, which facilitates the transfer to hands when such surfaces are touched. Conversely, MRSA acquired on hands and gloves may be transferred to the environmental surfaces and equipment they come into contact with, for example, curtains, monitoring equipment, switches/buttons, phones, touch panel screens, door handles, light switches, bed tables, bed rails, mattresses and even pens. Studies have shown that in hospital environments beds, lockers and over-bed tables are the most contaminated surfaces. A 2011 Canadian

study showed that 11.8% of surfaces sampled were positive for MRSA – including chair backs, hand rails, isolation carts and sofas.

Work in the early 2000's on controlling the spread of MRSA and increased protocols and education have led to a decrease in the overall incidents of MRSA. In Europe between 2003 and 2013, there was a decrease in the total percent of infections from MRSA of 41% to 20%. However, alongside this decrease there has been an increase in other anti-microbial resistant species emerging. Among these species of concern is the increase in the number of infections caused by anti-biotic resistant gram negative bacteria including *E. coli*, *K. pneumoniae*, *P. aeruginosa* and species from the *Acinetobacter* and the *Enterococcus* genus.

The ECDC estimate that infections caused by drug-resistant bacteria to be about 25,000 per annum and cost an extra 1.5 billion euro in extra healthcare costs and lost productivity.

1.1.2 Species of Concern

The ECDC along with state labs and hospitals across Europe currently monitor 7 bacterial species.

1) *Staphylococcus aureus*

S. aureus is a gram-positive bacterium that commonly colonises the skin and nose and is found on ~ 30% of healthy humans. In certain circumstances *S. aureus* can cause bloodstream infections (BSI), infective endocarditis, pneumonia, skin and soft tissue infections (SSTI), and bone and joint infection. The methicillin-resistant form (MRSA) was one of the first and most important anti-microbial resistant bacteria species and today is the most common healthcare associated infection and reports show that there is an increase worldwide in the levels of MRSA seen in healthcare systems between the 1990's and early 2000's.^{9,10,11,12,13}

Beta-Lactam anti-biotics such as flucloxacillin, are the most common anti-microbials used to treat infections of *S. aureus*. Methicillin, a beta-lactam class anti-biotic was developed by Beechams in 1959 and the first case of Methicillin resistant *S. aureus* was identified in 1961. Methicillin is no longer clinically available but all *S. aureus* resistant to anti-biotics based on the beta-lactam ring are referred to as MRSA.

2) *Escherichia coli*

E. coli is a gram negative bacterium most frequently isolated from bloodstream cultures and is one of the most common causes of bloodstream infections and healthcare associated infections-urinary tract infections (HAI-UTIs). In Europe in 2013, more than half of the *E. coli* isolates reported were found to be resistant to anti-microbials including aminopenicillins and fluoroquinolones. This follows a trend in recent years of

an increasing frequency of infections caused by anti-biotic resistant *E. coli*. The ECDC recommends the prudent use of anti-microbials to halt this trend.

3) *Pseudomonas aeruginosa*

P. aeruginosa is a non-fermenting gram-negative bacterium that is ubiquitous in aquatic environments. *P. aeruginosa* is an opportunistic pathogen and is a major cause of infection in hospitalised patients who are immuno-compromised or immuno-deficient. It commonly causes hospital-acquired pneumonia, bloodstream infections and urinary tract infections. *P. aeruginosa* is an enormously versatile organism and it has an intrinsic tolerance to detergents, disinfectants and anti-microbial compounds and this all results in the difficulty in controlling *P. aeruginosa* in the hospital environment. This has led to significantly increasing numbers of infections in Irish hospitals between 2010 and 2013.

4) Acinetobacter species

Acinetobacter is a genus of gram negative aerobic bacteria. There a large number of species within the genus and while they are an important organism in soil, they can survive on both wet and dry surfaces, such as those found in hospitals including medical devices due to their ability to form biofilms. The species are opportunistic pathogens and are known to cause pneumonia, blood stream infections and urinary tract infections.

5) *Streptococcus pneumonia*

S. pneumonia is a gram-positive anaerobic bacterium and it is a significant human pathogen. In healthy carriers it resides in the respiratory tract, the sinuses and the nasal cavity but in people who are immuno-compromised or immuno-deficient it can cause a wide range of disease. It has been identified as the most common cause of pneumonia, a major cause of meningitis in the young and old and a major cause of septicaemia in

HIV-infected people. There are over 90 different serotypes known of *S. pneumonia* and each has different virulence and resistance to anti-microbial agents. The trend in recent years for an increasing number of infections is caused by anti-microbial resistant serotypes brought on by the overuse of anti-biotics.

6) *Klebsiella pneumonia*

K. pneumonia is a gram-negative bacteria species which while normally found in humans on the skin and in the mouth, causes major health problems if it is aspirated into the lungs. Once in the lungs it can damage the organs by inflammation, necrosis and the production of thick, bloody, mucoid sputum. Outside of the lungs, it can cause pneumonia and infections of the blood, and of surgical sites. Due to the rise of infections caused by anti-bacterial strains of *K. pneumonia* in Europe, it has recently been added to the ECDC's list of infectious diseases monitoring list. The resistance pathways have been identified by *K. pneumonia*'s ability to produce extended-spectrum beta-lactamases which are enzymes which inhibit the activity of the beta-lactam based anti-biotics.

7) *Enterococci*

Enterococcus is a genus of gram positive bacteria, which are a normal part of the gastrointestinal tract. Infections from *Enterococcus*, especially two of the species of the genus (*E. faecalis* and *E. faecium*) have in the last few years been on the increase and have been shown to cause a wide variety of diseases including intra-abdominal abscesses and blood stream infections. *Enterococcus* species have an intrinsic resistance to certain anti-biotics such as the beta-lactum family of anti-biotics and aminoglycosides. Antibiotics traditionally used to treat *Enterococcus* infections such vancomycin and avoparcin have been recently become less effective. This is ascribed to

the overuse of these glycopeptides antimicrobials in hospitals and to their use as growth promoters in animal husbandry.

1.1.3 Prevention of Healthcare Associated Infections

In Ireland, there are approximately eight thousand cases of HAIs a year, of which MRSA accounts for 75% of these.¹⁴ In Irish hospitals preventative measures for treating HAIs are based on extensive cleaning regimens, at an estimated cost of 68 million euro per annum. In the United States, the cost of treating a patient with a bloodstream infection was estimated at forty thousand dollars to the hospital alone.⁵

Anti-bacterial technologies have been produced and tested previously, notably the commercially available products based on the synthetic chemical Triclosan or 2,2,4'-trichloro-2'-hydroxydiphenylether. Health and safety concerns with this material including skin irritation, dioxin production and bacterial resistance has led to Triclosan being 'notified' under the EEC Biocidal Directive (98/8/EC). Silver based materials are also available in the marketplace including paints like Sterishield™ from ICI Dulux and other products containing nano-sized silver including plasters and sandwich boxes. As the anti-bacterial activity of silver containing materials is short-term due to the leeching of the silver, their application is more suited to products with a relatively short life-span requirement such as plasters, bandages and cleaning wipes.

Semiconductor photocatalysis provides an alternative method for the deactivation of bacteria and has the advantages of a longer time span in which the material is active, the final degradation products are non-pathogenic and that HAI causing bacteria will not develop a resistance to the oxidising agents produced on the surface of the semiconductor photocatalyst.

The main focus of my work centres on two topics. The first topic is the development of a low cost, relatively quick synthesis method for producing zinc sulfide (ZnS) which has the capability to work as semi-conductor photocatalyst in an indoor environment and has the ability to degrade bacteria producing a sterile environment.

A secondary area of interest regarding ZnS is to look at improving the photocatalytic activity of the material using metal doping. Metal dopants can improve on the photocatalytic activity by reducing the recombination rate of the electron hole pair, inserting a band directly into the band gap of the semiconductor and by introducing defects into the crystal.

Reaction times of eight hours using hydrothermal heating are typically the way ZnS is produced and this body of work proposes reducing the reaction time down to less than 30 minutes using an ambient pressure microwave reaction system. The microwave synthesis method produces ZnS nanomaterials which are photocatalytically active under indoor light irradiation. The photocatalytic activity is also improved by the addition of Group 13 metal dopants to the ZnS system.

1.2 Semiconductors

A semiconductor is a material which has an electrical conductivity that falls between that of a metal and an insulator as shown in figure 1.1. Electrical conductivity arises from the ability of electrons to move between unoccupied regions in the bands of the atom or compound. Only electrons in energy levels near the Fermi level, the hypothetical energy level of an electron, are free to move around. In metals, the Fermi level lies inside at least one band and metals have a high electrical conductivity and are therefore conductors. In materials that act as insulators there is a gap between two bands and the Fermi level lies in the band gap and therefore the energy required for an electron to transition from the highest occupied molecular orbital (HOMO) in the valence band to the lowest unoccupied molecular orbital (LUMO) in the conduction band is greater than the energy supplied thermally or by light. Insulators therefore have a low electrical conductivity and materials that act as insulators include glass, rubber and most plastics.

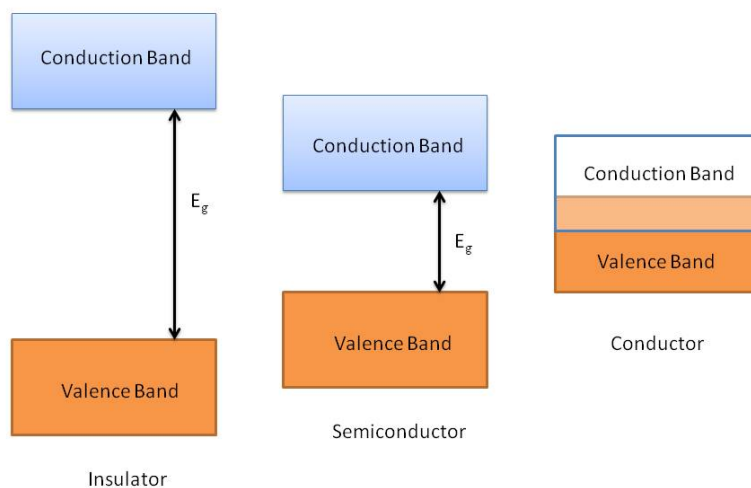


Fig 1.1 Diagram of the band structure of conductors, semiconductors and insulators

where E_g represents the band gap

In a semiconductor, the Fermi level also lies in the band gap but the band gap is smaller than that in an insulator and so the energy required for an electron to transition between the valence band and the conduction band can be overcome by excitation using electromagnetic irradiation.

The properties of semiconductor materials were first observed by Michael Faraday in the early 19th century when experimenting on materials and their electrical properties it was noticed that the electrical resistance (inverse of electrical conductivity) was reduced in silver sulfide as the material was heated.¹⁵ It was well known that in metals and other good conductors that electrical conductivity decreases at higher temperatures. This property, despite the increase in excited electrons moving into unoccupied orbitals, is due to increased collisions between the electrons and atoms at higher temperatures and so the electrons being scattered from their paths are less efficient charge carriers.¹⁶

The population, P , of electrons in orbitals is described by the Fermi-Dirac distribution

$$P = \frac{1}{1 + e^{(E-\mu)/kT}} \quad \text{Equation 1.1}$$

Where μ is the chemical potential which is the energy level for which $P = 1/2$, i.e. the Fermi level in metals. As seen in equation 1.1 the chemical potential decreases as the T , temperature, increases.

In the 19th century there were a number of other observations arising from semi-conducting materials that could not be explained including the observation of voltage between a solid and liquid electrode when irradiated by light, decreased resistance in selenium when exposed to light and conduction and rectification in metal sulfides. Following the discovery of the electron in 1897 by J.J. Thomson there were a number of theories developed to explain the movement of electrons and charge carriers in solid materials. In 1914, Johan Koenigsberger classified solid materials as metals, insulators

and variable conductors. In the early 1930s band theory and the theory of band gaps were developed by Alan Herries Wilson, a mathematician working at Cambridge University. During World War II, research and development in semiconductors advanced rapidly with the manufacture of increasingly pure materials and the development of semiconductor crystals for use in radar and communication devices at the forefront. Today, semiconductors are the backbone of the modern electronics with development of technologies based on silicon and other semiconductors worth many trillions of dollars. Semiconductors have a wide range of uses outside of the silicon in all computers including light-emitting diodes, photovoltaic solar cells, sensors, thermometers and as photocatalysts.

1.3 Semiconductor Photocatalysis

1.3.1 Mechanism of Photocatalysis

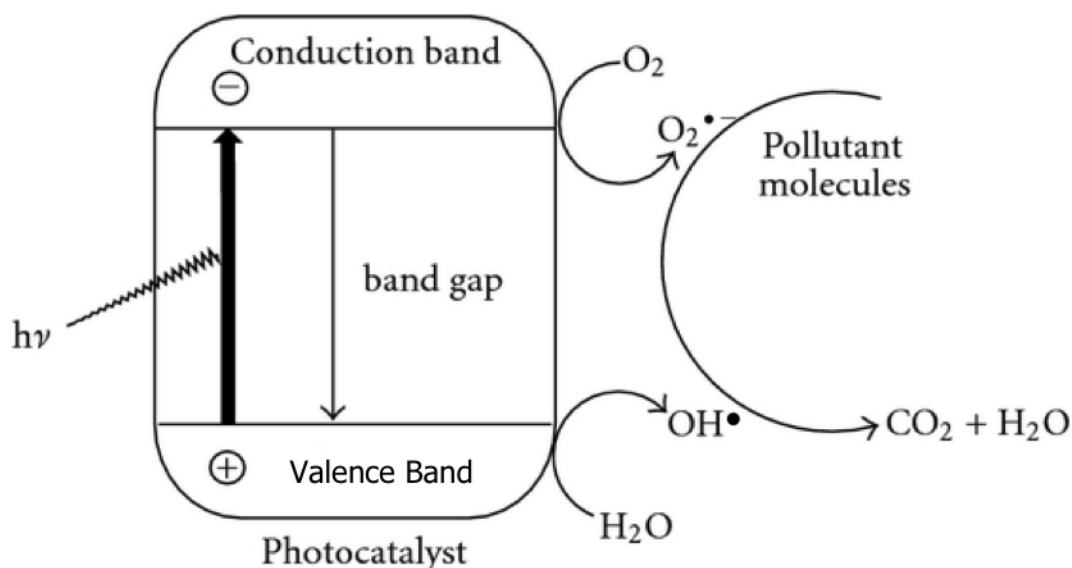


Fig. 1.2 Schematic representation of semiconductor photocatalysis showing the generation of ROS at the conduction and valence bands and degradation of pollutant molecules

Figure 1.2 shows the mechanism of semiconductor photocatalysis and the generation of hydroxyl radicals and other reactive oxygen species. Upon irradiation with a photon of light equal to or greater than the band gap of the semiconductor, an electron is promoted from the valence band to the conduction band.^{1,17} The vacancy left by the electron in the valence band is a positive hole and so an electron-hole pair is formed in the semiconductor. The excited electron-hole pair can recombine and the energy dissipated as heat. The electron or hole can migrate to the surface of the semiconductor preventing recombination. The photo-generated electrons and holes that migrate to the surface react with water and oxygen to produce various reactive oxygen species (ROS) such as hydroxyl radicals ($\bullet OH$), superoxide anions ($O_2^{\bullet-}$) and hydrogen peroxide (H_2O_2).

The mechanism for the generation of these reactive species is given in equations 1.2 – 1.9



The schemes shown in equations 1.2 – 1.8 shows the formation of hydroxyl radicals formed by the electron promoted to the conduction band. Molecular oxygen reacts with the electron to form a superoxide radical ($\text{O}_2^{\bullet -}$). The superoxide radical reacts with the hydrogen ion produced in water to form another radical $\text{HOO}\bullet$ which can further react with the oxygen radical and then hydrogen ions to form hydrogen peroxide, H_2O_2 . Hydrogen peroxide, a powerful oxidising species itself can react with conduction band electrons to form hydroxyl radicals which are adsorbed on the surface of the photocatalyst.

Hydroxyl radicals are also formed at the positive hole left in the valence band through equations 1.9 and 1.10.

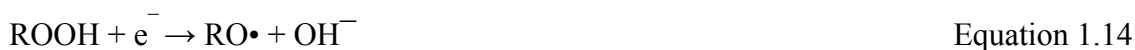


These hydroxyl radicals are formed by the oxidation of water and adsorbed hydroxide ions on the surface by the positive holes in the valence band.

The hydroxyl radicals can degrade organic pollutants, gases and bacterial species. The indirect oxidation of organic pollutants is shown in equations 1.11 – 1.13



The electrons that are promoted to the conduction band can also be transferred directly to pollutants on the surface of the catalyst and reduce the compound as in the case of carboxylic acids and in the dechlorination of polyhalogenated benzene rings.⁴⁴



The positive hole in the valence band can also directly oxidise organic pollutants as in equation 1.15



1.3.2 Anti-bacterial Properties of Semiconductor Photocatalysts

Since the first report of photo-induced cleavage of water using titanium dioxide electrodes by Fujishima *et al.*¹⁸ efforts have been made to develop a method to purify air and water using semiconductor photocatalysts have been undertaken. In general, antibacterial agents inactivate cell viability but pyrogenic and toxic ingredients such as endotoxins remain after the bacteria have been killed. Endotoxins cause critical problems in medical facilities because even at low concentrations they can elicit endotoxin activities such as pyrogenicity and lethal toxicity. Semiconductor photocatalysts have an advantage over other anti-bacterial agents, such as silver, in that not only can the bacteria be deactivated but the photocatalyst can degrade the organic compounds leached from the cell of the bacteria.¹⁹ Sunada *et al.*¹⁹ showed that when *E. coli* inactivation occurs, the concentration of endotoxin increases indicating that the TiO₂ destroys the outer membrane of the *E. coli* cell. Typically for the removal of endotoxins adsorbed on solid materials, a thermal treatment at 250 °C for 30 minutes is required or a chemical treatment with ethanol containing sodium hydroxide. Photocatalysts offer a much simpler route.

There are a number of theories on the mechanism of degradation of bacteria by semiconductor photocatalysis. The most popular is the degradation of the outer membrane of the bacterium by the reactive oxide species produced on the surface of the photocatalyst. The outer membrane is disrupted allowing the reactive oxygen species to cross the peptidoglycan layer and disrupt the internal cells of the bacteria. This leads to the cells death and ultimately leeching of the internal structures and compounds from the bacteria. These compounds will ultimately be degraded by the photocatalyst to the final degradation compounds, water and carbon dioxide.

1.4 Improving Photocatalysis

1.4.1 Doping

There are two types of doping that occurs within the band structure of the semiconductor (see figure 1.3). P-type doping occurs when a dopant with fewer electrons than the host material and positive holes are added to above the valence band of the semiconductor. N-type doping occurs when a dopant with more electrons than the host material is added to host and a dopant band exists below the conduction band of the semiconductor material.

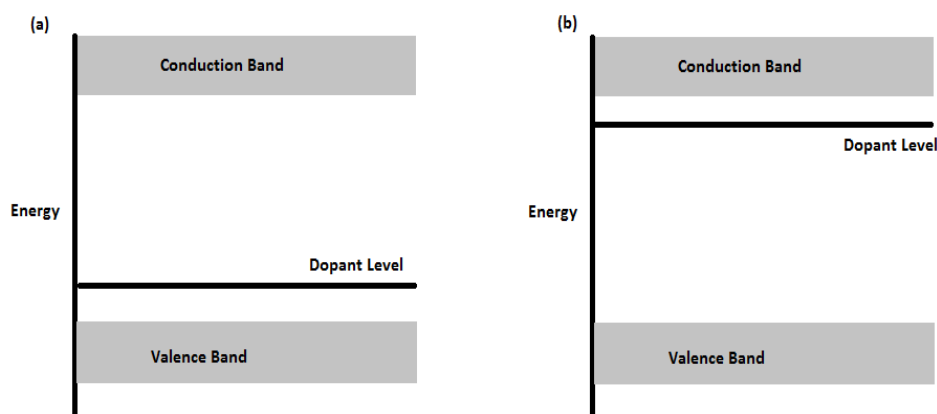


Fig 1.3 Diagram of (a) p-type semiconductor, (b) n-type semiconductor

For improvement of photocatalytic activity, dopants, both metal and non metal serve a number of functions. One of the main aims of doping is to reduce the effective band gap of metal oxide and metal sulfide semiconductors. In doped materials, an electron from the dopant ion can be excited to the conduction band of the semiconductor. An optimum dopant level must be established as an excess of metal ion doping can act as a recombination site and reduce the photocatalytic activity of the semiconductor. The band gap of ZnS, 3.7 eV for the cubic blende structure and 3.8 eV for the wurtzite

structure,^{41,42} equating to absorption edges of 335 nm and 326 nm which means that excitation of an electron from the valence band to the conduction band only occurs in the UV light region of the electromagnetic spectrum.

Doped ZnS materials have been studied since 1994 when Bhargava *et al.*²⁰ reported that Mn²⁺ doped ZnS could yield both high quantum luminescence efficiency and lifetime shortening. The wide band gap of ZnS allows it to be a good host material and metal doping has been used to change the optical and electronic properties allowing ZnS to be used in a wider range of applications.²¹ Doping with transition-metals or rare-earth elements has often been used to prepare phosphor ZnS materials for optoelectronic devices and photonic crystals.^{22,23}

Peng *et al.*²³ studied the effect of copper doping on ZnS prepared by a facile wet chemical method. It was found that as well as introducing a p-type dopant level into the band structure of ZnS, there was also an increase in the number of defects related to ion vacancies. These defects in a nanoparticle can affect the band structure by introducing new energy levels into the band gap and reducing the effective band gap energy. The presence of excess defects in a nanoparticle can reduce the levels of photocatalytic activity by acting as electron or hole traps and the level of doping and synthesis technique has an impact on the levels of dopants.

Kohtani *et al.* looked at the effect of lead, copper and nickel doping on ZnS. They found that Pb and Cu doped ZnS had a higher activity for the degradation of fluorinated organic compounds due to the Pb and Cu extending the photocatalytic response of ZnS toward the visible light region. It was also found that the metallic dopants act as redox reaction sites on the surface of the nanoparticle. In the same study it was noted that Ni doping does not have the same mechanism and so the photocatalytic activity is comparable to undoped ZnS.

Arai *et al.*²⁴ also found that Cu doped ZnS improved the photocatalytic activity of ZnS under visible light irradiation for hydrogen splitting in hydrogen sulfide due to the formation of a new energy level in the band structure of ZnS and that this donor level has partially filled 3d orbital of Cu²⁺.

Non metal doping of ZnS with nitrogen and carbon was reported by Muruganandham *et al.*²⁵ with excellent visible light absorption compared to the undoped material and the doped material was used to degrade the model pollutant AO7 (acid orange 7 dye) under visible light irradiation. The doping with nitrogen and carbon resulted in the formation of a new energy level in the band structure of the ZnS resulting in the effective band gap reducing to as low as 1.95 eV. Another non metal doping route was reported by Gou *et al.*²⁶ who used a conjugated polymer, polyvinyl chloride, to induce visible light photoactivity to ZnS. The conjugated polymer ZnS complex had a broader absorption spectra compared to ZnS alone but also the presence of the polymer lead to a more efficient separation of the electron hole pair which increased the photocatalytic activity.

1.4.2 Controlling the Size of the Photocatalyst

The size of the semiconductor photocatalyst plays a very important role in the activity of the catalyst. The lower the particle size, the higher surface-to-volume ratio the particle size has.⁶⁰ Ghosh *et al.*²⁷ controlled the size of the ZnS particle growth by using poly-*N*-vinyl-2-pyrrolidone (PVP) as a capping agent and by preventing agglomeration of the nanoparticles found an increase in the photoluminescence and decreased recombination of the photo-generated electron-hole pair.

1.4.3 Reducing Recombination

Recombination of the electron-hole pair is a limiting factor in the efficiency of a photocatalyst. Many recombination pathways, both radiative and non-radiative, exist and overcoming these pathways to reduce the recombination rate increases the photocatalytic activity of the photocatalyst.²⁷

One method of reducing the recombination rate is to prepare nanosized materials. Nanometer-sized semiconductor particles with an increased band gap compared to bulk materials, due to quantum confinement enhances the charge-transfer rates in the system and drastically reduces the volume recombination of the electron-hole pair within the semiconductor nanoparticle.⁶⁰

Doping of the semiconductor with metal ions is the most common method used to reduce the recombination rate of the electron hole pair. It was shown that cobalt doping²⁸ reduced the radiative recombination rate and photoluminescence as the cobalt acts as an electron trap with an energy band. Traps, both electron and hole, can have both negative and positive effects of the photocatalytic activity. The trap can reduce the recombination rate by trapping either an electron or hole, allowing the other to produce reactive oxygen species required to complete the photocatalysis but also with the electron or hole trapped, it itself is not available for photocatalytic activity. As with all elements involved in optimising the photocatalytic semiconductor, finding the right level of dopant to achieve the positive impact of reducing the recombination rate is required.

1.5 Zinc Sulfide

1.5.1 Physical Properties of Zinc Sulfide

Zinc sulfide, a type II-VI semiconductor was one of the first semiconductors discovered and has been extensively studied due to its vast array of applications.^{29,30,31,32,33,34} ZnS is the most common form of zinc found in nature as the black mineral sphalerite.³⁵ The black colour comes from impurities in the mineral, mainly iron, and pure sphalerite is white.

ZnS has two main structural polymorphs (figure 1.4), the cubic blende sphalerite and the hexagonal wurtzite structure and the physical properties of both are described in table 1.1. Cubic blende ZnS has a face centred cubic structure, characterised by ABCABC-type stacking in which both the zinc and sulfur atoms are tetrahedrally coordinated.^{36,37} Wurtzite phase ZnS has a hexagonal close packed structure in which the Zn and S atoms are also tetrahedrally coordinated.

Table 1.1 Physical properties of zinc sulfide⁹⁰

Property	Cubic Blende Sphalerite	Hexagonal Wurtzite
Molecular Weight (g/mol)	94.47	94.47
Melting Point (°C)	1,700	1,700
Light Absorption (nm)	335	326
Crystal Structure	Tetrahedral	Tetrahedral
Lattice Constants (nm)	a/b/c = 0.541	a/b = 0.382 c = 0.626
Density (g/cm ³)	4.090	4.090
Band Gap (eV)	3.7	3.8

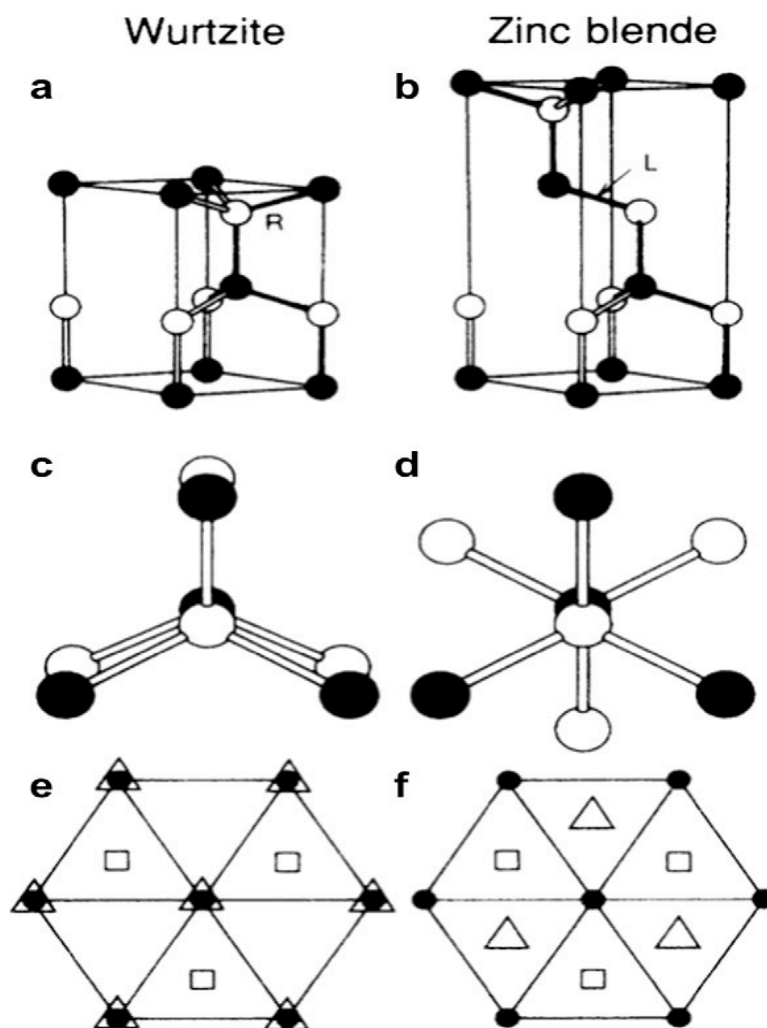


Fig 1.4 Models showing (a and b) the handedness of the fourth interatomic bond, (c and d) the respective eclipsed and staggered dihedral conformations and (e and f) the atomic arrangement along the close packing axis.^{29,38} (Image reproduced from reference 29)

Of the two forms, the cubic blende form usually crystallises at lower temperatures while the hexagonal wurtzite phase crystallises at temperatures above 1020 °C at standard pressures,³⁹ but at nanoparticle size this temperature can be reduced to as low as 400 °C.⁴⁰ At the bulk size the lattice formation enthalpy of cubic blende is approximately 10 kJ mol⁻¹ lower than that of the hexagonal wurtzite phase.³⁷

1.5.2 Band Structure of Zinc Sulfide

The two main polymorphs of zinc sulfide have similar band gaps of 3.7 eV for the cubic blende sphalerite phase and 3.8 eV for the hexagonal wurtzite phase which places it in the wide band gap class of semiconductors as shown in figure 1.5.^{41,42}

ZnS has a higher conduction band position compared to most other inorganic semiconductors,^{43,44} and the electrons that are promoted to the conduction band have the potential to reduce compounds, not accessible to other semiconductor photocatalysts, such as polyhalogenated benzenes, carbon dioxide, aromatic ketones and amides.

In nanosized ZnS particles, due to the quantum confinement effect, discussed later, the conduction band energy is reported to be at a more negative potential than the conduction band in the bulk material. Yin *et al.*⁴⁴ reported the conduction band energy at -2.3 V vs SCE for the nanosized ZnS whereas the bulk ZnS conduction band energy was -2.0 V vs SCE.

Density functional theory (DFT) calculations on ZnS²⁹ show that the valence band is comprised of three regions. The lower region consists of the s band from both zinc and sulfur, a higher region containing well localised Zn 3d states and the upper region of p-bands from sulfur hybridised with Zn 3d bands. The calculations also show that the p-electrons in the topmost valence band state bind tightly to sulfur so the positive holes are less mobile. The conduction band is shown to consist of Zn 4s bands with a contribution from S 3p orbitals.⁴⁵

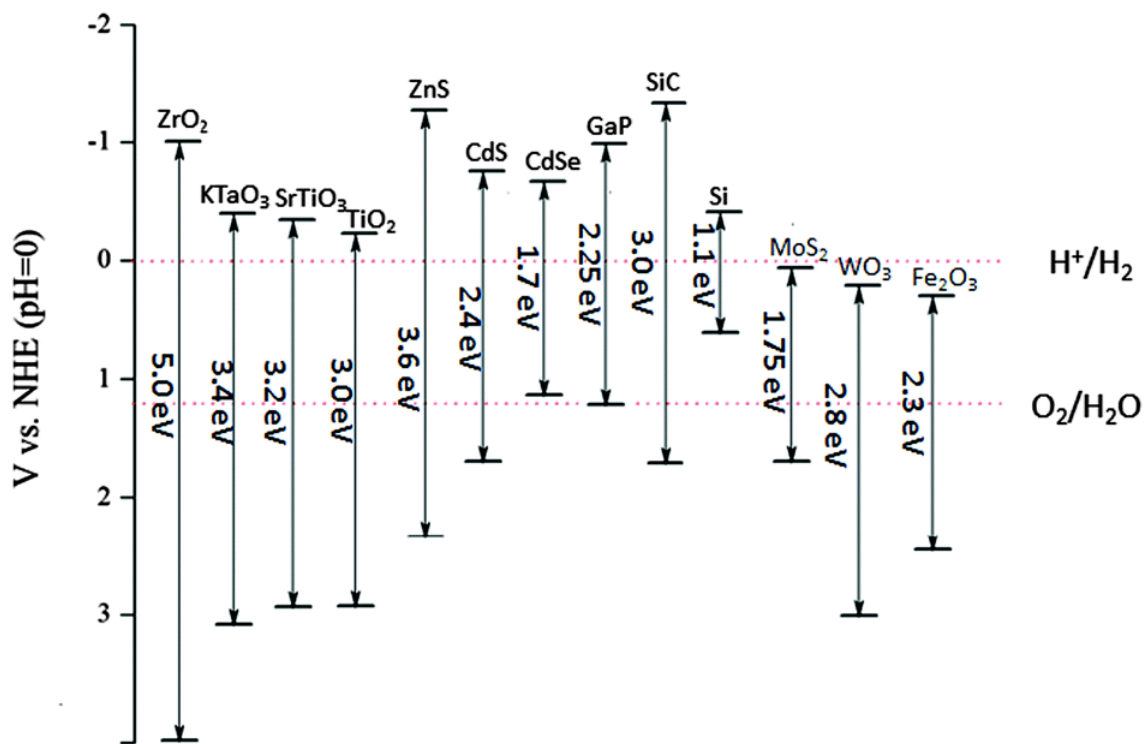


Fig 1.5 Band potentials of wide band gap semiconductors⁴⁶ (Imaged reproduced from reference 46, *Phys. Chem. Chem. Phys.*)

1.5.3 Applications of Zinc Sulfide

ZnS is one of the most important semiconductors in use in the electronics industry and is used in a pure and doped form in applications such as electroluminescence, nonlinear optical devices, light-emitting diodes (LEDs), flat panel displays, infrared windows, UV-light sensors, lasers, field-emitters, pigments and biological applications.^{41,47,48,49,50}

Zinc sulfide is a well known phosphor material with various luminescence properties, such as electroluminescence and photoluminescence and thus the material has been utilised in the fields of optoelectronics, such as solar cells and infrared windows and in lasers, displays and sensors.⁵¹ The nanoparticle form is more desirable for these devices than the bulk semiconductor as the photoluminescence intensity of the nanoparticles can be up to 25 times stronger than that of the bulk particles.⁵¹ Efficient emitting materials are required for the development of full-colour displays and Cu-doped ZnS has been investigated as an easily producible material which can be used as a luminescent light source in the blue-green region of the visible light spectrum⁵² and as a blue-emitting active laser.⁵³ For electronic and opto-electrical devices the wurtzite form of ZnS is more desirable than the cubic blende form.^{40,49,54} The surface state emission in the visible light region from defects in ZnS crystals is very important for these technologies. Surface emission intensity can be increased by controlling the size of the particle and by controlling the amount of defects by the synthesis technique.⁵⁵

Zinc sulfide has been studied in the field of photocatalytic water splitting for hydrogen production.⁴¹ Photocatalytic splitting of water involves the oxidation and reduction of H₂O to generate H₂ and O₂ with the hydrogen produced used in clean energy systems.⁵⁶ The advantages of using photocatalysis to generate hydrogen gas are the use of sunlight to produce the fuel and not traditional fossil fuels. Bang *et al.*⁵⁷ investigated the visible light photocatalytic water splitting from nickel doped zinc sulfide and showed that

hollow and solid spheres showed substantially improved efficiency compared to traditionally prepared ZnS nanoparticles due to their crystalline nature and high surface energy.

ZnS has been used a photocatalytic material for the decomposition of organic materials and toxic water pollutants. Nanosized ZnS has been studied for this application due to the rapid generation of the electron-hole pairs by photoexcitation and the highly negative reduction potentials of excited electrons.^{58,59,60,61}

Shao *et al.*⁵⁸ and Dong *et al.*⁵⁹ showed that hollow ZnS nanospheres could be used as a photocatalytic material to degrade the bromine containing test dye Eosin B in water and to degrade the organic dye methyl orange the presence of UV light. Yang *et al.*⁶² also used Eosin B to show the effectiveness of photocatalytic ZnS under UV light irradiation.

Kohtani *et al.*⁴³ demonstrated the ability of Pb-, Cu- and Ni- doped ZnS to degrade perfluorinated organic compounds. ZnS was chosen as the as the host material due to its wide band gap which is capable of accepting donor levels in the band structure and also due to the higher position of the conduction band levels which can be used in the photoredox reactions which degrade organic compounds.

Due to the large band gap of ZnS, for indoor light activity, ZnS generally requires modification of the band gap by doping or sensitisation of the semiconductor. Zhang *et al.*⁶³ showed that ZnS was photocatalytically active under visible light irradiation due to the presence of thiocyanuric acid. The thiocyanuric acid donates an electron when irradiated by the visible light to the conduction band of the semiconductor. The electron then reacts with oxygen on the surface of the particle to produce the superoxide anion, O_2^- , which degrades the model pollutant, methyl orange.

1.6 Synthesis Techniques

ZnS has been produced by many different techniques split into solution and gas based processes. The choice of synthesis technique effects the time and energy required to produce the material and also affects the properties, including the phase, particle size, crystallinity and photocatalytic activity. This research focuses on the preparation of ZnS nanoparticles through a microwave assisted technique but an overview of the other methods and there use in the literature is presented below.

1.6.1 Hydrothermal

A hydrothermal synthesis is carried out in a pressurised container, typically a Teflon lined autoclave in an aqueous solution.⁴¹ The autoclave is placed in an oven and heated over a period usually 8 – 12 hours, before the crystalline powder is collected, washed and dried and the material characterised and tested.^{64,65} Hydrothermal synthesis allows for the use of lower processing temperatures due to the closed vessel and increased pressure. However, the drawbacks of the hydrothermal method include small batch sizes, long processing times and the large energy input required to maintain an oven at processing temperatures for up to 12 hours. Hydrothermal has been combined with other techniques such as sol-gel⁶⁶, template assisted synthesis⁶⁷ and the preparation of single-source precursors to produce ZnS and other metal sulfide nanoparticles.

Jiang *et al.*⁶⁷ used acrylamide as a surfactant in combination with hydrothermal synthesis to produce ZnS microspheres and hallow nanospheres.

1.6.2 Solvothermal

Solvothermal synthesis is similar to hydrothermal except that an organic solvent is used as the solvent instead of water. Jang *et al.*⁴² used a solvothermal technique involving ethylenediamine to prepare ZnS nanoplates which were used to perform photocatalytic water splitting and photocatalytic degradation of azo dye acid red. Li *et al.*⁶⁸ also used ethylenediamine to produce ZnS by a solvothermal method and by varying the ratio of reactants were able to control the morphology and phase structure of the nanoparticles.

1.6.3 Sol-gel

Sol-gel methods are used to produce silica modified ZnS with the aim of producing crystalline ZnS with the properties of controlled particle size for the quantum confinement effect and passivation of the surface. Li *et al.*⁶⁹ used an acidified aqueous solution of tetraethylorthosilicate (TEOS) to prepare a sol-gel matrix. To this sol-gel a complex of EDTA-Zn and a sulfur source were added. Following hydrothermal treatment of the sol, crystalline ZnS nanoparticles were formed.

Senthilkumar *et al.*⁷⁰ used a simplified sol gel process via ultra sonication to produce ZnS nanorods. These materials calcined at 800 °C at different time intervals produced wurtzite phase ZnS. A sol gel was prepared using mercaptoethanol as a capping agent and by stirring the reaction mixture for 8 hours an homogenous stabilised dispersion was obtained. After treatment with ultrasonic irradiation and calcination, crystalline ZnS with nanorod morphology was produced.

1.6.4 Chemical Precipitation

Chemical precipitation is used for the preparation of colloidal systems and works for zinc sulfide due to the formation of strong ZnS bonds.⁷¹ Denzier *et al.*⁷¹ used solutions ZnSO₄ and Na₂S with rapid stirring and no heat to produce colloidal solutions of ZnS with an average particle size of 1 – 5 nm.

1.6.5 Template-Assisted Synthesis

Template-assisted synthesis methods are often used to control the morphology of the ZnS particles and to create one dimensional (1D) structures for specific applications.⁴⁷ Common template agents used are surfactants. Surfactants derive their name from their main property which is surface active agents. Surfactants are used to lower the interfacial tension between two liquids or between a solid and a liquid. Dinsmore *et al.*⁷² used sodium dioctyl sulfosuccinate to prepare manganese doped zinc sulfide with differing crystal phases depending on the temperature the particles were treated at. Naskar *et al.*⁷³ used various surfactants from the Span series to stabilise emulsions and control the particle size distribution of ZnS nanoparticles using a soft chemical method. The steric effect of PVP was employed by Panda *et al.*⁷⁴ to prepare mono-dispersed ZnS nanospheres with a particle size of 3-4 nm.

1.7 Microwave Synthesis

1.7.1 The electromagnetic spectrum

The electromagnetic spectrum (figure 1.6) is the complete range of all possibilities of frequencies of electromagnetic radiation. The spectrum is broken up into its component parts depending on the wavelength, frequency and energy of the radiation and the parts include the infrared region, the visible region, X-ray region and the microwave region.

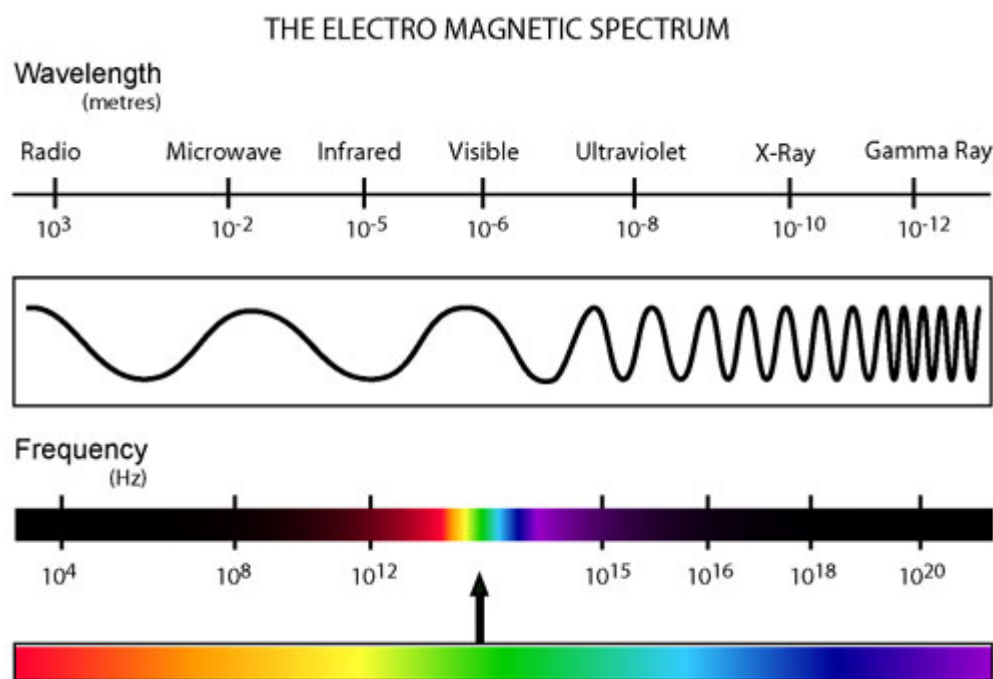


Fig 1.6 The electromagnetic spectrum showing its component parts separated by wavelength and frequency.⁷⁵ (Image reproduced from reference 75, University of Colorado website)

The most recognisable region is the visible region which occupies the space with a wavelength of 400 nm to 800 nm as this is the type of radiation that is seen by the human eye as light. At shorter wavelengths and higher energy than the visible light region is ultraviolet light, X-rays and gamma rays. Ultra violet light makes up a small percentage,

less than 5%, of the solar spectrum and the highest energy UV light is blocked from reaching the earth by the protective ozone layer which encompasses the planet.⁷⁶

X-rays are high energy, short wavelength radiation with a wavelength between 0.01 and 10 nanometers. The energy of X-rays is in the range of 100 eV to 100 keV and depending on the energy of the X-ray, has different applications. X-rays are produced in numerous ways including when fast moving electrons decelerate, when electrons transition between atomic orbitals and through synchrotron emission. Most naturally occurring X-rays are produced in outer space, for example the solar wind hitting the magnetosphere around the earth or expelled from black holes as the matter being pulled inside at great speeds collides and releases photons in the X-ray region of the EM spectrum. The most common man-made way of generating electrons is by utilising the X-rays generated by the transition of an electron from an outer orbital to an inner orbital in an atom. Because these transitions produce photons of a particular energy and wavelength each atom gives a characteristic X-ray. The X-rays are generated by bombarding a metal target with a high velocity beam of electrons inside a vacuum. The electrons have sufficient energy to knock out an electron from the inner shell leaving a vacancy for an electron from an outer shell to drop into and an X-ray is emitted with the loss of energy. Numerous metallic elements are used as targets depending on the application and the energy of the X-ray required. For medical applications tungsten is the most common element, with molybdenum used when a more sensitive part of the body is required. For X-ray crystallography, copper is the most common element used as the target.

Gamma ray – high frequency and high energy – produced from the decay of high energy states of atomic nuclei by reactions in stars and by the detonation of atomic weapons. They typically have energy greater than 100 keV. Gamma rays are distinct

form X-rays in that they are emitted from the nucleus of an atom but an X-ray is emitted from the electrons outside the nucleus. Gamma rays despite being very harmful to humans have been found to have a number of uses. When the body is exposed to gamma rays without adequate protection, the rays can interact with and break down the DNA molecules in the cells. Protection is usually provided by thick shielding made of heavy metals with lead being the most common shielding material used. Gamma rays are used in a variety of industrial sensors to measure thickness, density and depth and are also being used instead of X-ray machines for large cargo containers. Gamma rays are used in hospital environments to image tumours and to kill cancer cells.

Infrared light is located at wavelengths longer than those of visible light between 700 nm and 1 mm. Infrared light is emitted or absorbed by molecules when they change their rotational-vibrational movements. Over half of the energy that arrives on earth from sunlight is in the infrared spectrum, as is most of the thermal radiation emitted by objects at room temperature. Infrared radiation is used for wide ranging applications such as communications, spectroscopy, medical applications, thermal imaging and for curing coatings. The greenhouse effect which is a major cause of climate change is caused by absorption of infrared radiation emitted by or reflected by the earth's surface by compounds such as CO₂, CH₄, NO_x, H₂O and CFCs.

Radio waves are at the extreme end of the electromagnetic spectrum with the longest wavelengths from 30 cm to hundreds of kilometres in length. Radio waves are used in communication to send broadcast signals from television and radio, and even to communicate with the Mars rovers and probes that are travelling throughout the solar system.⁷⁷

1.7.2 Microwaves

Microwaves lie between radio waves and infrared radiation in terms of wavelength and frequency. A broad definition of microwaves is anything between 300 MHz (0.3 GHz) and 300 GHz, with a wavelength between 0.1 cm and 1 m and this includes ultra-high frequency (UHF) and extremely-high frequency (EHF) waves. Microwaves are used for point to point communication, for transmission of television signals via satellites and in radar systems. The most common way of generating microwaves is by using a magnetron but there are other generators including klystrons, gyrotrons and travelling wave tubes. Magnetrons as we know them today were invented by John Randell and Harry Boot at the University of Birmingham during World War II as a way of generating microwaves to be used in radar devices.

Randell and Boots improved Magnetrons consist of a heated cathode, an anode which is kept at a higher potential than the cathode, two large magnets and an antenna, see figure 1.7. The electrons are emitted from the heated central cathode and accelerated towards the anode but the presence of the magnetic field causes the electrons to travel along a curved path in the drift space between the cathode and anode. Due to the deviation from their paths an r.f. field is induced in the cavities which propagate back into the drift space. The electrons from the cathode then interact with the r.f. field and the energy given off is defined by the potential difference between the cathode and anode. The antenna/waveguide is then used to transmit the microwaves generated by these interactions into the intended target area. The shape and materials used in the waveguides can be used to filter the different wavelengths and this is useful for point to point communication systems.

The heating property of microwaves was first investigated in 1946 by Dr. Percy Spencer who was working on radar technology at Raytheon when he noticed a chocolate bar is

his pocket had melted while he was standing next to an active radar set. Spencer went on to create the microwave oven by experimenting with food exposed to a magnetron including eggs and popcorn. Eventually they enclosed the magnetron inside a metal box to protect those nearby from exposure to the microwave irradiation.

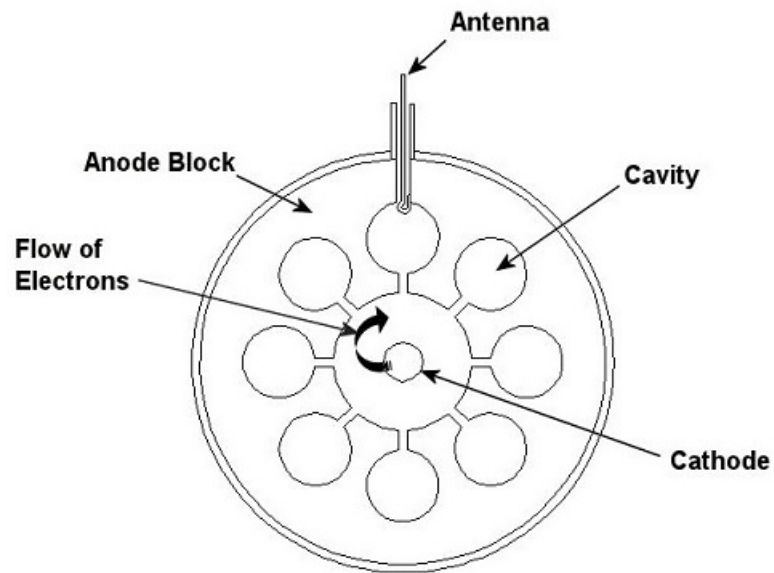


Fig 1.7 Schematic view of the interior of a magnetron (magnets would be above and below the magnetron in the above diagram)

1.7.3 Microwaves and Chemical Synthesis

Microwave irradiation was first used in chemical synthesis in the 1980's following two publications by Gedye in 1986⁷⁸ and by Giguere *et al.*⁷⁹ in 1988. Microwave heating for chemical reactions was initially used in organic reactions but since then has been used for inorganic reaction, preparation of thin films, curing of polymers and for heating solid-state reactions. Compared to conventional heating such as using an oil bath or furnace, microwave heating has been shown to be advantageous in that it produces better yields, has a reduced reaction time and uses lower amounts of energy. This is achieved due to direct microwave interaction with the material in the microwave cavity and does not rely on conduction of the heat through from the source through to the target material. Gedye *et al.*⁸⁰ performed numerous organic reactions in 1988 which took 2-3 hours to complete under typical reflux conditions but were completed in 2-3 minutes using a Teflon coated sealed reactor in the microwave.

Another important component is the materials susceptibility to microwave irradiation. Materials are divided into conductors and insulators/dielectrics but this division is dependent on the frequency of the electromagnetic irradiation applied to the material and the conductivity, permittivity and permeability of the material. The absorption of the electromagnetic energy can be described as

$$\epsilon = \epsilon' + j \epsilon'' \quad \text{Equation 1.16}$$

where ϵ' is the real component of permittivity and ϵ'' is the imaginary component of permittivity. The real part represents the degree to which the electric field may build up inside the material when exposed to the electric field while the imaginary part or dielectric loss is a measure of the amount of the field transformed into heat.

The loss angle, δ , the phase difference between the electric field and the polarisation of the material is related to the complex dielectric constant as

$$\tan \delta = \epsilon'' / \epsilon' \quad \text{Equation 1.17}$$

Therefore the $\tan \delta$, the dissipation factor determines the ability of the material to transform the absorbed electromagnetic energy into heat. For the microwave interactions, the materials can be further classified into three categories; i) Microwave reflectors such as metals, ii) microwave transmitters such as fused quartz and ceramics and iii) microwave absorbers such as water. The microwave reflectors such as metals are used to build the cavities of microwave ovens which allow for the microwave irradiation to be contained in the oven and not leak into the open. Lead lined glass allows for a user to observe the reaction inside the microwave while not exposing the user to the radiation. The microwave transmitters can be used to create windows between the magnetron and the microwave cavity and also as reaction vessels such as Teflon coated vessels and glass beakers. The microwave absorbers take up microwave energy and are rapidly heated once exposed to microwave irradiation.

Microwave absorbers are known as dielectric materials and energy absorption is primarily due to the presence of the permanent dipole moment of the molecules which orient and reorient themselves under the influence of the electric field of the microwave. The reorientation loss mechanism originates from the inability of the polarisation to follow the rapid reversals of the electric field.

At lower frequencies (below 100 MHz), the dipoles follow the changes in the field and their orientation changes in phase with the field. At very high frequencies (1 – 10 THz), the molecules no longer respond to the electric field. Between the lower and higher frequencies at the medium microwave range (300 MHz – 300 GHz) the molecules inertia from following the changes in the field and the interaction with neighbouring

molecules make changing the orientation more difficult and so the dipoles lag behind the field changes. This phase lag of the dipoles absorbs power from the electric field and the dielectric loss of the energy occurs as the dipole relaxes. This is known as dielectric heating.

Microwave penetration depth (D_{ph}) is also a parameter to consider when selecting materials for use in microwave chemistry. The penetration depth is defined as the depth into the material at which the power is reduced to one third of its original intensity. The absorption of the dielectric material, α , is related to the imaginary parts of the dielectric constant, ϵ'' , or the refractive index. The depth penetration is related to the absorption coefficient by;

$$D_{ph} = 1/\alpha \qquad \text{Equation 1.18}$$

Therefore materials with a high absorption coefficient have a shallower depth penetration. Penetration depth is dependent on a number of factors including temperature of the water, type and concentration of any salts present and the incident wavelength of the microwaves. Water has a depth penetration between 1 cm and 2 cm at room temperature and a microwave frequency of 2450 MHz, which was used in all experiments in these studies.

Polar molecules have permanent dipole moments (separation of positive and negative charges) due to the difference in the electro-negativity between the atoms in the molecules. The presence of the permanent dipoles makes polar molecules ideal solvents for use in microwave reactions. Table 1.2 shows the dipole moments of various polar and non-polar solvents.

Table 1.2 Polar and non-polar solvents with their boiling points and dielectric constants

Solvent	Polar / Non-Polar	Boiling Point	Dielectric Constant
Hexane	Non-Polar	69 °C	1.88
Toluene	Non-Polar	111 °C	2.38
Dichloromethane	Non-Polar	40 °C	9.1
Dimethylformamide	Polar	153 °C	38
Iso-propanol	Polar	82 °C	18
Ethanol	Polar	79 °C	24
Methanol	Polar	65 °C	33
Water	Polar	100 °C	80

Water has the highest dielectric constant of the solvents available for use in microwave chemistry and so is an excellent solvent for this use. When water is placed in a microwave cavity and exposed to microwave irradiation the molecules rapidly absorb the energy. The electric dipoles of the water molecules respond to the applied electric field of the microwave and as the molecules interact with the neighbouring molecules the dipole orientation is unable to respond to the field and so resistive heating occurs as shown in figure 1.8.

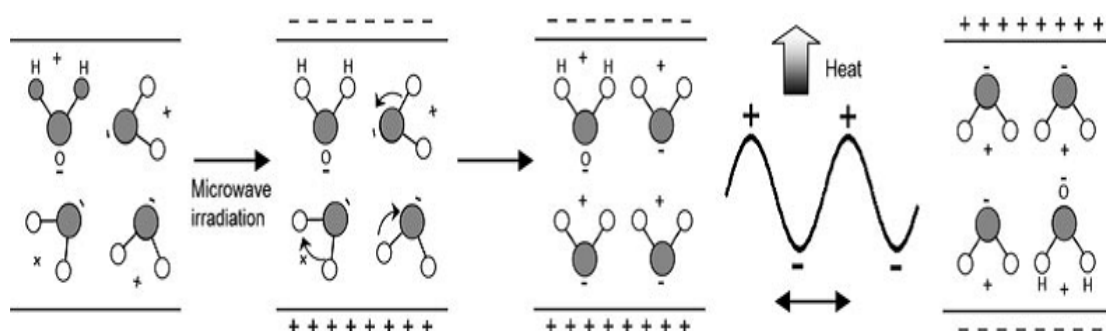


Fig 1.8 Mechanism of heating of water by microwave irradiation.⁸¹ (Image reproduced from reference 81, *Chemistry A European Journal*)

The dipole species possess a characteristic relaxation time and frequency dependent dielectric constant. Owing to this, at 2.45 GHz, water has a rapid dissipation of the electromagnetic energy as heating, therefore water heats up rapidly under microwave irradiation.

Microwave synthesis exhibits many advantages including being effective, economical and environmentally friendly. Some additional advantages of microwave heating are rapid volumetric heating, fast reaction rate, short reaction time, high reaction sensitivity and energy saving. Microwave synthesis also produces particles of small size and a narrow particle size distribution.⁸² Microwave heating also provides opportunities for scale up of reactions without unwanted thermal gradient effects thus providing potential large scale industrial applications.⁸³

Microwave synthesis is widely used to prepare zeolites, inorganic materials, ceramic materials, and in organic, peptide, polymer synthesis and biochemical processes.

Zhai *et al.*⁸⁴ used a combination of microwave and chemical bath deposition to prepare ZnS and CdS thin films which was put forward as a technique to produce these thin films using a time saving method. Liao *et al.*⁸⁵ produced a nanocrystalline metal sulphides (Cu, Hg, Zn, Bi, Pb) using microwave-assisted reflux synthesis in formaldehyde solutions of the metal salt and thioacetamide. Zhu *et al.*⁸⁶ also used a microwave-assisted reflux reaction setup to produce nanosized ZnS and CdS particles. Zhao *et al.*⁵⁰ used microwave-assisted synthesis to produce ZnS nanoballs in saturated aqueous solutions. A combination of single-source precursors and microwave degradation to prepare wurtzite ZnS was reported by Sun *et al.*⁸⁷

1.8 Nanosized Versus Bulk Materials

Nanocrystalline semiconductor photocatalysts have been studied extensively in recent years because of their special properties such as large-surface to volume ratio, increased catalytic activity and special electrochemical properties when compared to those of their bulk counterparts.⁸⁸ Nanoparticles also have larger band gap energies compared to the bulk materials due to quantum size confinement.⁸²

In semiconductors the energy gap between the top of the valence band (HOMO) and the bottom of the conduction band (LUMO) is called the band gap. In a photoactive semiconductor, when light of a wavelength with greater energy than the bandgap hits the valence band, electrons are excited to the conduction band leaving a hole in the valence band. The distance between the electron in the conduction band and the hole in the valence band is called the exciton Bohr radius, α_B^{exc}

$$\alpha_B^{exc} = \frac{h^2}{8R^2} \left(\frac{1}{m_e^*} + \frac{1}{m_h^*} \right) \quad \text{Equation 1.19}$$

Where m_e^* and m_h^* are the effective masses of the electron and hole, h is Planks Constant, R is the radius of the nanoparticle.⁸⁹ In a bulk semiconductor the energy gap is constant but in a nanosized material with a size comparable to the Bohr radius the band gap is size dependent. This is due to the motion of electrons and holes being restricted due to the finite size of the nanoparticle. The relationship between the band gap of a nanosized material and a bulk material is given in equation 1.19.⁸⁹

$$E_{g(nano)} = E_{g(bulk)} + \frac{h^2}{8R^2} \left(\frac{1}{m_e^*} + \frac{1}{m_h^*} \right) \quad \text{Equation 1.20}$$

Equation 1.19 shows that due to the quantum confinement effect there is an inverse-square dependence of the band-gap on the radius of the nanoparticle and results in spatial confinement of the charge carrier wave functions and leads to a blue-shift of the

absorption edge of the semiconductor. For most semiconductors the exciton Bohr radius is below 10 nm. In bulk semiconductors the large number of molecular orbitals creates a band of continuous electronic states. In a nanosized semiconductor the number of bands decreases, splitting the conduction and valence band into discrete energy levels. The HOMO – LUMO gap widens, increasing the effective bandgap and also the redox potential of the bands.⁹⁰

For nanoparticles, a large percentage of atoms are on or near the surface, leading to a vast interface between the nanoparticle and the surrounding medium. In the case of catalysts the surface plays a vital role as in the initiation and termination of reactions. The larger surface area of a nanoscale semiconductor also changes the physical properties of the material compared to the bulk with the melting point and phase transition temperature often much lower in nanosized materials. This is because surface atoms are much easier to remove than bulk atoms and so the energy required to physically change the material is lower. In imperfect crystals the surfaces can be covered with defects and dangling bonds which can act as electron and hole traps.²¹ The presence of these defects can modify the bandgap of the semiconductor by having energies which lie within the bandgap.³⁶ These defects also affect the photochemical reactions on the surface by trapping electrons or holes or electron-hole pairs and increasing the lifetime of these species and therefore increasing the photocatalytic activity of the semiconductor.

1.9 Project Hypothesis

This project was started with the aim of investigating zinc sulfide as a potential semiconductor photocatalytic material to be used as an anti-bacterial agent against bacteria which cause healthcare associated infections. As part of this, there was an aim to develop a low cost, quick and environmentally benign synthesis method that had the potential to be scaled up to an industrial scale.

Specific aims of the project

1. The development of a microwave-assisted synthesis method to produce zinc sulfide and quantify its photocatalytic activity and anti-bacterial properties in an indoor-light environment.
2. To investigate the group 13 metals (aluminium, gallium and indium) as dopants to improve the photocatalytic performance of microwave-assisted ZnS and to examine the optical and physical properties of group 13 metal doped ZnS.
3. To investigate co-doping of ZnS using silver and indium and the effects that co-doping has on the optical and physical properties of ZnS and the photocatalytic activity.

Chapter 2: Experimental Procedures and Characterisation Techniques

2.1 Materials

Zinc acetate dihydrate (98%), thiourea (ACS reagent), indium acetate (99.99%) gallium oxide (99.99%), aluminium oxide (99.99%) and silver nitrate (ACS reagent) were all purchased from Sigma Aldrich and used as received. Methylene blue was obtained from Gurr's Company. Mueller Hinton broth and Mueller Hinton agar were acquired from Cruinn Diagnostics Ltd and used as received. Deionised water was used in all stages of synthesis, characterisation and photocatalysis.

2.2 Equipment

The photocatalyst powders were characterised by X-ray diffraction using a Siemens D 500 X-ray diffractometer with the diffraction angles scanning from $2\theta = 20 - 80^\circ$, using a Cu K α radiation source. The diffuse absorbance spectra of the samples were measured by a UV-Vis-NIR Perkin Elmer Lambda 900 spectrometer between 800 and 200 nm with a blank KBr disc used as a reference. Surface area analysis was carried out by B.E.T. analysis using a Quantachrome Nova 2200e surface area and pore size analyzer after the samples had been purged for three hours after N₂ at 300 °C. Fluorescence measurements were taken, with samples suspended in ethanol, by a Perkin Elmer LS 55 luminescence spectrometer. Transmission electron microscopy (TEM) images were captured with a Joel JEM 100CX II electron microscope. Scanning electron microscopy images were taken using a Hitachi SU 70 FE-SEM with a Schottky electron gun. X-ray photoelectron spectroscopy was carried out a Thermo VG Scientific Sigma Probe Spectrometer. Raman spectroscopic measurements of the powdered samples were taken using a Horiba Jobin Yvon LabRAM HR800 raman spectrometer. Photocatalysis experiments were carried out using a Solas 60 W incandescent bulb. All microwave assisted synthesis reactions were carried out in a MARS 5 microwave system.

2.3 Synthesis of the Semiconductor

2.3.1 Preparation of Zinc Sulfide

Zinc sulfide was synthesised in an open vessel assisted by microwave irradiation. In a typical reaction, zinc acetate dihydrate (4.3888 g in 200 mL of H₂O, 0.2 M) was added to a beaker containing thiourea (1.5218 g in 200 mL H₂O, 0.2 M). This beaker was placed in the microwave and irradiated at 600 W for 30 minutes, which resulted in a dry, yellow powder, which was collected from the beaker after a 5 minute cool down period. The microwave power was varied from 150 – 720 W through 300, 450 and 600 W respectively. With the variation in irradiation power the irradiation time was also changed, for example, samples irradiated at 150 W were irradiated for 120 minutes while those prepared at 720 W were irradiated for 15 minutes. In all reactions the volume and concentrations of the zinc precursor and the sulfur precursor were kept equal. Separate experiments to examine the effect of precursor concentration and volume were carried out by varying the concentration of the precursor from 0.1 to 0.2 M and the volume changed from 100 to 200 mL. Sample details are outlined in table 2.1.

The samples are named such that the chemical structure is first (ZnS) followed by the microwave irradiation power in watts (600), followed by the irradiation time in minutes (30) and the concentration of the precursor solutions in moles/L (02) where 01 is 0.1 moles/L and 02 is 0.2 moles/L.

Table 2.1 Sample preparation of ZnS

Sample Name	Precursor Conc. (M)	Irradiation Power (W)	Irradiation Time (min)
ZnS150-60-01	0.1	150	60
ZnS150-60-02	0.2	150	60
ZnS150-120-01	0.1	150	120
ZnS150-120-02	0.2	150	120
ZnS300-30-01	0.1	300	30
ZnS300-30-02	0.2	300	30
ZnS300-60-01	0.1	300	60
ZnS300-60-02	0.2	300	60
ZnS450-20-01	0.1	450	20
ZnS450-20-02	0.2	450	20
ZnS450-40-01	0.1	450	40
ZnS450-40-02	0.2	450	40
ZnS600-15-01	0.1	600	15
ZnS600-15-02	0.2	600	15
ZnS600-30-01	0.1	600	30
ZnS600-30-02	0.2	600	30
ZnS720-15-01	0.1	720	15
ZnS720-15-02	0.2	720	15
ZnS720-30-01	0.1	720	30
ZnS720-30-02	0.2	720	30

2.3.2 Preparation of Aluminium Doped Zinc Sulfide

The synthesis of aluminium doped zinc sulfide samples were all carried out at 600 W microwave irradiation power. Zinc acetate dihydrate (200 mL, 0.2 M) and thiourea (200 mL, 0.2 M) were used as the zinc and sulfur precursors respectively. Aluminium oxide (0.04 M) was used as the aluminium precursor. The samples were prepared by adding various amounts of aluminium oxide corresponding to different mol % of aluminium (0.2, 0.4, 0.8, 1, 2, 5 and 10 mol %) and added to the beaker containing zinc acetate and thiourea prior to irradiation. For the samples prepared contain 0 to 2% aluminium the irradiation time was 30 minutes but it was increased to 35 minutes for the 5% Al – ZnS and 40 minutes for the 10% Al – ZnS due to the increase in the volume of water which was to be evaporated during the reaction.

2.3.3 Preparation of Gallium Doped Zinc Sulfide

The synthesis of gallium doped zinc sulfide samples were all carried out at 600 W microwave irradiation power. Zinc acetate dihydrate (200 mL, 0.2 M) and thiourea (200 mL, 0.2 M) were used as the zinc and sulfur precursors respectively. Gallium oxide (0.04 M) was used as the gallium precursor. The samples were prepared by adding various amounts of gallium oxide corresponding to different mol % of gallium (0.2, 0.4, 0.8, 1, 2, 5 and 10 mol %) and added to the beaker containing zinc acetate and thiourea prior to irradiation. For the samples prepared contain 0 to 2% gallium the irradiation time was 30 minutes but it was increased to 35 minutes for the 5% Ga – ZnS and 40 minutes for the 10% Ga – ZnS due to the increase in the volume of water which was to be evaporated during the reaction.

2.3.4 Preparation of Indium Doped Zinc Sulfide

The synthesis of indium doped zinc sulfide samples were all carried out at 600 W microwave irradiation power. Zinc acetate (200 mL, 0.2 M) and thiourea (200 mL, 0.2 M) were used as the zinc and sulfur precursors respectively. Indium acetate (0.04 M) was used as the indium precursor. The samples were prepared by adding various amounts of indium acetate corresponding to different mol % of indium (0.2, 0.4, 0.8, 1, 2, 5 and 10 mol %) and added to the beaker containing zinc acetate and thiourea prior to irradiation. For the samples prepared contain 0 to 2% indium the irradiation time was 30 minutes but it was increased to 35 minutes for the 5% In – ZnS and 40 minutes for the 10% In – ZnS due to the increase in the volume of water which was to be evaporated during the reaction.

2.3.5 Preparation of Silver and Indium Co-Doped Zinc Sulfide

The synthesis of silver and indium co-doped zinc sulfide samples were all carried out at 600 W and 30 minutes irradiation power and time. Zinc acetate (200 mL, 0.2 M), thiourea (200 mL, 0.2 M) and indium acetate (4 mL, 0.04M) were used as the zinc, sulfur and indium precursors respectively. Using this volume and concentration of indium acetate keep the mol % of indium constant at 0.4% for all the silver and indium co-doped samples. Silver nitrate (0.04 M) was used as the silver precursor as was added in various amounts corresponding to different mol % of silver (0.4, 1, 2, 4 and 8 mol %) and was added to the beaker containing zinc acetate, thiourea and indium acetate prior to microwave irradiation.

2.4 Characterisation Techniques

2.4.1 Powder X-ray Diffraction Analysis

X-ray diffraction is used in the qualitative identification of crystalline materials based on the Bragg equation⁹¹, (equation 2.1)

$$2d \sin \theta = n\lambda \quad \text{Equation 2.1}$$

Where, d is the *d-spacing*, the perpendicular distance between pairs of adjacent planes within the crystal, θ is the *Bragg angle*, or the angle of incidence of the X-ray, n is the diffraction order and λ is the wavelength of the X-ray. The wavelength of X-ray used is the $K\alpha$ radiation from a Cu source, which emits X-rays at a wavelength of 1.5418 Å.

An X-ray is emitted from the copper source when it is struck by high-energy charged particles, such as electrons accelerated through 30 kV.⁹¹ The incident charged particles have sufficient energy to eject some of the Cu 1s (k shell) electrons. The vacancy left by the 1s electron is filled by an electron from an outer orbital, either the 2p or the 3p shells, and the energy released is emitted in the form of an X-ray. The X-ray released has a fixed wavelength. When the transition from 2p \rightarrow 1s occurs, it is called a $K\alpha$ transition and has a wavelength of 1.5418 Å. When a 3p \rightarrow 1s transition occurs, it is called a $K\beta$ transition and has a wavelength of 1.3922 Å. $K\alpha$ is used as this transition occurs more frequently than $K\beta$.

The intensity of the diffracted X-rays from the powder is plotted against the 2θ values to give a pattern. Each crystalline phase has a characteristic pattern, which can be used as a fingerprint for identification purposes. There are two main factors, which determine the X-ray diffraction pattern, the first is the size and shape of the unit cell and second,

the atomic weight and position of the atoms in the cell. Therefore, even though two materials may have the same crystal structure they will have distinct diffraction patterns.

The crystallite size of the crystalline nanoparticles can be estimated from the X-ray powder diffraction using the Scherrer equation⁹² as shown in equation 2.2,

$$\tau = \frac{k\lambda}{\beta \cos \theta} \quad \text{Equation 2.2}$$

The Scherrer equation estimates the size of the crystallites, τ , using k , which is a correction factor of 0.9 and λ , the wavelength of X-ray. In these experiments a Cu $K\alpha$ source is used to generate X-rays where $\lambda = 1.5418 \text{ \AA}$. β represents the line broadening at half the maximum intensity which is measured from the X-ray diffraction pattern and θ is the Bragg angle of the diffraction peak measured in radians.

The powder X-ray diffraction patterns were collected using a Siemens D 500 X-ray diffractometer with diffraction angles scanning between $2\theta = 20 - 80^\circ$, using a Cu $K\alpha$ radiation source.

All X-ray diffraction graphs were analysed against the library from International Centre for Diffraction Data which was linked to the software on the computer were the data from the diffractometer was analysed.

2.4.2 X-ray Photoelectron Spectroscopy

X-ray photoelectron spectroscopy (XPS) is a technique which is a part of a suite of electron spectroscopy techniques which measure the kinetic energy of electrons that are emitted from matter as a consequence of bombarding the matter with ionizing radiation or high-energy particles.⁹³ XPS is a useful for studying surfaces of matter because the electrons that are produced are not very energetic and are rapidly absorbed by the solid

matter. Therefore they cannot escape from the solid unless they are ejected within 20 – 50 Å of the surface.

The XPS pattern is determined by plotting the intensity of the electron counts versus the energy (eV) at which the electron is ejected. This energy is quoted as the binding energy of the electron and is used to determine the chemical species of the element.

X-ray photoelectron spectroscopy analyses were performed using a Thermo VG Scientific (East Grinstead, UK) Sigma Probe spectrometer. Dr. S. J. Hinder from the University of Surrey performed the XPS measurements of all samples. The instrument employs a monochromated Al K α X-ray source ($h\nu = 1486.6$ eV) which was used at 140 W. The area of analysis was approximately 500 μm in diameter.

2.4.3 UV-Visible Absorption Spectrometry (UV-vis)

UV-visible light absorption spectroscopy is based on measuring the electronic transitions that occur within and between molecules when they are irradiated with UV and visible light sources. The detector measures the light that is not absorbed by the molecules and so the absorption can be inferred from what is not seen by the detector. The characteristic absorption wavelengths can be used to identify molecules, the wavelength at which absorption occurs can determine the band gap of semiconductors and the intensity of the absorption can be used to determine the concentration of the molecules based on the Beer-Lambert law, equation 2.3,

$$A = \epsilon cl \quad \text{Equation 2.3}$$

Where A is the absorbance intensity, ϵ is the molar coefficient of the molecule, c is the concentration and l is the path length.

The optical properties and diffuse absorbance of the samples were measured using a UV-Vis-NIR Perkin-Elmer Lambda 900 spectrophotometer. For the absorption

measurement of the model dye, methylene blue, the aliquots were taken in a poly(methyl methacrylate) (PMMA) cuvette and scanned between the wavelengths of 400 and 800 nm. For the diffuse absorbance spectra, a quantity of the sample was mixed with spectroscopic grade potassium bromide (KBr) (1:10 ratio) and ground well. The mixture was pressed into a disc and this disc was scanned between 800 and 200 nm using a blank KBr disc as a reference material.

The band gap of semiconductors was estimated from the diffuse absorbance plots using Tauc plots.⁹⁴ This involves plotting $(\alpha h\nu)^{1/r}$ versus $h\nu$, where α is the absorption coefficient of the material and r is $\frac{1}{2}$ for direct allowed transitions such as transition of an electron from the valence band to the conduction. An extrapolation from the linear part of the plot to the energy axis ($h\nu$) provides an approximation of the band gap in electron volts (eV).

There are limitations to using this method to estimate the band gap. Scattering of the incident light by particles of differing sizes can lead to difficulty in resolving the absorption spectra. The samples prepared in this work were not extremely crystalline (compared to those calcined at 200 °C for example in chapter 4) and so amorphous material present may have contributed to scattering. Additional absorption resulting from the different types of intrinsic defects also adds to the margin of error when attempting to estimate the band gap of the materials.

The energy difference between the conduction band and the valence band, the band gap, is measured using equation 2.4. where E is the band gap, h is planks constant, c is the speed of light and λ is the wavelength measured.

$$E_{\gamma} = h\nu = \frac{hc}{\lambda}$$

Equation 2.4

The UV-Vis spectrum of each sample was measured between 800 and 200 nm and the wavelength at which the absorbance increases due to absorption of light by the semiconductor is divided to give the band gap, $\Delta E_{c \rightarrow v}$, in electron volts (eV).

2.4.4 Transmission Electron Microscopy

Transmission electron microscopy (TEM) investigates the morphology and crystalline size of nanoparticles by a beam of electrons generated from a tungsten filament. Using electrons as opposed to visible light in tradition microscopy allows the imaging of nanosized materials. The electrons are accelerated through a vacuum and focused on the sample using a set of electromagnetic lenses. An image is produced by the contrast of the dark areas showing where the sample absorbs the electrons and the light areas where no sample is present.

Transmission electron microscopy images were captured using a Jeol JEM 100CX II electron microscope. The samples for the TEM were prepared by dispersing the powder in ethanol with sonication. The dispersed powder was then dropped on to copper coated TEM grids and allowed to dry overnight. The samples were imaged using an accelerating voltage of 100 keV at various magnifications.

2.4.5 Field Emission Scanning Electron Microscopy

Field-emission scanning electron microscopy is a powerful tool for imaging of nanoparticles. The electrons generated are focused into a beam by a series of lenses and the beam is scanned across the sample. The beam loses energy when it interacts with the sample and generates both X-rays and secondary electrons. The X-rays are used for chemicals analysis and the secondary electrons are used to build up an image of the sample surface.

FESEM images were taken using a Hitachi SU 70 FESEM with a Schottky electron gun. Measurements were carried out at an accelerating voltage of 5 – 15 kV. Powdered

samples were evenly distributed on a mounted carbon tape surface. Loose powdered sample was removed by blowing with a canned air spray.

2.4.6 Luminescence Spectroscopy

Emission luminescence spectroscopy works by exciting the sample material (usually with a UV light source) which causes an electron to become excited. The emission spectrum for that electron as it loses energy is measured, with the intensity of the emission at a range of wavelengths, which can indicate the relaxation pathways of the electron. When there is a short time between the excitation and emission of the electron ($\leq 10^{-8}$ sec), the process is known as fluorescence, and for longer times, the process is known as phosphorescence.

Fluorescence measurements were taken using a Perkin-Elmer LS 55 luminescence spectrometer. All samples were prepared by dispersing 10 mg of powder in 25 mL ethanol by sonication. The samples were excited at 275 nm and the emission was measured between 300 and 525 nm.

2.4.7 BET Specific Surface Area Analysis (Nitrogen Sorption Studies)

Surface area analysis is an important characterisation for photocatalytic materials. The size of the particle is inversely related to the surface area with smaller particles having larger surface areas and therefore more surface sites available for photocatalytic reactions to take place. Developed in the late 1930's the BET equation published by Stephen Brunauer, Paul Hugh Emmett and Edward Teller⁹⁵ describes the physical absorption of gas molecules on a solid surface and serves as the basis for the technique of measuring the specific surface area of a solid material.

The surface area of the samples was measured with a Quantachrome NOVA 2200 instrument with the samples degassed at 300 °C for 2 hours prior to measurement.

2.4.8 Raman Spectroscopy

Raman spectroscopy is a vibrational spectroscopy technique which uses the Raman scattering at particular wavelengths to identify chemical compounds. Raman spectroscopy is based on the theory of the inelastic scattering of light first predicted by Adolf Smekal in the 1920's and first demonstrated by Sir Chandrasekhara Venkata Raman in the 1930's. Raman used sunlight and narrow band photographic filter to create monochromatic light which was then blocked by a filter and he found that a small amount of light changed frequency and passed through the filter. Raman was awarded the Nobel Prize in 1930 for this discovery.

In Raman spectroscopy, monochromatic light is generated by a laser, illuminating the sample. The sample produces two types of scattered light, Rayleigh scatter and Raman scatter. Rayleigh scatter emerges with exactly the same energy and wavelength as the incident light and Raman scatter occurs emerges at either shorter or longer wavelengths than the incident light and is usually much less intense than Rayleigh scatter. The monochromatic light induces a vibrational transition in the sample and the photons from the laser gain or loss energy as a consequence. Raman spectroscopy is used to identify inorganic solids, which give characteristic vibrational spectra, alongside more traditional identification techniques such as X-ray diffraction, and also used to distinguish between polymorphs of materials like anatase and rutile in TiO_2 and cubic-blende and wurtzite in ZnO and ZnS .

Raman spectroscopy was carried out using a Horiba Jobin Yvon LabRAM HR 800 with an excitation laser of 532 nm used to excite the powdered samples.

2.5 Photocatalytic Testing

2.5.1 Methylene Blue Degradation

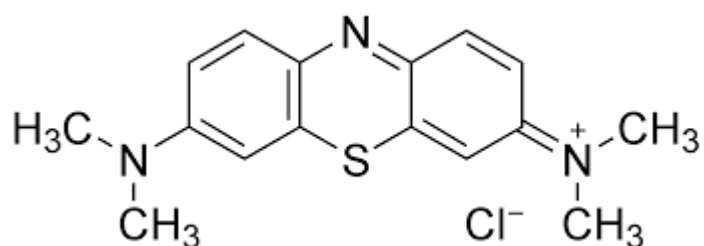


Fig 2.1 Chemical Structure of Methylene Blue

The photocatalytic rates of the samples were determined by the decolouration of an organic dye, methylene blue (figure 2.1) in the presence of the photocatalyst and illuminated using a 60-watt incandescent bulb. In a typical experiment, methylene blue (50 mL, 1×10^{-6} M) was added to the photocatalysts (0.060 g) in a glass beaker. For all samples the weight of 0.060 g was used and was not normalised for the BET area. The photocatalyst was well ground in a pestle and mortar before being used. The photocatalyst and dye were stirred in the dark for 30 minutes to allow for an adsorption of the dye on to the surface of the photocatalyst. After this, the beaker was irradiated for 2 hours with a 60-watt incandescent bulb with samples of the dye taken every 30 minutes. For all the experiments, the bulb was maintained at a height of 25 cm above the beaker. This height was established to ensure irradiation of the sample while preventing evaporation of the methylene blue solution through heating. The samples were centrifuged at 2000 rpm for 10 minutes and the degradation of the methylene blue was measured using a UV-Vis spectrometer and the photocatalytic rate and half-life determined using equation 2.5 and equation 2.6 respectively.

The photocatalytic rate, k , is measured based on the degradation of the methylene blue dye using equation 2.5,

$$\text{Ln} \frac{(A)}{(A_0)} = kt \quad \text{Equation 2.5}$$

where A is the absorbance and A_0 is the absorbance at time zero. By plotting this against time, t , the photocatalytic rate, k , is calculated from the inverse of the slope.

The half-life of the dye is calculated from the photocatalytic rate of the photocatalyst used and is shown in equation 2.6

$$\tau = \frac{\text{Ln}2}{k} \quad \text{Equation 2.6}$$

where τ is the half-life of the dye and k is the photocatalytic rate of the photocatalyst used as determined in equation 2.5. The results presented were as reported and not normalised for the surface area calculation as per BET.

In these experiments, the degradation of methylene blue in the presence of the photocatalyst is assessed as a first order rate reaction.⁹⁶ However, due to the large number of variables that may influence the rate of degradation including, concentration of the dye, available sites on the photocatalyst and the concentration of the reactive oxygen species, the degradation is not a true first order reaction.⁹⁷ In these experiments, as the concentration of the dye is so much greater than the number of available sites on the photocatalyst, the concentration can be considered a constant and the degradation assessed as a pseudo-first rate reaction. This fit is borne out as evidenced by the correlation coefficient (R^2 value) given in Tables 3.3 and 4.4

2.6 Anti-bacterial Testing

2.6.1 Agar Test Method

Agar plates were prepared using Mueller Hinton agar plate mix. The loading of the powder samples in the agar was 1% wt/wt. The agar was autoclaved at 120 °C prior to testing. After autoclaving the agar was heated to 100 °C and the photocatalyst was added to the molten agar with stirring and dispersed with sonication before being poured onto a plate. Each of the agar plates were inoculated with 50 μL *E. coli* and 50 μL of *S. aureus* suspension. Each of these suspensions were diluted to approximately 1000 colony forming unit/mL (CFU/mL). Each plate was prepared in triplicate with one sample irradiated with a light bulb (*i.e.* 3 plates irradiated) and one sample kept in the dark (*i.e.* three plates not irradiated). After irradiating the samples for 3 hours with a 60 W light bulb both sets of plates were placed in an incubator at 37 °C for 24 hours to allow any growth of the bacteria to take place. A schematic of the agar test method is shown in the figure 2.2.

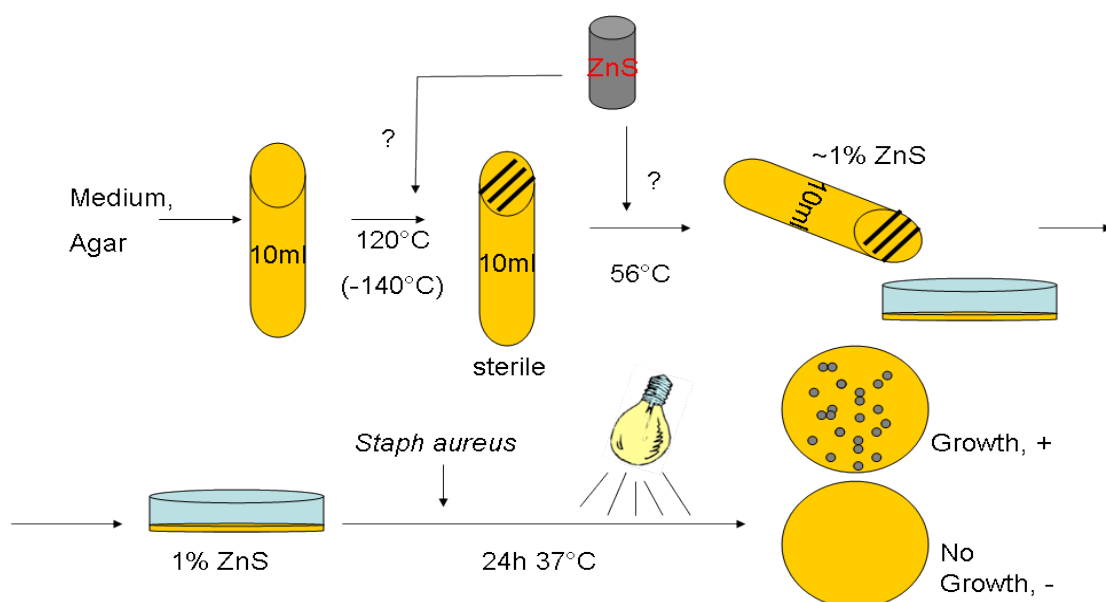


Figure 2.2: Schematic diagram of the anti-bacterial agar test method

2.6.2 Suspension Test

The suspension test (figure 2.3) measures the bactericidal effect of the photocatalyst and makes it possible to determine a time frame for the reduction in the bacterial colonies. The reference sample for these tests contained no catalyst or powder.

The reference sample consisted of 4.5 mL multi-recovery diluents (MRD) and is inoculated with 500 μL of 10^6 CFU/mL of bacteria. This gives a theoretical concentration of 10^5 CFU/mL at time zero, t_0 . The test sample contains 10 mg of photocatalyst suspended in 4.5 mL of MRD, which was then inoculated with 500 μL of 10^6 CFU/mL of bacteria. The reference and sample were both exposed to light from an 11 – watt compact fluorescent lamp, CFL, or “energy saver” light bulb for a total of 5 hours. Samples from both were taken at 0 minutes, 30 minutes, 1 hour, 3 hour and 5 hours.

**Chapter 3. Preparation and Characterisation of Microwave-
Assisted Synthesised Zinc Sulfide**

3.1 Introduction

In this chapter, the work involving the microwave synthesis is employed for the synthesis of zinc sulfide is discussed. In recent years, many different techniques have been employed for the synthesis of ZnS, including precipitation method,⁹⁸ by spray pyrolysis,⁹⁹, by hydrothermal synthesis,¹⁰⁰ in solution,¹⁰¹ using ligands,¹⁰² with conjugated polymers,¹⁰³ and using ultrasonic irradiation.¹⁰⁴ Microwave synthesis offers advantages over these other techniques because it is quite fast, simple and very energy efficient and leads to shorter reaction time, small particle sizes and narrow particle size distribution due to its rapid volumetric heating.^{105,106}

Numerous precursor materials and synthesis conditions were explored before the final synthesis scheme was arrived upon which allowed for the preparation of an indoor light active ZnS photocatalyst. The aim was have a repeatable procedure that would be relatively easy to scale up to an industrial scale. Typically microwave synthesis reactions take place in a closed Teflon lined container or using an in-built reflux system but both of these are only suitable for small scale reactions. By exploring the use of an open beaker for the reaction to take place in, it allowed for the possibility of scale up and also reduced the possibility of problems caused by pressure build up.

The prepared powdered semiconductor photocatalyst was fully characterised and the photocatalytic properties were examined under indoor light conditions using a 60 W bulb.

The anti-microbial activity of the ZnS photocatalysts was examined for both the bactericidal and bacteriostatic effects of the material.

3.2 Microwave Synthesis

A study on the effect of precursor concentration, microwave irradiation power and irradiation time was carried out to determine the effect of these factors on the formation of zinc sulfide by microwave.

A number of precursor compounds for both zinc and sulfur were examined and experimented with. For sulfide, thiourea, thioacetamide and sodium sulfate were looked at. Thioacetamide was ruled out due to the toxicity and odour of the compound and initial attempts to synthesise ZnS with sodium sulfate and zinc acetate dihydrate proved unsuccessful. Numerous zinc salts were experimented with including zinc acetate dihydrate, zinc nitrate and zinc sulfate. Synthesis attempts with zinc nitrate also proved unsuccessful with nothing precipitating during the heating phase and when all the water had evaporated there was nothing left in the beaker. Zinc sulfate was ruled out as a starting material for this sequence of experiments as the aim was to use equal amounts of zinc and sulfur in the reaction.

During the initial experimentation phase, many different precursor concentrations, irradiation times and powers, and volume of precursors were tried. It was found that if the concentration was too low that nothing precipitated and at the end of the reaction, no powder was formed. When the precursor concentration was too high, either the precursor material didn't dissolve in the water or the powder that was collected at the end of the reaction was a mix of crystalline ZnS and an amorphous mixture. If the volume of water was too low, the reaction time was not long enough for crystalline ZnS and the upper limit of precursor solutions was restricted by the size of the vessel that could be placed into the cavity of the microwave safely.

The precursor materials chosen for the preparation of the ZnS were zinc acetate dihydrate and thiourea respectively. Both of these compounds were dissolved in water

and added together in a beaker and stirred for a time to ensure the two precursors were mixed. This beaker was then placed in the microwave and irradiated. The irradiation power and volume of solution determined the irradiation time used. In each synthesis the irradiation time was long enough to allow for complete evaporation of the water and for a yellow powder to be collected from the bottom of the beaker.

Water is a polar molecule, which means it has a permanent dipole. When the irradiation begins, the high frequency electromagnetic radiation (2.45 GHz) interacts with the water. The electric dipoles present, respond to the applied electric field and a constant reorientation of the water molecules occurs. This leads to friction between the molecules which generate heat in a process called dielectric heating. It was observed during the reactions that a volume of 400 mL will reach boiling point in approximately 15 seconds. At 86 °C the thiourea molecule breaks down (equation 3.1) and liberates hydrogen sulfide, the sulfur source for the reaction. The hydrogen sulfide reacts with the liberated zinc ions (equation 3.2) to form ZnS.⁸⁸



After a time, which is determined by the initial volume of water, the yellow zinc sulfide powder precipitates out of the solution and when all the water is evaporated by continuous irradiation a yellow powder is collected. The powder was used without further treatment.

3.3 Characterisation

3.3.1 X-ray Diffraction

X-ray diffraction was employed to identify the material, determine the crystallinity and crystal phase and to estimate the particle size of the materials prepared at different irradiation powers and times, and different concentrations of starting materials.

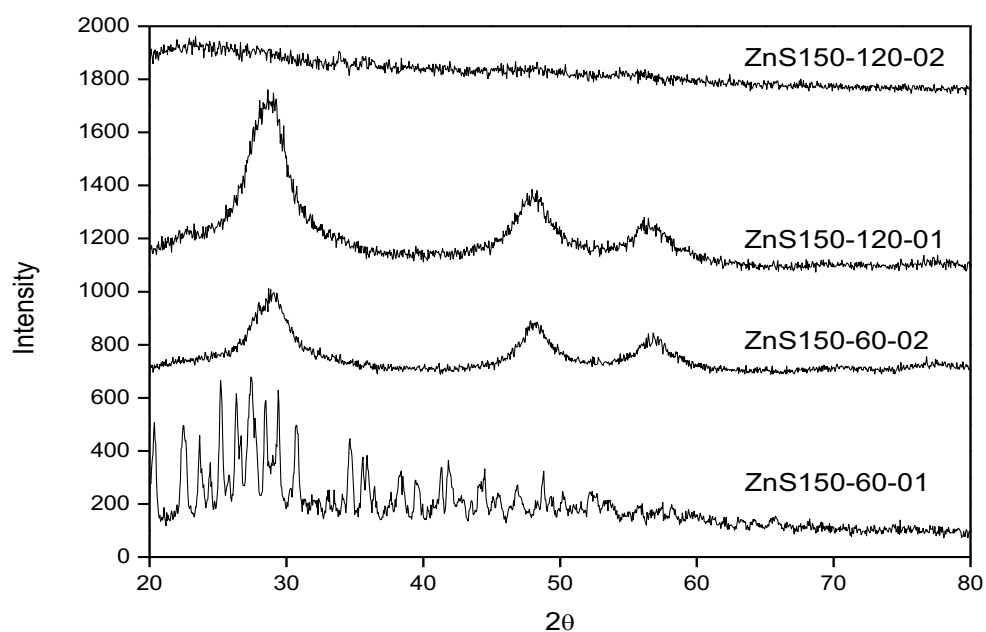


Fig 3.1 X-ray diffraction patterns of ZnS prepared at 150 W irradiation power at different irradiation times and precursor concentrations

Zinc sulfide prepared at 150 W irradiation power showed a mixture of amorphous materials prepared and cubic blende phase zinc sulfide (figure 3.1). It was determined that this irradiation power was too low to produced consistent crystalline materials. This is due to the temperature of the solutions being too low for the precursor materials to degrade as in and for a complete reaction to occur.

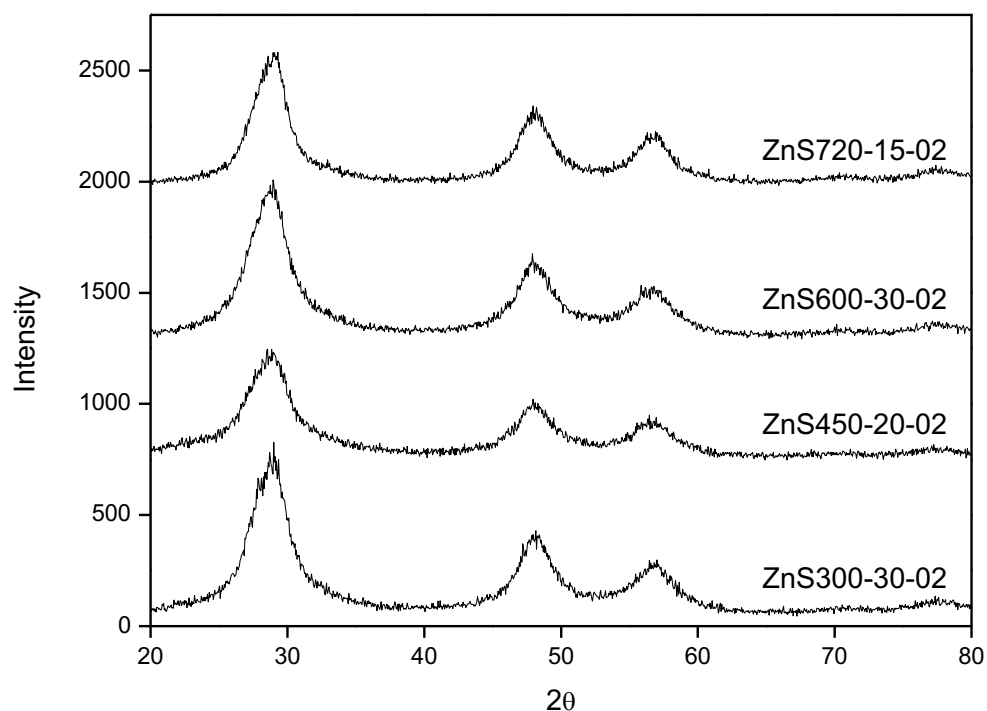


Fig 3.2 X-ray diffraction patterns for samples ZnS300-30-02, ZnS450-20-01, ZnS600-30-02 and ZnS720-15-02

For samples prepared at 300 – 720 W irradiation power (figure 3.2), all the materials were identified as crystalline cubic blende zinc sulfide when compared to the International Centre for Diffraction Data (ICDD file #05-0566)^{107,108} with the three main peaks occurring at 28 °, 47 ° and 56 ° corresponding to the (111), (220) and (311) planes respectively. The variation of concentration of the precursor and the irradiation time does not affect the crystal phase of the ZnS formed. This is a common finding in microwave synthesis of ZnS even when refluxing systems¹⁰⁹ and autoclave vessels are used. The broadening of these peaks, demonstrate that the materials are nanosized, and calculations based on the Scherrer equation (derived from the (111) peak, peak width at half height is approximately 3.6) show all particles to be less than 4 nm in size. (Table 3.1) Particle size does not change with irradiation time or power, which was also observed by Yang *et al.*⁸² and Zhu *et al.*¹¹⁰

Table 3.1 Estimated particle size from X-ray diffraction and Planes Spaces calculations for ZnS prepared by microwave synthesis

Sample Name	Plane Spaces for (111) plane (nm)	Estimated Crystallite Size (nm)
ZnS 300-30-01	0.5494	2.33
ZnS 300-30-02	0.5377	2.94
ZnS 300-60-01	0.5368	2.91
ZnS 300-60-02	0.5374	3.02
ZnS 450-20-01	0.5405	2.70
ZnS 450-20-02	0.5392	2.52
ZnS 450-40-01	0.5413	2.65
ZnS 450-40-02	0.5405	2.60
ZnS 600-15-01	0.5406	2.69
ZnS 600-15-02	0.5393	2.72
ZnS 600-30-01	0.5328	2.91
ZnS 600-30-02	0.5391	2.83
ZnS 720-15-01	0.5540	2.88
ZnS 720-15-02	0.5369	3.31
ZnS 720-30-01	0.5350	2.67
ZnS 720-30-02	0.5407	2.09

3.3.2 Scanning Electron Microscopy

Zhao *et al.*⁵⁰ found that using zinc acetate as a precursor caused large aggregates to form. This is due to the acetate molecules interacting with the forming ZnS crystals and cause agglomeration. Scanning electron microscopy (SEM) was employed to show the size of the agglomerates. Figure 3.3 shows the SEM image of ZnS-450-40-02 with agglomerations of up to 100 nm in size.

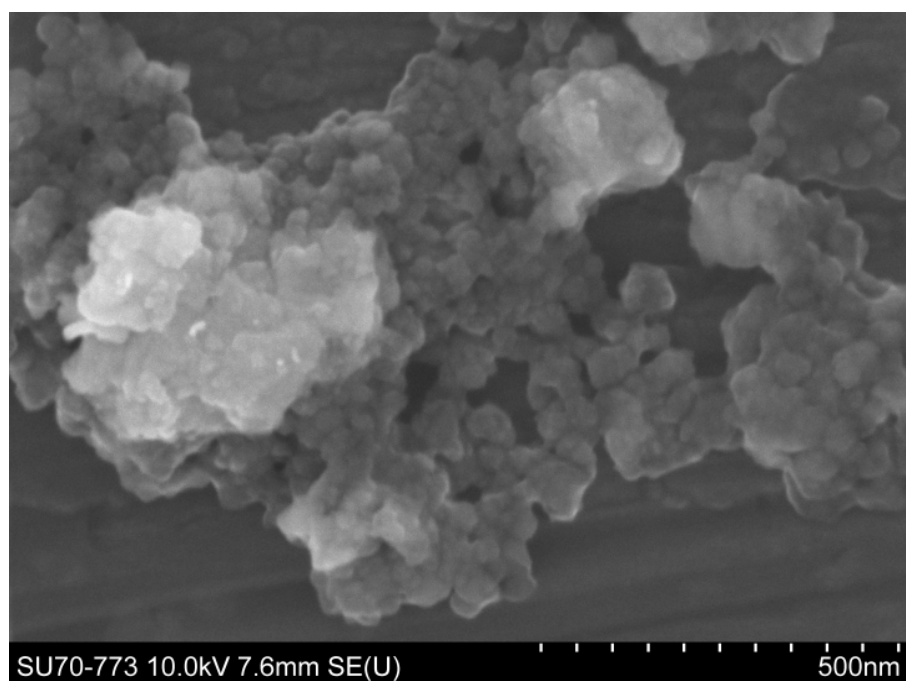


Fig 3.3. Scanning electron microscope image of ZnS450-40-02

3.3.3 Transmission Electron Microscopy

The morphology and size of the particles were further investigated using transmission electron microscopy (TEM) and high-resolution transmission electron spectroscopy (HRTEM). Figure 3.4 (A) and 3.4 (B) confirm that the powder samples are agglomerated into clusters with a large size distribution of particle sizes. The HRTEM images in figure 3.4 (C) and 3.4 (D) confirms this size distribution and show the particles to be non-uniformly shaped.

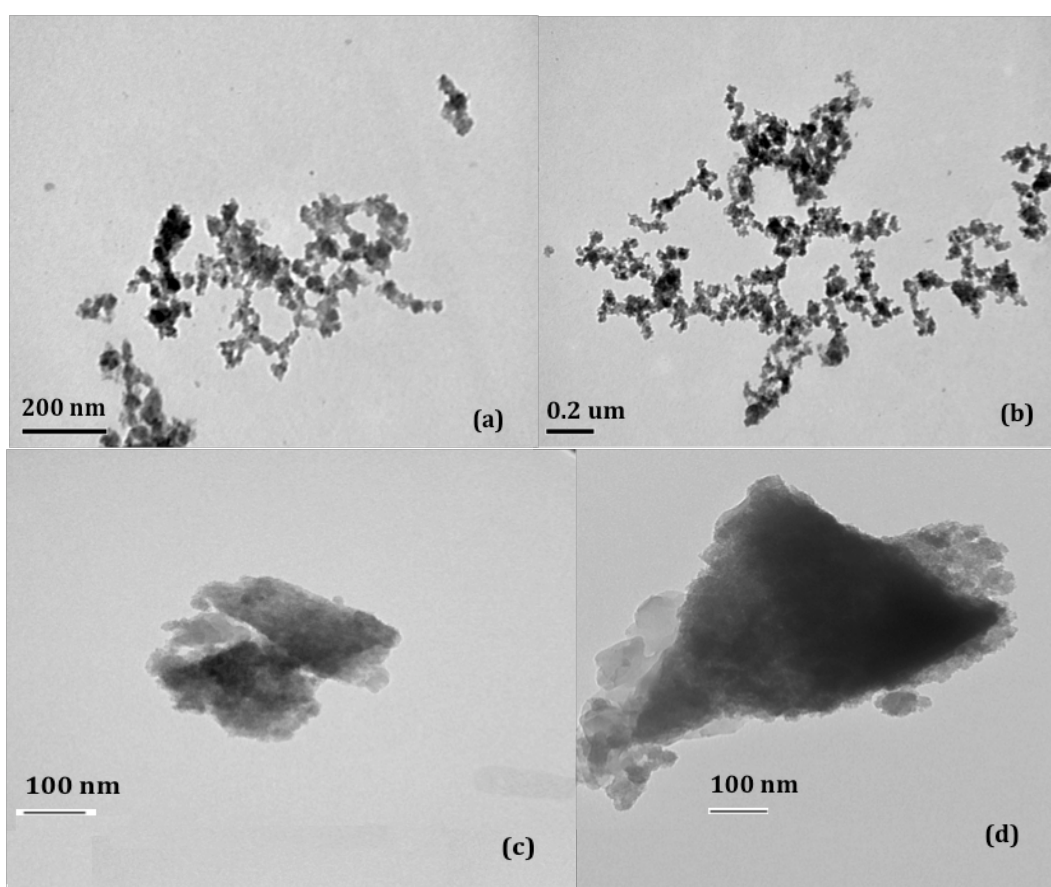
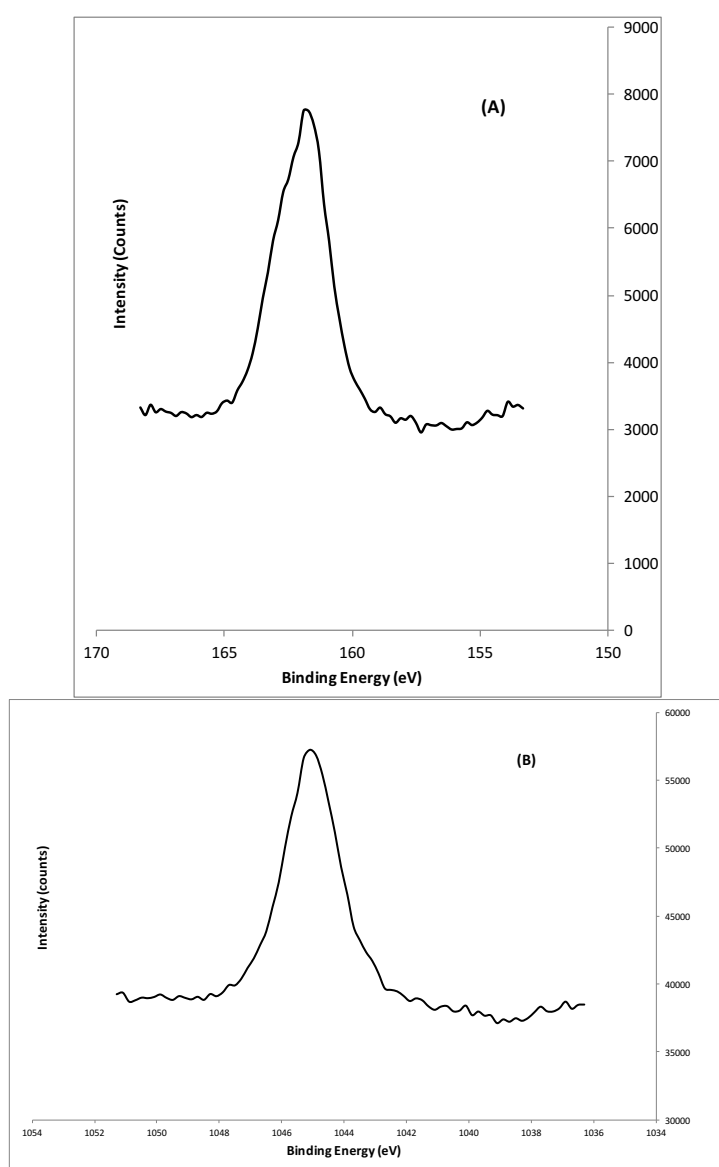


Fig 3.4 (A) and (B) TEM images of ZnS720-30-01 and (C) and (D) HRTEM images of ZnS600-30-02

3.3.4 X-ray Photoelectron Spectroscopy

X-ray photoelectron spectroscopy (XPS) was employed on a selected number of samples to confirm the identification of the materials and to look for impurities. The XPS spectra of ZnS450-20-01 (figure 3.5) shows the peaks for S 2p, Zn 2p_{1/2} and Zn 3p_{3/2} and locates these peaks at 161.9, 1045.1 and 1022.1 eV respectively which confirm the material as zinc sulfide.^{111,112}



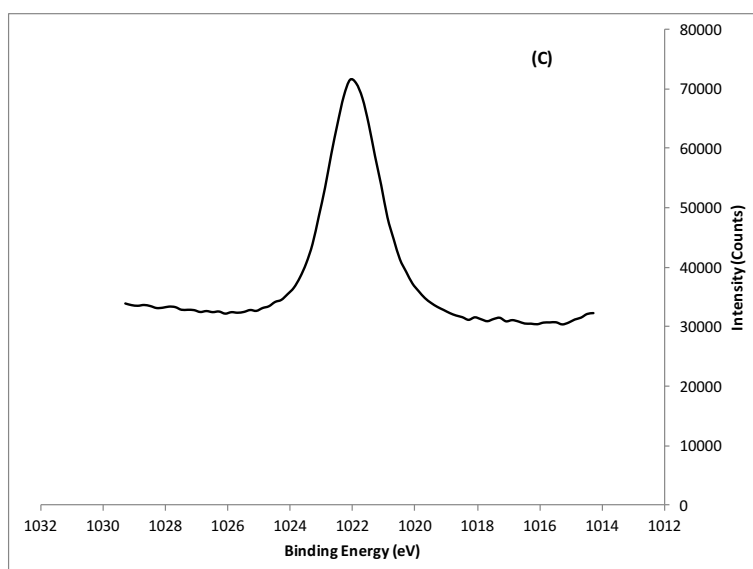


Fig 3.5. X-ray photoelectron spectra of the (A) S 2p, (B) Zn 2p_{1/2}, (C) Zn 2p_{3/2} peaks of ZnS450-20-01.

It should be noted that the S 2p spectra is composed of 2p_{3/2} and 2p_{1/2} peaks due to the spin-orbit splitting. Generally, the S 2p_{3/2} peak at lower binding energy is almost twice the intensity or area of the higher binding energy S 2p_{1/2} peak. These peaks are only around 1.1 eV from each other and cannot be resolved from one another. The survey scan (figure 3.6) and more detailed scans indicate that there is no contaminants present on the surface of the material.

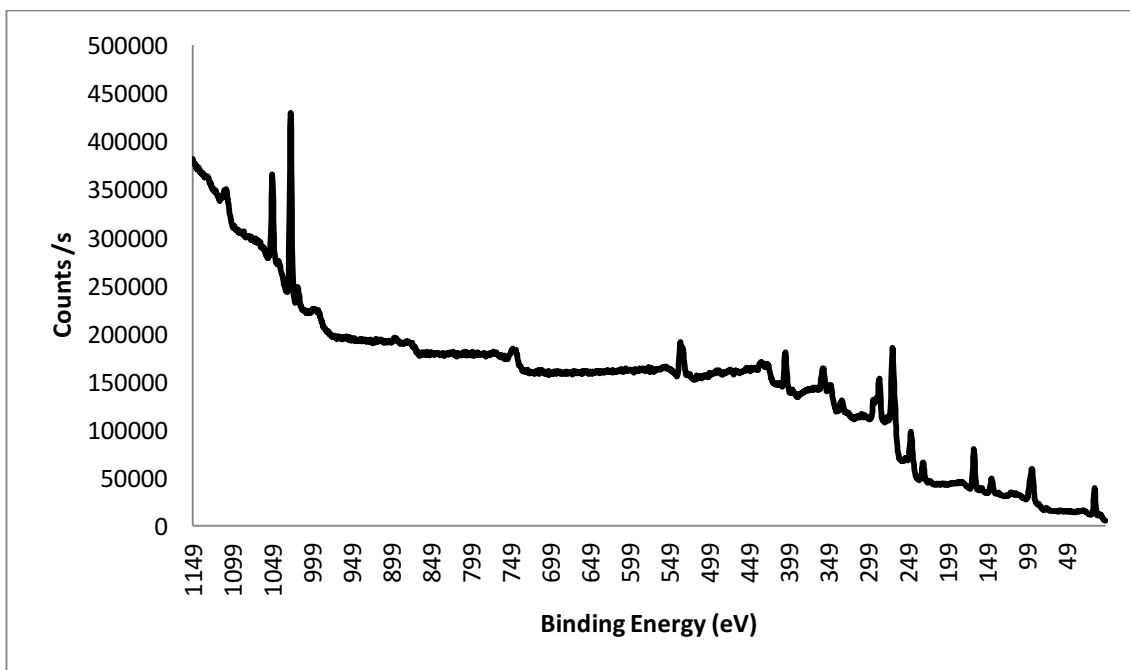


Fig 3.6 XPS survey scan of ZnS450-20-01

The survey scan shows additional peaks including peaks at 535 eV, 403 eV and 285 eV corresponding to oxygen, nitrogen and carbon respectively which are present on the surface, adsorbed from the atmosphere.

3.3.5 Diffuse Absorbance and Luminescence

The diffuse absorbance spectra of each sample was collected by preparing a KBr disc with the material and the UV-Vis spectra obtained between 800 – 200 nm. By measuring the diffuse absorbance of the material it is possible to estimate the band gap of the material and looking at the shape of the absorption curve can give an indication of the absorption characteristics of the material. The band gap of each material is shown in table 3.2.

Table 3.2 Absorption edge and band gaps of ZnS prepared by microwave heating at different power, irradiation time and precursor concentrations.

Sample Name	Absorption Edge (nm)	Band Gap (eV)
ZnS 300-30-01	342	3.6
ZnS 300-30-02	320	3.9
ZnS 300-60-01	341	3.6
ZnS 300-60-02	330	3.7
ZnS 450-20-01	310	4.0
ZnS 450-20-02	324	3.8
ZnS 450-40-01	325	3.8
ZnS 450-40-02	320	3.9
ZnS 600-15-01	324	3.8
ZnS 600-15-02	320	3.9
ZnS 600-30-01	328	3.8
ZnS 600-30-02	331	3.7
ZnS 720-15-01	346	3.6
ZnS 720-15-02	332	3.7
ZnS 720-30-01	335	3.7
ZnS 720-30-02	326	3.8

The band gaps observed for these samples are higher than that of bulk sphalerite zinc sulfide. This is due to the quantum confinement effect, discussed in section 1.8, and confirms the X-ray diffraction measurements that the particles are nanosized. Examination of the absorption spectra in figure 3.7 shows that there is an absorption shoulder in the UV-Vis spectrum. This shoulder extends to 450 nm, into the visible light region of the electromagnetic spectrum and this is evidenced by the yellow colour of the ZnS.

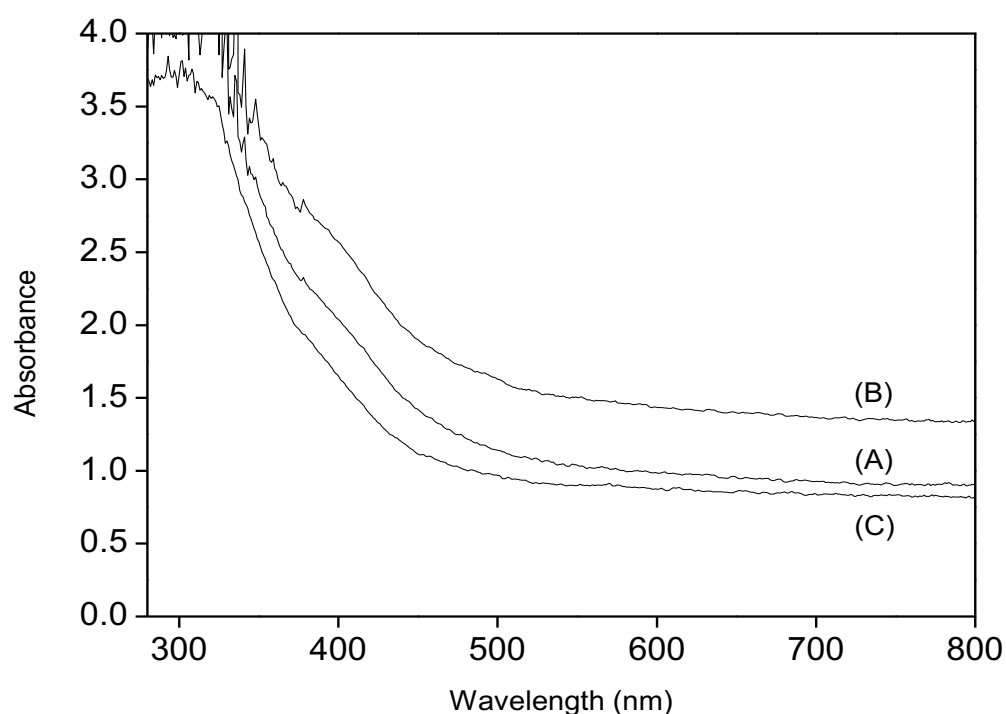


Fig 3.7. Diffuse absorbance spectra of (A) ZnS300-60-01 (B) ZnS450-40-01 and (C) ZnS600-30-02

The luminescence properties of the ZnS samples were examined by suspending the particles in ethanol and exciting the samples at 275 nm. The emission spectrum of ZnS-450-20-02 is shown in figure 3.7. The emission spectrum shows three peaks at 385 nm, 427 nm and 489 nm. These peaks correspond to 3 point defects within the ZnS crystal with 385 nm corresponding to interstitial Zn, 427 nm corresponding to S vacancies and

489 nm corresponding to Zn vacancies within the crystal.^{23,113,114,115} These defects within the crystal introduce inter-band donor levels which act as stepping stones within the band gap and allow for the transition of an electron from the valence band to conduction band even when the irradiation energy is lower than that of the band gap.

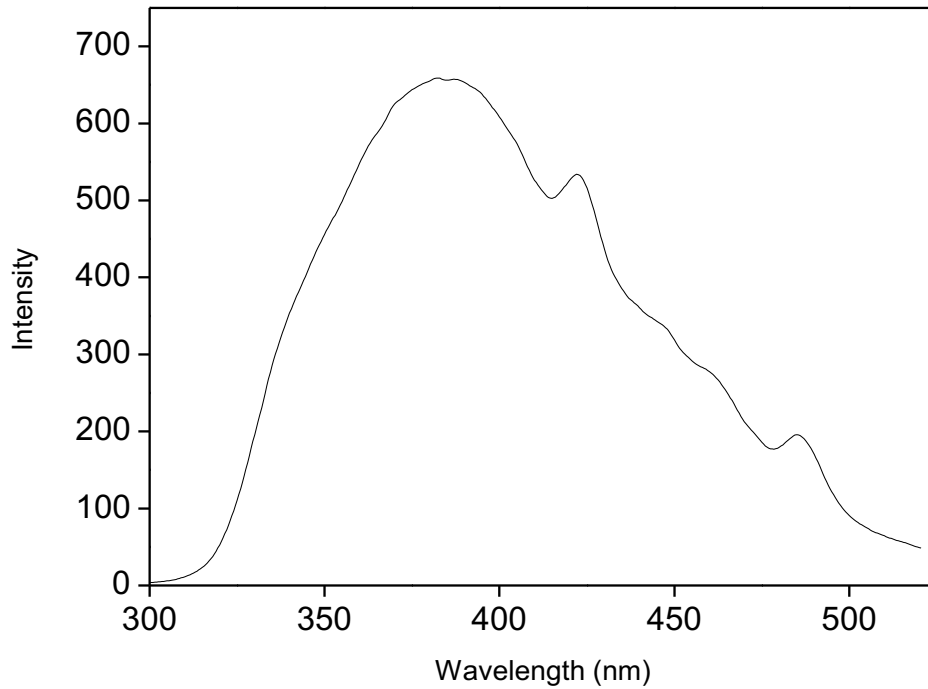


Fig 3.8. Luminescence spectra of ZnS450W excited at 275 nm.

The proposed mechanism for the inter-band donor levels is shown in figure 3.9. The donor levels energy gaps between the valence band and conduction band are 2.5 and 2.9 eV, which fall inside the region for visible light absorption and are consistent with observations in previous studies.^{23,113,114,115}

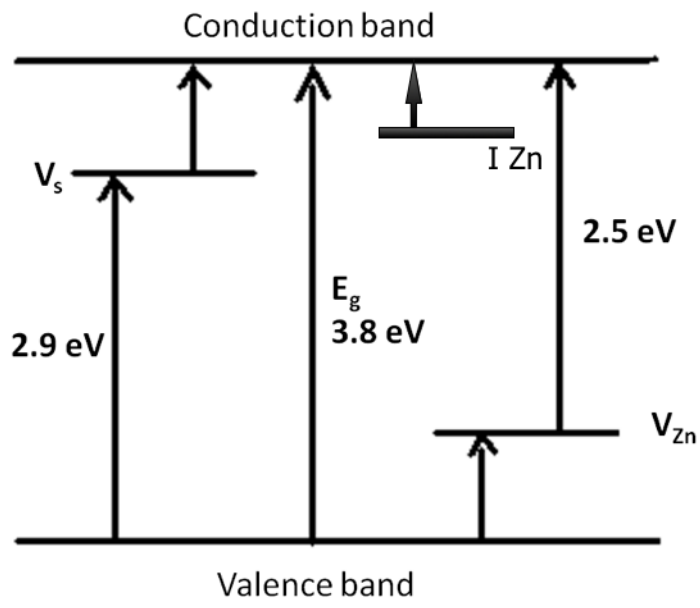


Fig 3.9. Schematic energy level diagram of microwave prepared ZnS

3.3.6 Photocatalytic Testing

Photocatalytic testing was carried out using a 60 W light bulb to simulate indoor light. The emission spectrum from the light bulb is shown in figure 3.10. The emission from the bulb occurs mainly in the visible light region of electronic spectrum with a small portion in the UV light region extending from 340 nm to 390 nm. A beaker containing 60 mg of photocatalyst and 50 mL of 1×10^5 M methylene blue solution was stirred in the dark for 30 minutes to allow for any absorption of the dye onto the surface of the photocatalyst. The beaker and light source were enclosed so that no other light source could interfere with the experiment.

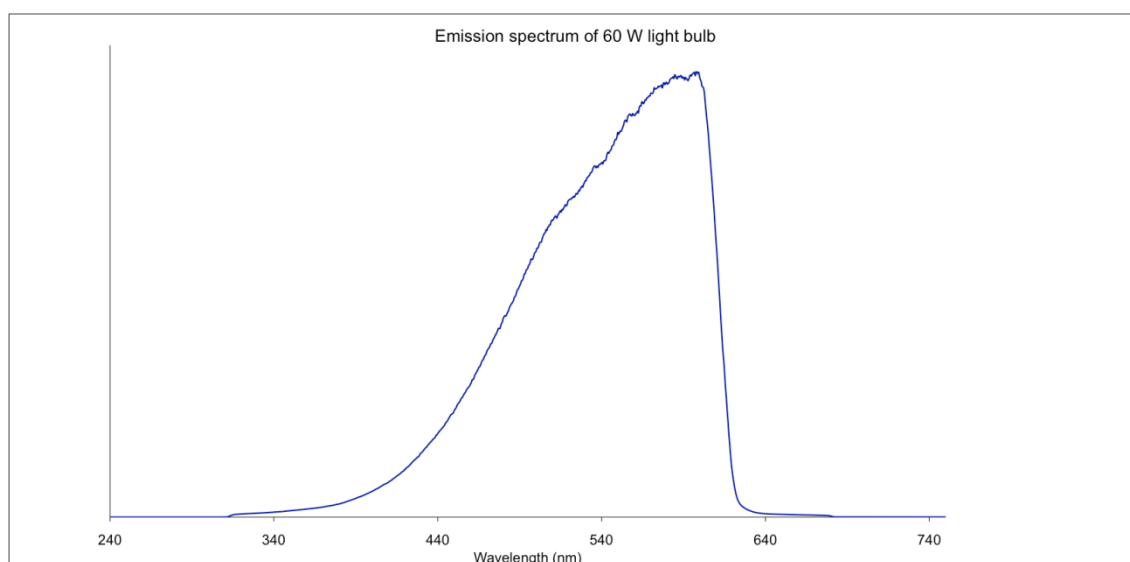


Fig 3.10 Emission spectrum of the 60 W light bulb used for the photocatalysis and anti-bacterial studies

The dye was exposed to light for 2 h with constant stirring and samples taken every 30 minutes. The samples were centrifuged before a reading was taken on the UV-Vis spectrometer between 800 nm and 400 nm. Table 3.3 shows the calculated photocatalytic rate of the degradation of the dye in the presence of each photocatalyst. The photocatalytic rate was calculated by plotting $\ln(A/A_0)$ versus *time (min)*, where A is the absorbance of the dye at λ_{\max} and A_0 is the absorbance of the dye at λ_{\max} at time zero. The half-life, τ , of the dye can be subsequently determined from the $\tau = \ln 2/k$, where k is the photocatalytic rate of degradation of methylene blue in the presence of the photocatalyst. Each experiment was performed in triplicate.

For the as prepared materials, the ZnS720-15-02 (figure 3.11) showed the highest photocatalytic activity at 0.006 min^{-1} . This is 6 times higher than the blank (no photocatalyst powder) and 2 times higher than Degussa P25 titanium dioxide which was used as reference photocatalyst. The other reference material was ZnS purchased from Sigma Aldrich with a particle size of approximately 10 microns. This reference had a photocatalytic activity comparable with the blank. The increase in the photocatalytic activity can be explained by two factors. The first is the smaller size of the microwave prepared ZnS, at 3 – 4 nm in size, there is a larger surface area than those of the reference materials meaning more photocatalytic sites available. The second is due to the electronic properties of the microwave ZnS. As shown in section 3.2.2.5 these materials absorb light in the visible light region where most of the light from the bulb used is emitted. These results show that the prepared samples are capable of degrading organic material in an indoor light environment.

Table 3.3 Photocatalytic rate and half life of methylene blue in the presence of ZnS prepared by microwave heating at different power, irradiation time and precursor concentrations.

Sample Name	Photocatalytic Rate (min ⁻¹)	Correlation Co-efficient (R ² value)	Half Life (min)
Blank	0.001	0.7898	693
Sigma Aldrich ZnS	0.001	0.9425	693
Degussa P25 TiO ₂	0.003	0.97485	239
ZnS 300-30-01	0.003	0.93056	241
ZnS 300-30-02	0.003	0.87492	238
ZnS 300-60-01	0.004	0.93675	170
ZnS 300-60-02	0.005	0.94053	138
ZnS 450-20-01	0.004	0.96056	168
ZnS 450-20-02	0.004	0.9588	165
ZnS 450-40-01	0.005	0.99281	138
ZnS 450-40-02	0.005	0.9893	140
ZnS 600-15-01	0.005	0.9769	140
ZnS 600-15-02	0.004	0.97794	166
ZnS 600-30-01	0.005	0.97251	142
ZnS 600-30-02	0.005	0.97808	144
ZnS 720-15-01	0.005	0.94021	142
ZnS 720-15-02	0.006	0.99108	119
ZnS 720-30-01	0.005	0.97644	140
ZnS 720-30-02	0.005	0.95124	138

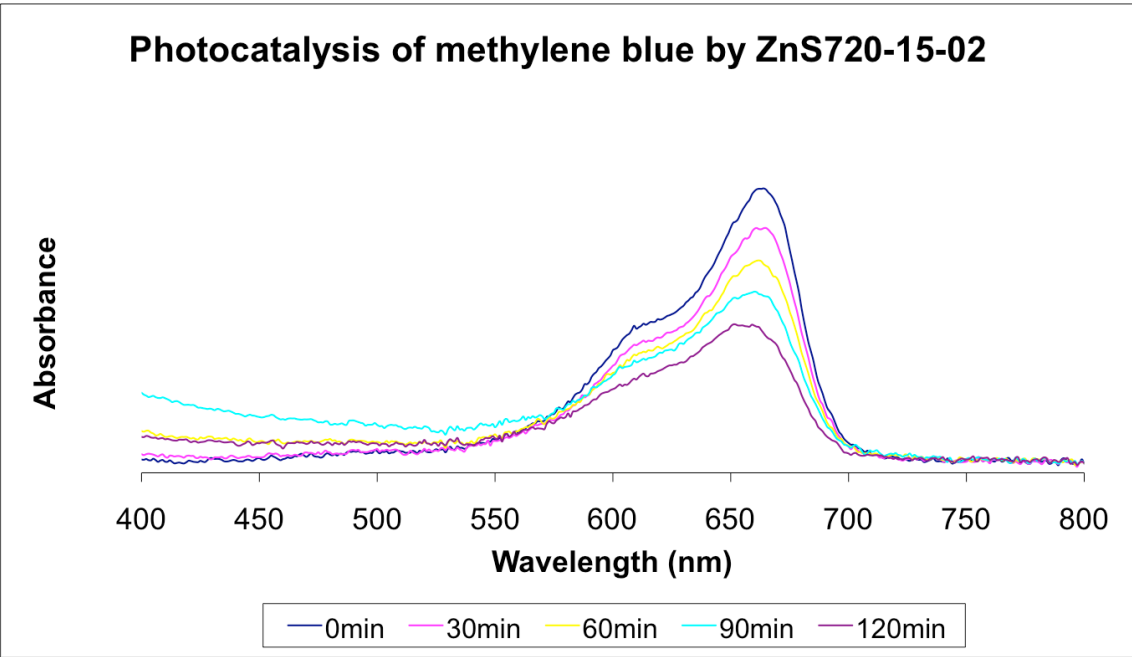


Fig 3.11 Absorbance spectra of methylene blue in the presence of ZnS720-15-02 over 2 hours

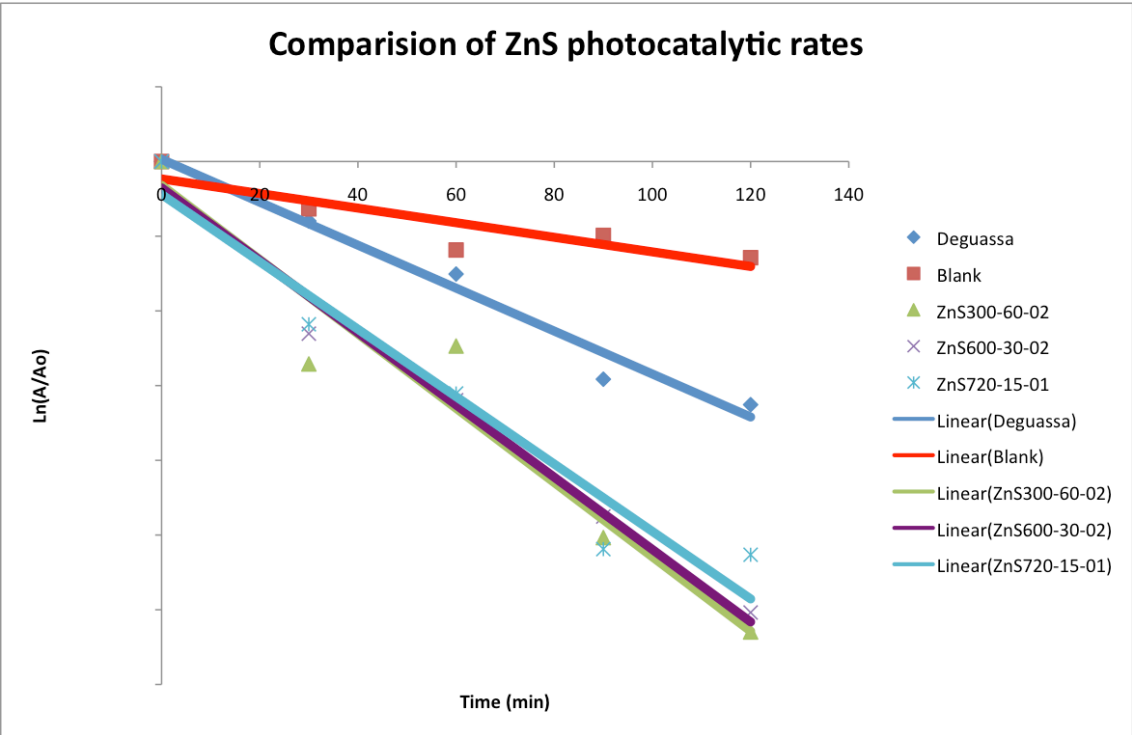


Fig 3.12 Comparison of blanks and a selection of ZnS samples degradation rates

3.3.7 Antibacterial Testing

The microwave prepared ZnS was tested for its anti-bacterial activity under irradiation from an indoor light source, a 60 W bulb. The ZnS sample tested was ZnS-300-30-02, the sample irradiated at 300 W for 30 mins using 0.2 M concentration solutions of precursors. Three references were used, a blank, Degussa P25 TiO₂, a commercial photocatalyst and Sigma – Aldrich ZnS.

Initial testing involved using a concentration of 1% w/w of the photocatalyst in Müller Hinton agar. Each plate was inoculated with 50 µL *E. coli* and 50 µL *S. Aureus* suspensions (concentration of the suspensions was approximately 1000 CFU/mL). The plates were irradiated using an indoor light source (60 W light bulb) or kept in the dark for 3 h and each sample had a plate prepared in triplicate for each lighting condition. After the light/no light exposure the plates were incubated at 37 °C overnight. It was found that the ZnS produced in the microwave had anti-bacterial properties and both light and dark conditions at a 1% w/w photocatalyst to agar concentration. (Table 3.4)

It was postulated that the reason the ZnS showed anti-bacterial activity in both the light and dark conditions was due to the small particle size and high concentration of the material dispersed in the agar which affected the colony growth.

Figure 3.13 shows agar with no photocatalyst present, exposed to light (a) and kept in the dark (b). Both plates show growth of *E. coli* and *S. Aureus* bacterial colonies. Figure 3.14 shows agar with 1%w/w loading of the Sigma Aldrich ZnS reference material, exposed to light (a) and kept in the dark (b). Both plates show growth of *E. coli* and *S. Aureus* bacterial colonies.

Table 3.4 Anti-bacterial results of ZnS300-30-02 and controls

Sample	Details	Light Exposure		No Light exposure	
		L+		L-	
Blank Agar	No photocatalyst	<i>E. coli</i>	<i>S. aur</i>	<i>E. coli</i>	<i>S. aur</i>
		Growth	Growth	Growth	Growth
ZnS	Sigma Aldrich ($<10 \mu\text{m}$)	Growth	Growth	Growth	Growth
TiO ₂	Evonic Degussa Nanopowder	Growth	Growth	Growth	Growth
ZnS	0.2 M precursors, 300 W, 60 min	No Growth	No Growth	No Growth	No Growth

Figure 3.15 shows agar with 1%w/w loading of the titanium dioxide reference material, exposed to light (a) and kept in the dark (b). Plate (c) is plate (b) with a differently exposed photograph to show more clearly the growth of the bacterial colonies. Both plates show growth of *E. coli* and *S. Aureus* bacterial colonies. The agar in figures 3.14 and 3.15 show a white colouring due to the presence of ZnS and TiO₂ respectively. Figure 3.16 shows the agar with 1%w/w loading of the microwave prepared ZnS, exposed to light (a) and kept in the dark (b). It is clear from these images that there was no growth of bacteria when the colonies are inoculated on plates containing ZnS.

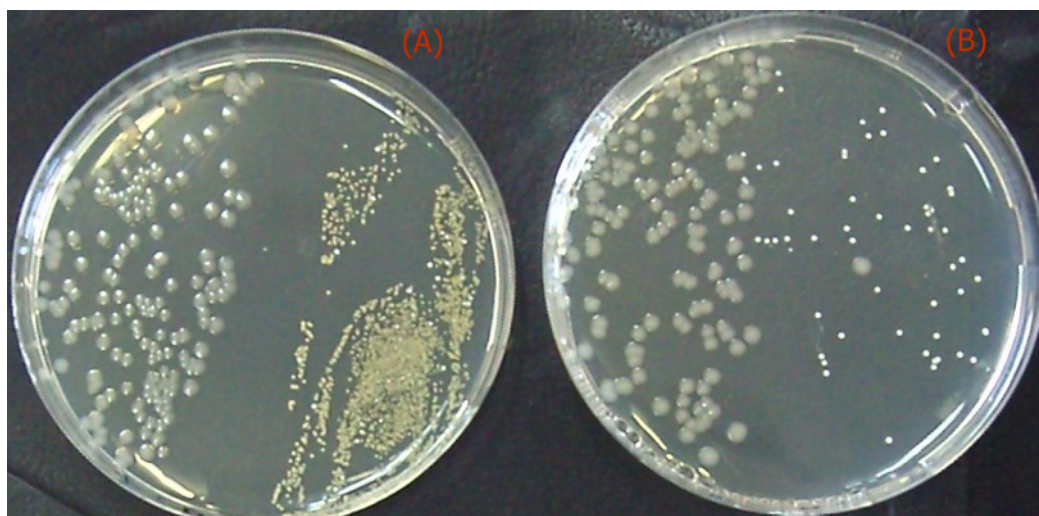


Fig 3.13 Petri dishes of (a) blank agar plate inoculated with *E. coli* and *S. aureus* exposed to light and (b) blank agar plate inoculated with *E. coli* and *S. aureus* not exposed to light.



Fig 3.14 Petri dishes of (a) Sigma-Aldrich ZnS agar plate inoculated with *E. coli* and *S. aureus* exposed to light and (b) Sigma-Aldrich ZnS agar plate inoculated with *E. coli* and *S. aureus* not exposed to light.

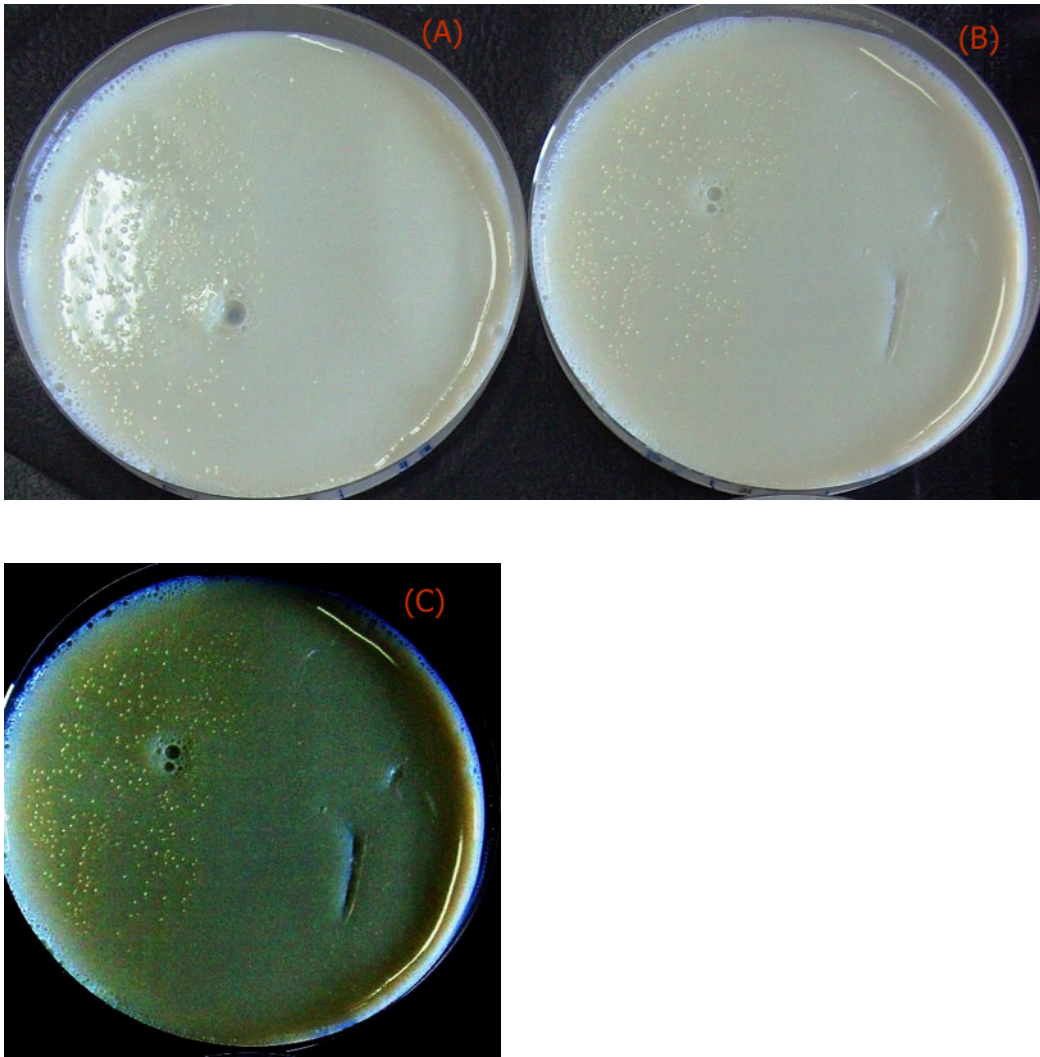


Fig 3.15 Petri dishes of (A) TiO_2 agar plate inoculated with *E. coli* and *S. aureus* exposed to light and (B) TiO_2 agar plate inoculated with *E. coli* and *S. aureus* not exposed to light and (C) different exposure of TiO_2 agar plate inoculated with *E. coli* and *S. aureus* exposed to light to enable visualisation of bacteria which is similar in colour to the titanium dioxide.

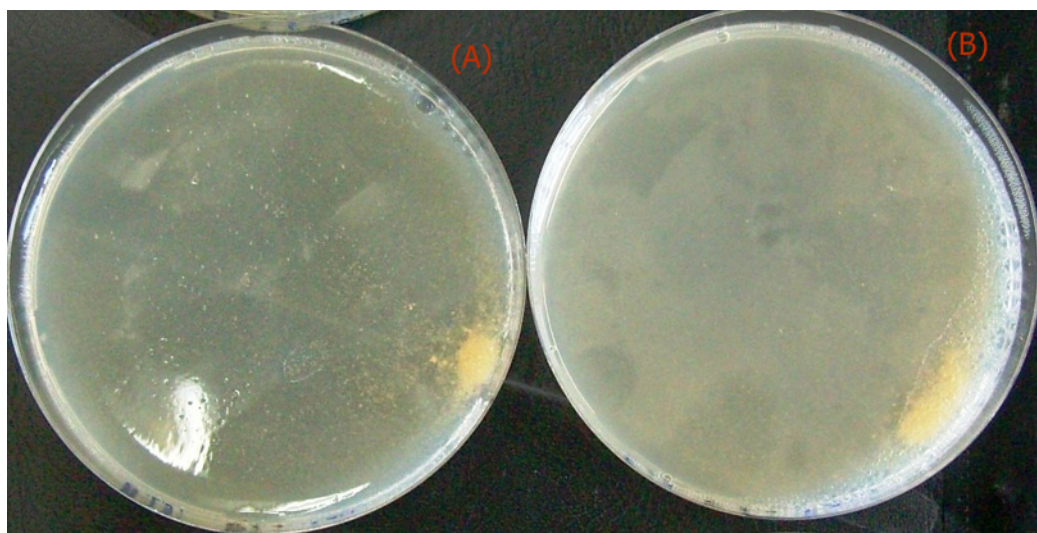


Fig 3.16 Petri dishes of (a) ZnS300-30-02 agar plate inoculated with *E. coli* and *S. aureus* exposed to light and (b) ZnS300-30-02 agar plate inoculated with *E. coli* and *S. aureus* not exposed to light.

To determine the minimum inhibition concentration of ZnS required to effectively prevent the growth of the bacterial colonies, plates containing 0%, 0.25% and 0.75% ZnS were inoculated with *E. coli*, *S. aureus* and *P. aeruginosa*. Each plate was prepared in triplicate and exposed to light from a 60 watt bulb for 3 h, with a control plate kept in the dark for the same period. The plates were kept overnight in an incubator at 37 °C.

The plate containing no catalyst showed growth of all three bacteria in both light and dark conditions. At 0.25% w/w loading, in the dark conditions both the *S. aureus* and *E. coli* grew colonies, however on the plates exposed to light the growth of *S. aureus* was partially inhibited while the growth of *E. coli* colonies was fully inhibited. This is an indication of photocatalytic action against the bacteria by the microwave synthesized ZnS. At 0.75 % w/w loading inhibition of *E. coli* and *S. aureus* bacteria was observed in both light and dark conditions; however the growth of *P. aeruginosa*, a species resistant to many anti-bacterial agents, was not affected.

These tests showed that the ZnS acts as a bacteriostatic material preventing the growth of the test microbes in both light and dark conditions at concentrations above 0.75% w/w and that photocatalytic action takes place when the samples are exposed to light at concentration as low as 0.25% w/w.

To observe the bactericidal effects of the material a suspension test was designed. The reference samples contained no catalyst and comprised of 4.5 mL of maximal-recovery diluent (MRD) and were inoculated with 500 μ L of 10^6 CFU/mL of bacteria. The test samples contained 10 mg of ZnS300W suspended in 4.5 mL of MRD, which was inoculated with 10^6 CFU/mL of bacteria. This gave a concentration of 10^5 CFU/mL of bacteria in each sample. The reference and test samples were exposed to light from the 60 watt bulb for 5 h with samples taken at 0 min, 30 min, 1 h, 3 h and 5 h and the concentration of bacteria was measured at each time point. Table 3.5 shows the concentration of bacteria at each time point for both the reference and test sample and figure 3.17 shows a graph of the relative concentrations of bacteria. The test showed that there was an 88% reduction in the amount of bacteria in 5 h and showed the material to be bactericidal.

Table 3.5. Concentrations of the bacterial suspension test for the reference and test samples.

Time	0 h	0.5 h	1 h	3 h	5 h
Reference CFU count	8.7×10^5	5.8×10^5	6.7×10^5	1.4×10^6	2.2×10^6
Sample CFU count	5.8×10^5	2.7×10^5	2.2×10^5	1.5×10^5	7.3×10^4

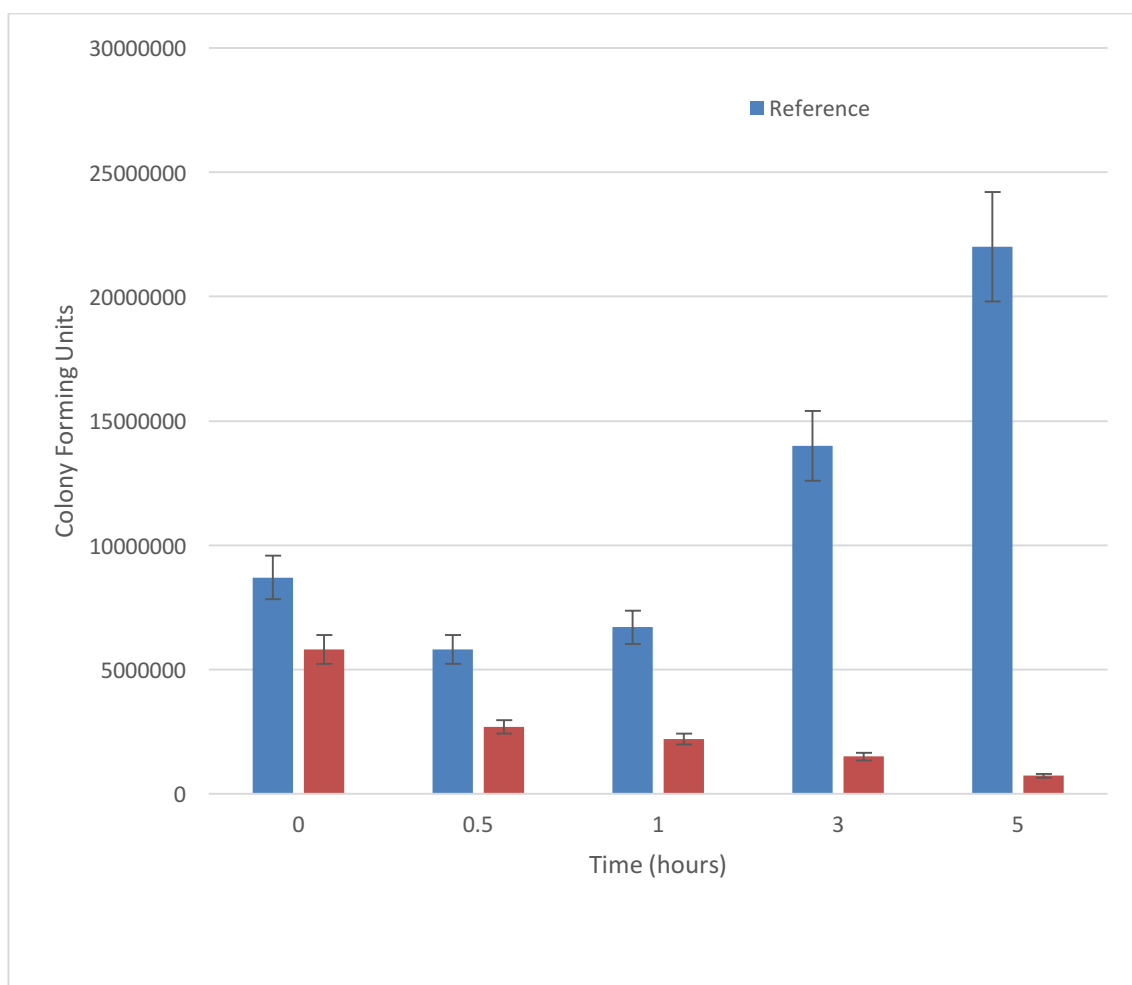


Figure 3.17 Bacterial concentration of reference and ZnS300W sample to test the degradation rate of the photocatalyst.

This study where the concentration of ZnS is varied and previous studies have shown that the anti-bacterial effect of the semiconductor is concentration dependant.^{116,117} The increase in ZnS concentration leads to a decrease in the bacterial concentration, and in this study when the concentration was above 0.75% w/w of the agar, no bacterial colonies of *S. aureus* or *E. coli* were observed. It has been found that below the concentration threshold for which the ZnS is harmful to the bacteria that the number of bacterial colonies actually increases due to the fact that bacteria can metabolise Zn^{2+} at low concentrations.¹¹⁶ A number of factors may play a role in the antibacterial effect of

ZnS. *S. aureus* has an efflux mechanism for Zn^{2+} which suggests that free cations on the surface of the material is toxic to the bacteria.¹¹⁸ Oxidative species such as superoxide anions and singlet oxygen can be generated on the surface of the photocatalyst after irradiation with light¹¹⁹ will also assist in the degradation of the cell membrane of the bacteria which leads to loss of cellular components and induces cell death.^{120,121} The small size of the nanoparticle as shown by the broadening of the XRD peaks a larger surface area for contact with the bacteria also increases the antibacterial activity of the ZnS.

3.4 Conclusion

A novel ambient pressure microwave synthesis route for producing nanoparticles of ZnS was achieved. Many starting materials, synthesis parameters including irradiation time, volume of precursors, concentration of precursors and irradiation power were explored to find a feasible method which could easily be scaled up.

The ZnS particles prepared were fully characterised and found to 3-4 nm in size, which has agglomerated to clusters of approximately 100 nm and irregular shapes. X-ray photoelectron spectroscopy and X-ray diffraction showed that crystalline cubic blende phase sphalerite ZnS was formed with no contaminants or other crystal forms present.

The electronic properties were examined and it was found that the band gap of the material was larger than that of the bulk ZnS due to the nanosized nature of the particles and the quantum confinement effect. Despite this larger band gap the material showed absorbance and emission at wavelengths in the visible light region of the electromagnetic spectrum. This was assigned to defects in the crystal introducing donor levels within the band gap and reducing the amount of energy required for an electron to transition from the valence band to the conduction band of the photocatalyst.

Photocatalytic degradation of methylene blue was carried out and showed the microwave prepared ZnS capable of degrading organic material in an indoor light environment. The materials rate was 6 times higher than the blank and 2 times higher than the reference photocatalytic materials.

Anti-bacterial studies showed that the ZnS was both bactericidal and bacteriostatic towards *E. coli* and *S. aureus*. The minimum inhibition concentration was determined to 0.25%w/w loading for the agar and at this concentration, evidence of photocatalytic

activity against the bacteria was observed with growth on the plate kept in the dark and no growth on the plate exposed to the light.

Chapter 4: Group 13 metal doped ZnS

4.1 Introduction

The band gap of zinc sulfide of 3.7 eV allows for photocatalytic activity to be initiated under irradiation of light of a wavelength of 335 nm meaning that UV light is required. The aim of modifying ZnS by doping with metals is to improve the photocatalytic activity under indoor light irradiation by modifying the band gap of the semiconductor.

Metal doping of semiconductors has a long history with many applications in the electronics industry, such as gallium doping of silicon to prepare a p-type semiconductor. Doping has also been used in photocatalytic research where metal ion doping of semiconductors and solar cells has been used to change the band structure, optical properties and recombination rates of the photocatalytic material.

Metal doping of zinc sulfide to improve the photocatalytic activity of the material has been widely reported. Kudo *et al.*¹²² prepared ZnS doped with ionic copper, nickel and lead, which induced visible light absorbance in ZnS by reducing the effective band gap to 2.5 and 2.3 eV respectively and this improved the photocatalytic generation of hydrogen under visible light irradiation. Arai *et al.*¹²³ prepared hollow Cu-doped ZnS shells which also produces hydrogen from alkaline solutions under visible light, while the undoped samples show no photocatalytic activity when exposed to visible light. Kohtani *et al.*¹²⁴ also doped ZnS with copper, nickel and lead to induce visible light photocatalytic action. The application of this study was the photo-reductive defluorination of hexafluorobenzene and found that not only did lead and copper extend the photocatalytic response into the visible region but the metals also acted as redox sites for the photoreductive defluorination. Cadmium doping of zinc sulfide has also been carried out to prepare visible light active catalyst. In the study by Xing *et al.*,¹²⁵ cadmium of different levels was doped into the ZnS crystal, there was a range of absorption edges and hydrogen production efficiencies based on the level of doping.

The most common properties of ZnS exploited are its luminescence and phosphorous properties and a wide variety of metal dopants have been used to tune the luminescent intensity and emission wavelengths of ZnS. Manganese is the most common metal used,^{126,127,128,129,130,131,132,133} with numerous reports for silver,^{134,135,136} cobalt,^{137,138,139} copper,^{140,141,142,143,144} nickel^{145,146,147} and elements from the lanthanide series^{148,149,150}. These phosphors have wide ranging applications including DNA markers, biosensors, lasers, LEDS and other photonic devices¹²²⁻¹⁴⁶.

It is clear from the previous reports that there are a number of experimental factors that affect the metal properties including loading of the dopant, use of a co-catalyst, synthesis technique and sintering temperatures. Varying these conditions, including increasing the dopant level can remove all photocatalytic activity of the semiconductor.

In this chapter, a study on the effect metal doping of ZnS by the group 13 metals, prepared by microwave assisted synthesis was carried out. Group 13 consists of the elements boron, aluminium, gallium, indium and thallium. Boron is a non-metallic element and so was excluded from this study as was thallium due to the toxic nature of elemental thallium and its salts. The three remaining elements, aluminium, gallium and indium are all soft metals whose ionic radii are much smaller than the atomic radii of the elements. The three elements all have a 3+ oxidative state and the ions are formed by the removal of three electrons from the outer shell, 1 *p* electron and 2 *s* electrons. These electrons are relatively far from the nucleus and the loss of these, combined with increased effective nuclear charge attracting the remaining electrons, the ionic radii are relatively small. The fact that these three elements form a 3+ ion also means that they are non-equivalent impurities in ZnS and any substitution for the Zn²⁺ cation by the dopant cations could result in increased numbers of electron traps and crystal defects

which affect the surface chemistry and the photocatalytic properties of the semiconductor

Table 4.1 Physical and chemical properties of the Group 13 metals

	Aluminium	Gallium	Indium
Atomic No.	13	31	49
Melting Point	933 K	303 K	430 K
Density	2698 kg m ⁻³	5905 kg m ⁻³	7290 kg m ⁻³
Oxidation States	+3	+3	+1, +3
Appearance	silvery white metal	soft silver metal	soft silvery metal

Aluminium was the first of these elements to be isolated by Hans Oersted, in 1825 by reduction of aluminium chloride. Hans Oersted was a chemist and physicist who discovered that electric currents create magnetic fields in 1820. Aluminium has its name derived from the Latin word 'lumen' which translates to 'bitter salt'. Aluminium is the 3rd most abundant element in the earth's crust after oxygen and silicon and is the most abundant metallic element, accounting for over 8% of the weight. It is non-toxic, has a relatively low density, high thermal conductivity and is highly corrosion resistant. These chemical and physical properties mean that aluminium has a large number of widely varied uses including being the main component of aircraft fuselages, food storage, aluminium foil and modern car shells.

Gallium was discovered fifty years later in France by P. E. Lecoq de Boisbaudran in 1875, four years after its existence and properties were predicted by Dimitri Mendeleev. De Boisbaudran isolated the element following examination of mineral sphalerite and observed gallium's characteristic a two violet line spectrum. The name gallium is derived from the Latin word for France, 'Gallia'. The main use of elemental gallium is

to produce low temperature alloys, as its melting point is nearly room temperature at only 303 K. Gallium has one of the largest liquid ranges of the metallic elements, 2370 K, and so is used in thermometers where a large temperature range is required. Gallium is also used in modern electronics where is used to form semiconductors, solid state transistors and LED's. Gallium has no biological function, however the gallium (III) ion can mimic the function of iron (III) ion and in bacterial species that uptake gallium can cause death as it binds to the same sites as iron (III) but does not allow redox reactions to happen during respiration as iron (III) does.

Indium was first isolated in 1863 by two German chemists Ferdinand Reich and Hieronymus T. Richter. While searching zinc based minerals for the then known thallium Reich, being colour-blind, asked Richter to observe the spectrum for him. Instead of the green emission lines they expected for thallium, Richter observed a blue line in the emission spectrum. At the time no element with that emission spectrum was known so they concluded that they had discovered a new element. Richter first isolated the metal a year later and indium was named after the Latin 'indicum' which means indigo or violet for the spectral line colour that was observed. Indium has a wide range of uses in the electronics industry with its alloys used in transistors, thermistors, photoconductors and is used to form low temperature alloys. Indium is also a component of indium tin oxide (ITO), a transparent conductive coating used in LCD's, touch screens, solar cells and as a coating on aircraft windshields.

The group 13 metals aluminium, gallium and indium have been used previously to enhance the photocatalytic activity of ZnS but a systematic study on the effects of the group has not been published.

4.2 Photocatalyst Synthesis

Aluminium oxide, Al_2O_3 was used as the source for aluminium in Al – ZnS samples, indium acetate, $\text{In}(\text{C}_2\text{H}_3\text{O}_2)_3$, was used as the indium source in the In – ZnS samples and gallium oxide, Ga_2O_3 , was used as the gallium source in the Ga – ZnS samples. A 0.04 M aqueous solution of each of the impurities was prepared with sonication and varying amounts, equal to 0.2% - 2% dopant level, was added to 200 mL each of 0.2 M zinc acetate dihydrate solution and 0.2 M thiourea solution. The overall solution was mixed prior to irradiation in an open beaker at 600 W for 30 minutes. After this time had elapsed and a 5 minute cool down period, the beaker was removed from the microwave and a dry yellow powder was collected. The powder was characterised without further treatment.

4.3 Characterisation

4.3.1 X-ray Diffraction

X-ray diffraction was used to determine the crystallinity and the crystal phase of the samples. Figure 4.1 shows the XRD patterns for ZnS and Al doped ZnS samples and all were found to be cubic blende phase of ZnS with the peaks at 28° , 47° and 56° corresponding to the (111), (220) and (311) diffraction planes respectively.

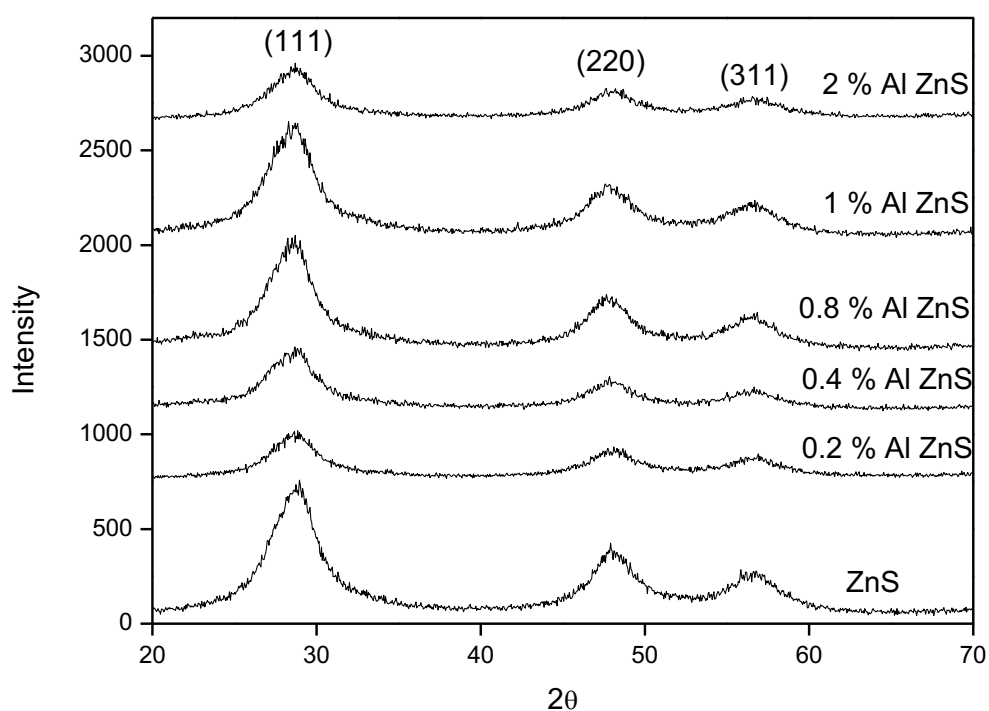


Fig 4.1. X-ray diffraction patterns of ZnS and aluminium doped ZnS prepared by microwave synthesis

Figures 4.2 and 4.3 show the X-ray diffraction patterns for the gallium doped ZnS samples and the indium doped ZnS samples. All samples show the cubic-blende sphalerite structure for zinc sulfide. Investigations of the diffraction patterns also show that there are no peaks present from impurities or phase transformations occurring with the increasing dopant concentration. For all three dopants there is no change in the crystallinity of the ZnS with increasing dopant concentration (peak width at half height

is approximately 3.6 for ZnS and doped ZnS samples). While metal doping can lead to increased crystallinity of ZnS,¹⁵¹ it appears that under a microwave irradiation synthesis the presence of the dopants doesn't effect the crystallisation of the ZnS. The formation of ZnS crystals and the crystal structure is strongly dependent on the synthesis conditions and the effects of additives on the surface energy of growing crystals.¹⁵² The addition of capping agents¹⁵³ and metals¹⁵⁴ has been shown to reduce the crystallinity in microwave-assisted synthesis of ZnS due to the effect on the surface energy and the shorter reaction times compared to the traditional synthesis techniques.

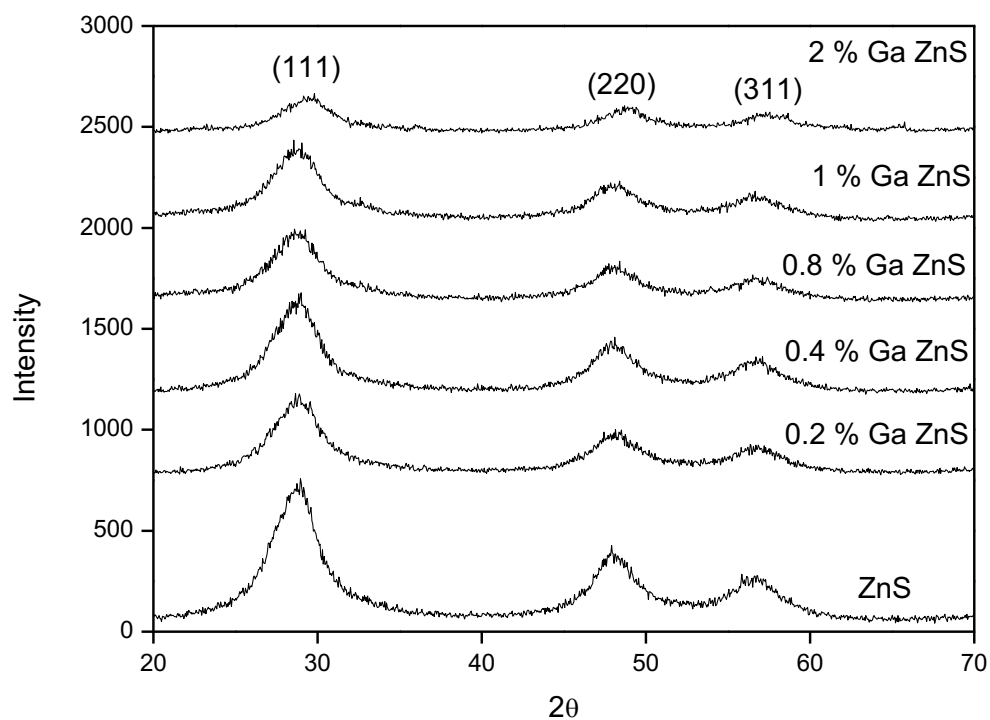


Fig 4.2. X-ray diffraction patterns of ZnS and gallium doped ZnS prepared by microwave synthesis

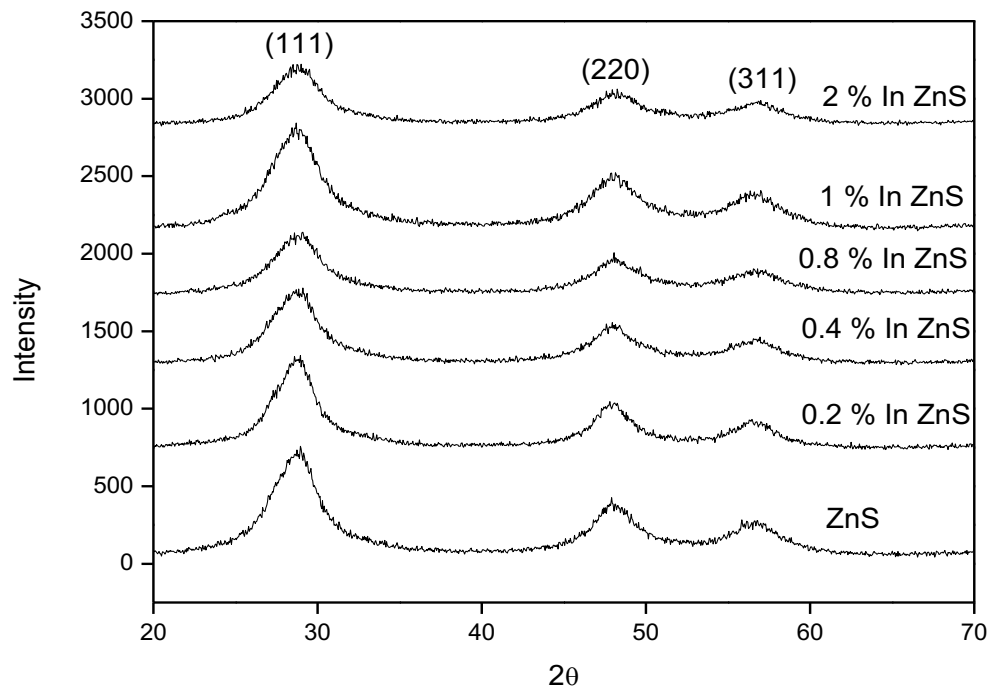


Fig 4.3. X-ray diffraction patterns of ZnS and indium doped ZnS prepared by microwave synthesis

The broad peaks present in figures 4.1 to 4.3 suggest that the particles are nanosized and calculations based on the Scherrer equation (derived from the (111) peak) show that all crystallites are less than 4 nm in size.

4.3.2 Diffuse Absorbance

Diffuse absorbance spectroscopy was employed to determine the effect of the dopants on the optical properties of zinc sulfide as shown in figure 4.4 for aluminium, figure 4.5 for gallium and figure 4.6 for indium. The samples were prepared by pressing a KBr disc with a sample to KBr ratio of 1:10.

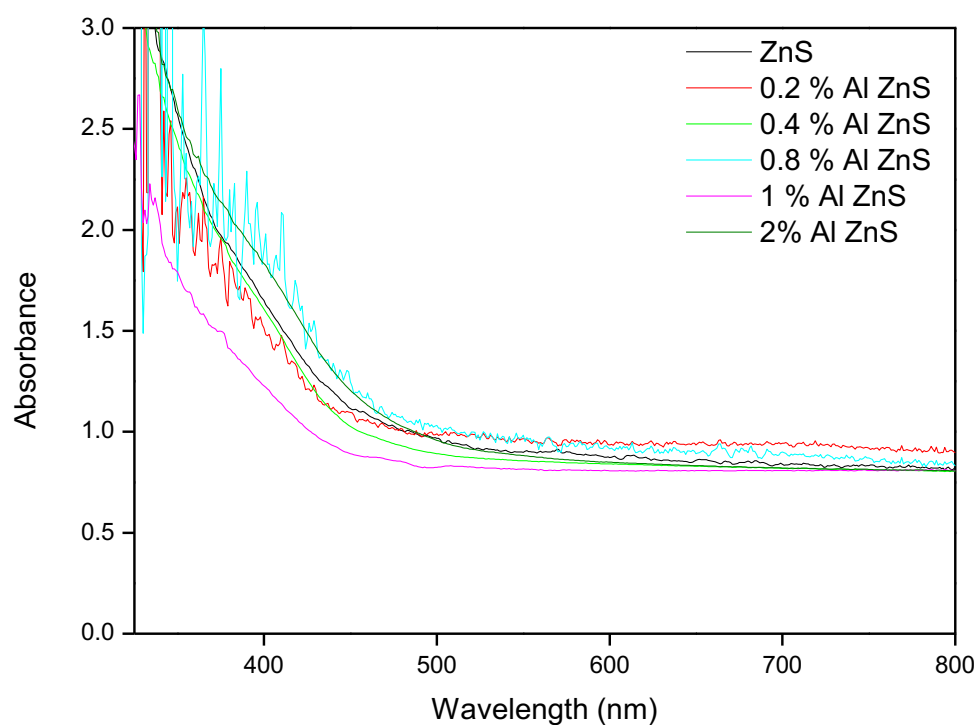


Fig 4.4. UV-Vis diffuse absorbance spectra of ZnS and Al – ZnS samples prepared by microwave synthesis

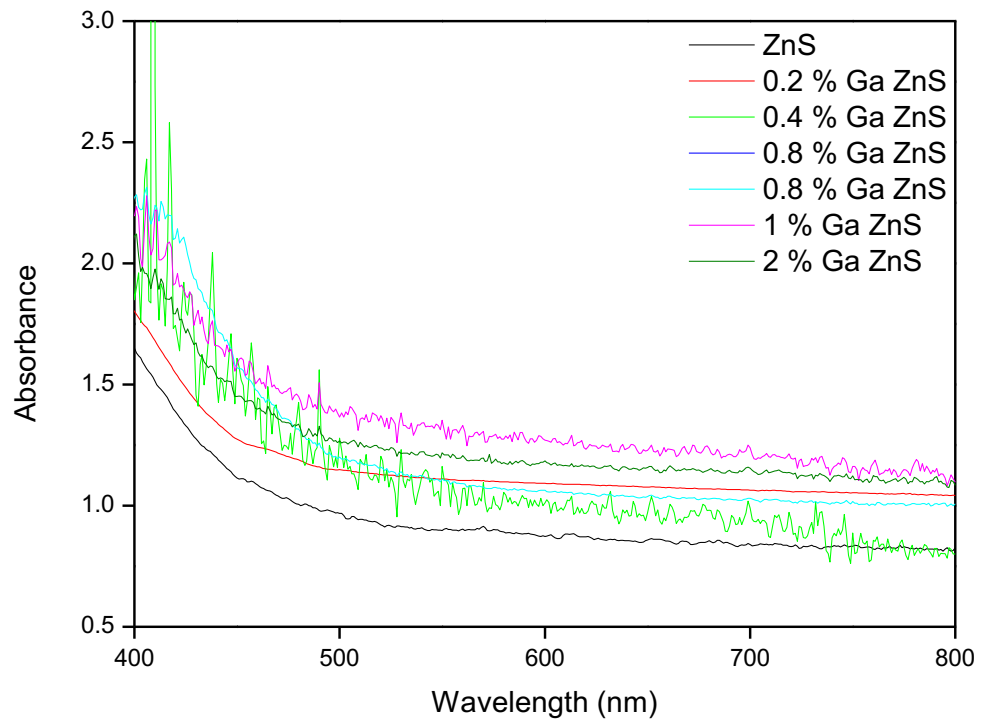


Fig 4.5. Diffuse absorbance spectra of ZnS and gallium doped ZnS prepared by microwave synthesis

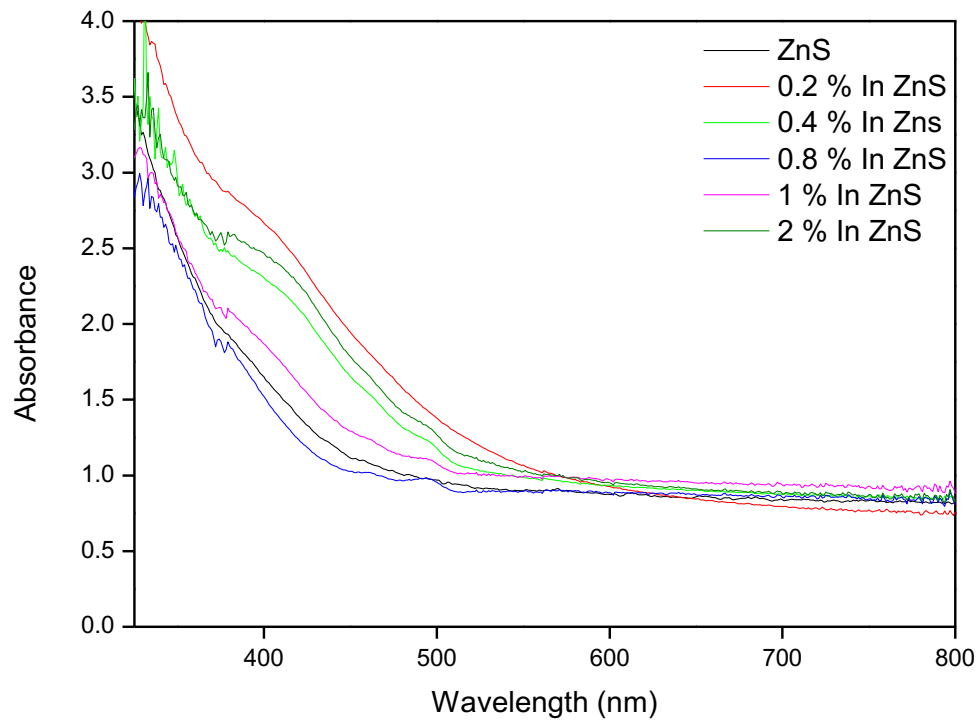


Fig 4.6. Diffuse absorbance spectra of ZnS and indium doped ZnS prepared by microwave synthesis

The diffuse absorbance spectra show no change in the aluminium doped and gallium doped samples compared to undoped ZnS sample which suggests that aluminium and gallium have no effect on the optical properties of ZnS at these dopant levels and this is consistent with the results reported by Nagamani *et al.*¹⁵⁵ The absorption edge for these samples is between 320 and 340 nm which equates to a band gap of 3.8 to 4.0 eV for these materials, larger than the band gap of bulk ZnS, 3.7 eV due to the quantum confinement effect associated with nanosized materials. For the indium doped materials an absorption shoulder in the spectrum appears which allows absorption of visible light irradiation by the semiconductor. This is also observed by the fact that the indium doped samples were darker in colour than the aluminium and gallium doped ZnS. The dopants are present as ions in reaction vessel and the ionic radii for Al^{3+} , Ga^{3+} and In^{3+} are 0.054 nm, 0.068 nm and 0.080 nm respectively. The ionic radius of Zn^{2+} is 0.074 nm. This

means that the aluminium and gallium ion can both replace the Zn^{2+} ion and fit into the interstitial space between the Zn^{2+} and S^{2-} ions. The indium ions are in the zinc sites in ZnS and due the difference in the covalence between the In^{3+} and Zn^{2+} the indium doping causes distortions and point defects in the ZnS crystal, including interstitial Zn and S atoms and vacancies at the Zn and S sites. Previous work by Peng,¹⁵⁶ Scocioreanu¹⁵⁷ and Mehta¹⁵⁸ have shown that these defects can act as inter-band donor levels and this reduce the energy required to promote an electron from the valence band to the conduction band in the semiconductor and this is represented by the large absorption shoulder in the diffuse absorbance spectra of indium doped zinc sulfide.

4.3.3 Photoluminescence

Photoluminescence spectroscopy was also employed to investigate the optical properties of the doped samples. Luminescence measurements were obtained by excitation of the samples suspended in ethanol at a wavelength of 275 nm.

In Chapter 3 the luminescence of the undoped zinc sulfide samples was described in detail with emission peaks observed at 385, 427 and 489 nm assigned to interstitial Zn^{2+} , S^{2-} vacancies and Zn^{2+} vacancies respectively. For samples doped with aluminium and gallium, no effect in the on the luminescent intensity of wavelength of the emissions was observed. These results compliment the results observed in section 4.2.1.2 for the diffuse absorbance spectra where no changes were observed for the aluminium and gallium samples compared to the undoped ZnS samples.

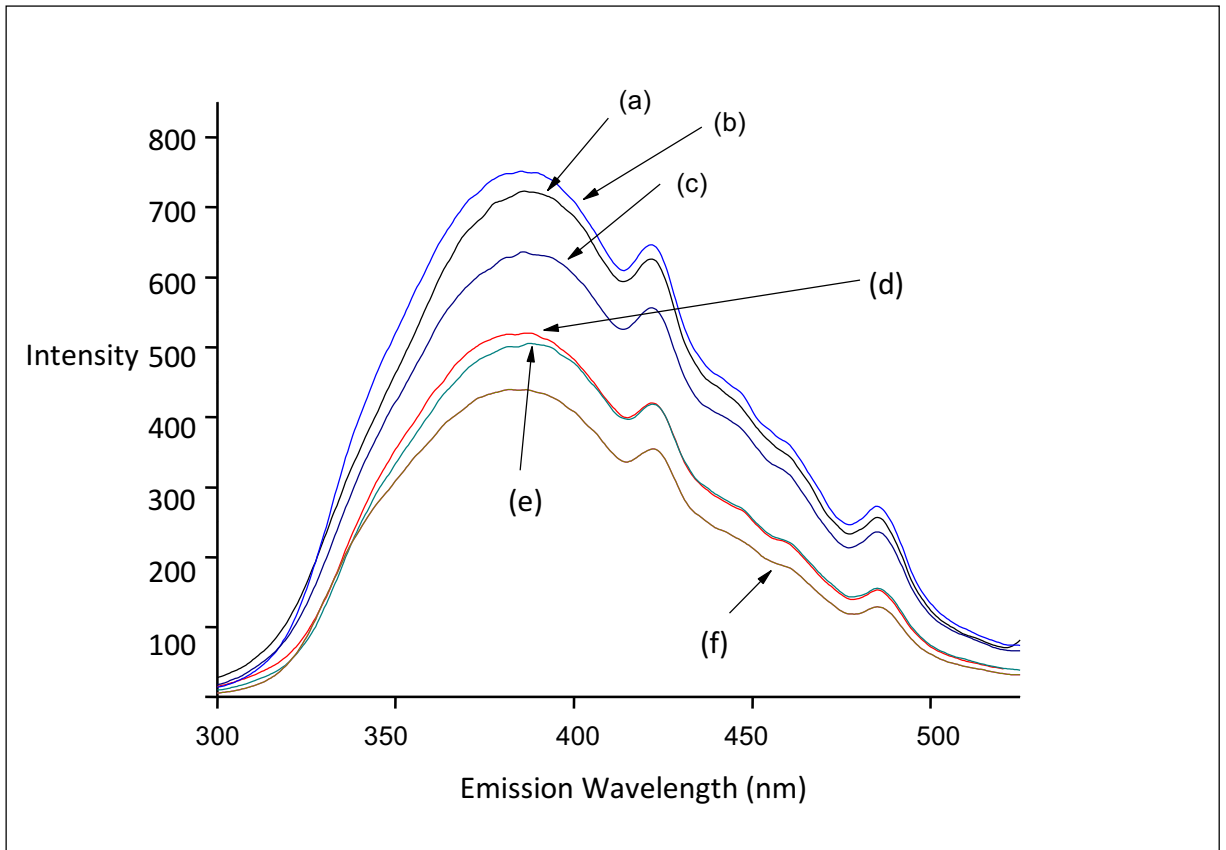


Fig 4.7: Emission spectra of (a) ZnS600-300-02 (b) 0.2 % In-ZnS (c) 0.4 % In-ZnS (d) 0.8 % In-ZnS (e) 1 % In-ZnS and (f) 2% In-ZnS

The emission spectra of the indium doped samples shown in figure 4.7 show a decrease in the emission intensity as the amount of dopant level is increased. This result counters the results observed by Yang *et al*¹⁵⁹ who found that at lower doping levels the fluorescence emission intensity increased but above a 1 mol% dopant level the intensity decreased. It is believed the increase is due to increase in the number of electron – hole pairs being created by the substitution of the In^{3+} into Zn^{2+} sites within the crystal. In the experiments carried out in this study, the decrease in emission intensity is attributed to a number of factors caused by the indium doping. Firstly, the indium ions are not equivalent to zinc ion ($\text{In}^{3+}/\text{Zn}^{2+}$). The non-equivalency is due to the difference in charge between the ions and so in indium substitution, there is a slightly positive charge on the indium ion when bound to the sulphur ions within the crystal structure. These slightly positive sites can act as electron traps so under excitation, electrons promoted

from the valence band to the conduction band are not returned as they would in an undoped sample therefore reducing the radiative recombination and the emission intensity.

As this decrease in emission is only observed in the indium doped samples and not in the aluminium and gallium doped samples, it would suggest that the indium doping occurs by substitution of the Zn^{2+} ion by In^{3+} ions but that the aluminium and gallium doping occurs through interstitial doping. This would be expected due the indium ionic radius being larger than that of the zinc ionic radius and the ionic radii of aluminium and gallium being smaller than zinc as demonstrated in section 4.3.3.

4.3.4 Surface Area Analysis

Surface area plays a significant role in the ability of a photocatalyst to degrade pollutants and the larger the surface area, the higher the activity of the catalyst. The surface area of each sample was calculated using the Brunauer-Emmett-Teller (BET) equation which measures the absorption of a monolayer of N_2 molecules on the surface of the catalyst. The results in table 1 (the average of three individual analysis) show that by introducing doping the surface of the catalyst increases by about 10%. An increase in the surface area is expected as a dopant is introduced in the ZnS crystal as the dopant leads to distortion of the surface.¹⁶⁰ This would be a factor in the improved photocatalytic activity of the doped materials by the virtue of more sites being available on the surface of the material for photocatalysis to occur.

Table 4.2. Surface area of photocatalysts as calculated from BET analysis

Sample	Surface Area (m²/g) ± 5 m²/g
ZnS	86
0.2% Al ZnS	107
0.4% Al ZnS	108
0.8% Al ZnS	110
1% Al ZnS	111
2% Al ZnS	110
0.2% Ga ZnS	104
0.4% Ga ZnS	106
0.8% Ga ZnS	104
1%Ga ZnS	107
2 %Ga ZnS	108
0.2% In ZnS	98
0.4% In ZnS	98
0.8% In ZnS	102
1% In ZnS	100
2% In ZnS	101

4.3.5 X-ray Photoelectron Spectroscopy

X-ray photoelectron spectroscopy (XPS) was used for the indium doped samples to further characterise the crystal structure and look at the effect of indium doping on the samples. Table 4.3 shows the peak locations for zinc, sulfur and indium in the indium doped samples. In all of these samples no other impurities were detected.

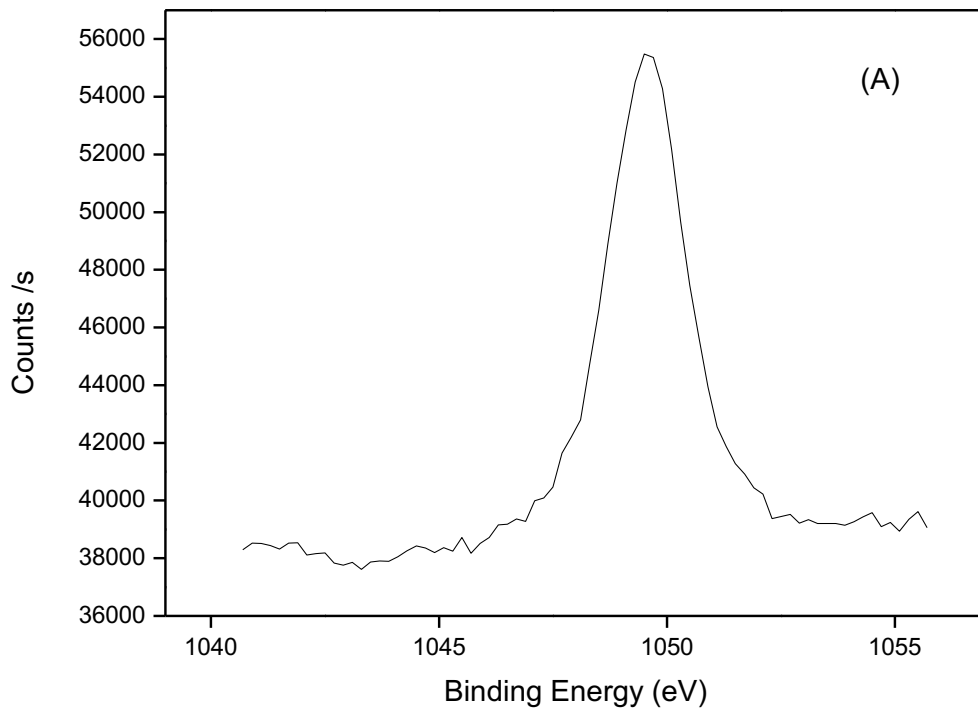
Table 4.3 Binding energies for XPS analysis of indium doped samples

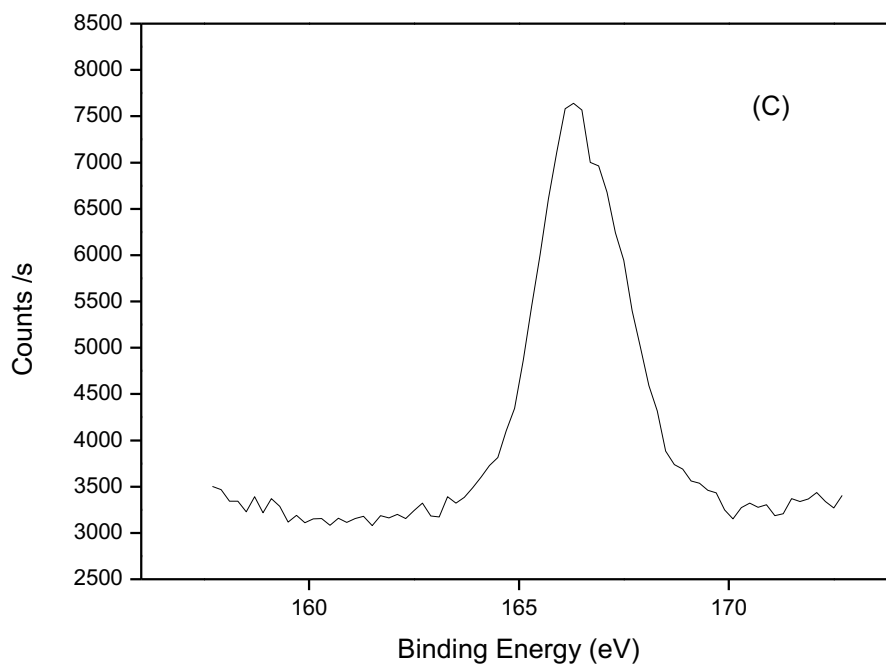
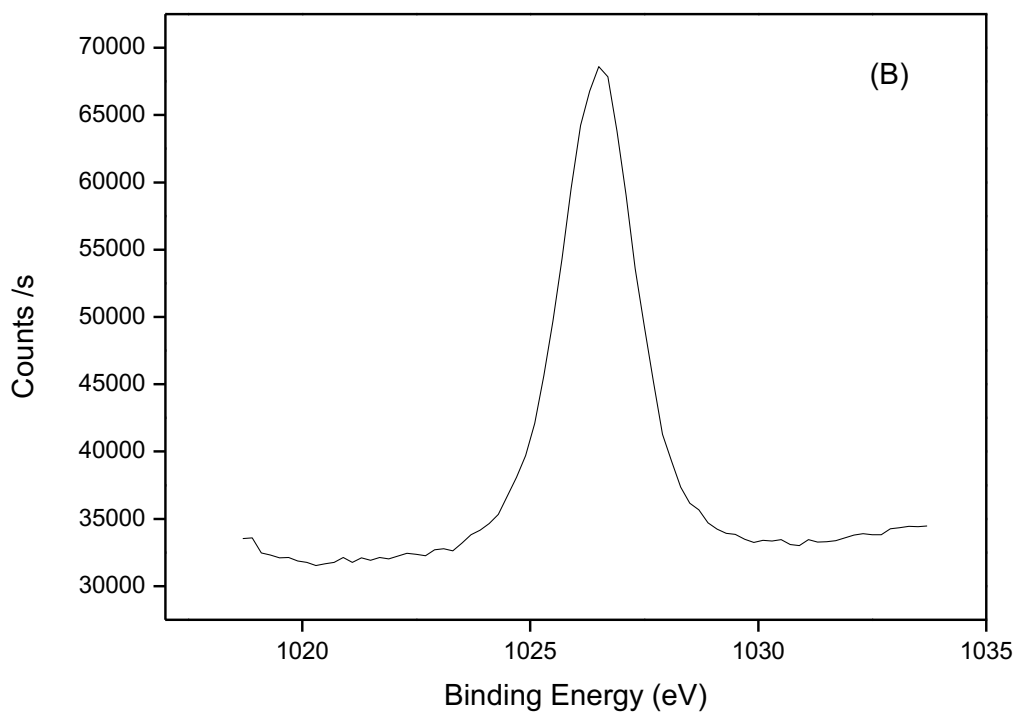
Sample Name	Zn 2p _{1/2} (eV)	Zn 2p _{3/2} (eV)	S 2p (eV)	In 3d _{5/2} (eV)	In 3d _{3/2} (eV)
ZnS	1045.1	1022.1	161.9	-----	----
0.2% In ZnS	1046.9	1024.1	164.7	-----	----
0.4% In ZnS	1048.9	1025.7	165.4	-----	----
0.8% In ZnS	1048.5	1025.2	165.3	-----	----
1% In ZnS	1048.8	1025.5	165.8	448.6	455.7
2% In ZnS	1049.3	1026.3	166.1	449.2	456.2

Table 4.3 shows that as the amount of indium in the sample increases there is a shift in binding energies of the zinc and sulfur peaks to higher energies suggesting that the incorporation of indium in the ZnS crystal is causing distortions as also seen in the photoluminescence emission spectra. These distortions were not observed in the XRD pattern due to the low sensitivity of that technique were dopant peaks below 5% are generally not observed.

The peaks for indium do not appear until the 1% doping level and even at the 2% doping level the peaks are not very strong. The binding energies of the peaks are

consistent with the energies for indium 3+ ions with peaks at ~ 448 eV and ~ 454 eV corresponding to the In $3d_{5/2}$ and In $3d_{3/2}$ electrons respectively.





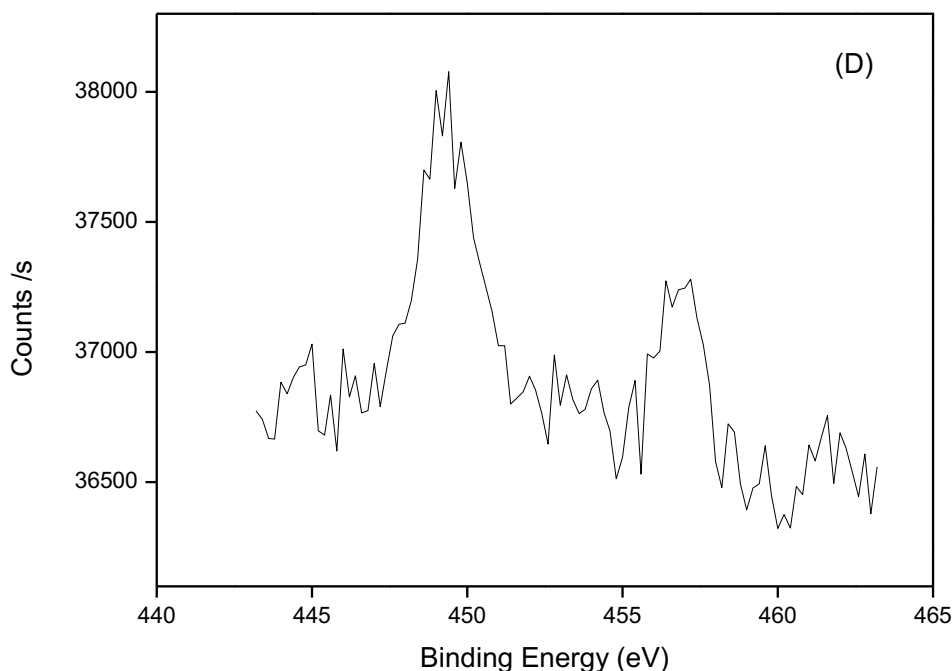


Fig 4.8. XPS spectra for 2 % In – ZnS (A) Zn $2p_{1/2}$ peak (B) Zn $2p_{3/2}$ peak (C) S $2p$ peak and (D) In $3d$ peaks.

For all spectra, the reference peak of C1s remained at the reference binding energy of C – C bonding at 284.8 eV. This indicates the shifting to higher binding energies for all peaks with an increasing amounts of indium in the sample is a chemical effect rather than as a result of charging. The binding energy peak position depends on the oxidation state and the local chemical environment of the element. With the introduction of In^{3+} into the crystal structure, there are changes to the environment around the Zn^{2+} and S^{2-} ions. Indium is a more electronegative element than zinc and a more electronegative dopant can lead to an increase in the binding energy of the base element (zinc) as the electron density around zinc decreases, requiring more energy to remove an electron. For sulphur the ratio of binding changes with the introduction of In^{3+} due to the difference in the oxidation states between zinc and indium.

4.3.6 Photocatalytic Activity

The photocatalytic activity of the group 13 metal ZnS samples was measured by following the degradation of the dye methylene blue under irradiation from a 60 W incandescent light bulb in the presence of the powdered photocatalyst.

Table 4.4. Photocatalytic degradation rate of methylene blue under irradiation from a 60 W light bulb in the presence of the photocatalysts

Sample	Photocatalytic Degradation Rate (min⁻¹)	Correlation Co-efficient (R² value)
ZnS	0.0048	0.97808
0.2% Al ZnS	0.0045	0.94582
0.4% Al ZnS	0.0072	0.96378
0.8% Al ZnS	0.0035	0.89829
1% Al ZnS	0.0047	0.98264
2% Al ZnS	0.0040	0.9132
0.2% Ga ZnS	0.0043	0.92773
0.4% Ga ZnS	0.0065	0.93828
0.8% Ga ZnS	0.0030	0.95258
1% Ga ZnS	0.0050	0.96093
2% Ga ZnS	0.0026	0.97258
0.2% In ZnS	0.0046	0.9996
0.4% In ZnS	0.0075	0.9854
0.8% In ZnS	0.0058	0.99211
1% In ZnS	0.0042	0.97796
2% In ZnS	0.0046	0.99003

Table 4.4 shows that optimum loading concentration for each dopant is 0.4%. Below this concentration the activity of the catalyst is the same as the bare catalyst. Above this concentration the activity drops off due to an excess of metal dopant being present. The excess metal can act as a cover on the surface of the photocatalyst reducing the number of sites available for photocatalysis to take place.

When using a metal dopant to improve the photocatalytic activity, an optimum concentration is required. The results in table 4.4 show that for the degradation of methylene blue under indoor light irradiation of the three group 13 metals studied that 0.4% is the optimum concentration when samples are prepared by microwave irradiation.

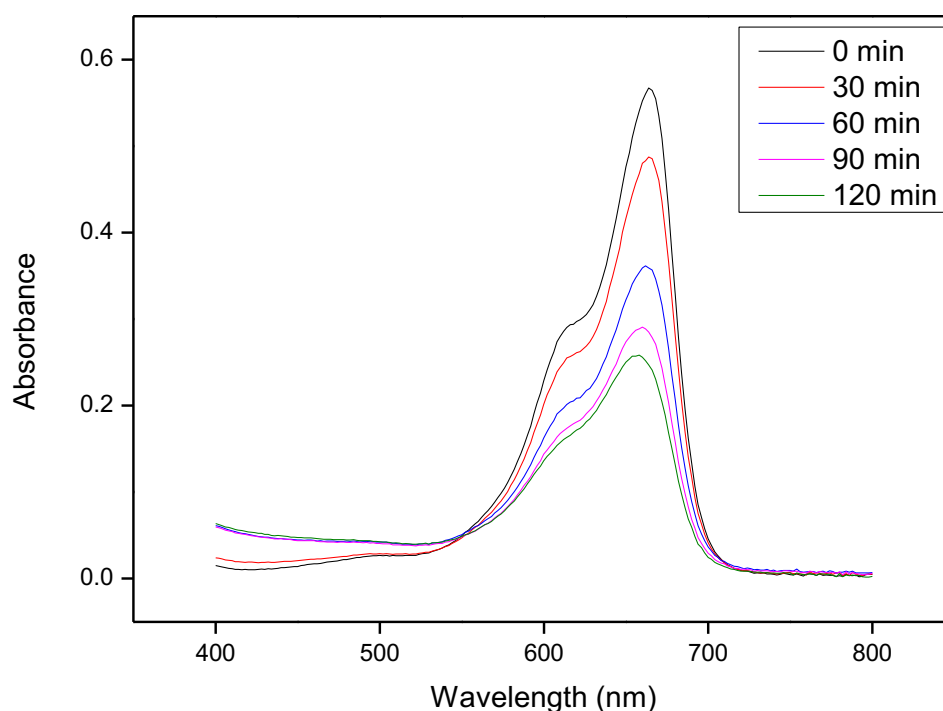


Fig 4.9. Photocatalytic degradation of methylene blue under irradiation from a 60 W bulb in the presence of 0.4% In doped ZnS

4.3.7 Anti-bacterial Study

The anti-bacterial study for the aluminium, gallium and indium doped samples was carried out using *E. coli* and *S. aureus* as the test microbes. An agar plate was prepared with the catalyst added to the agar at a concentration of 1% w/v while it was molten and a plate poured with the nano-sized catalyst dispersed throughout the agar. The plates were prepared in duplicate and inoculated with the microbes. One set of plates was exposed to light from the 60 W bulb for 3 hours prior and the other set was kept in the dark for the 3 hours. After the 3 hours both sets of plates were incubated at 37 °C for 24 hours. Control agar plates with no catalyst were also prepared.

Table 4.5 Anti-bacterial activity of aluminium doped ZnS samples

Sample	Light Exposure		No Light Exposure	
	<i>E. coli</i>	<i>S. aureus</i>	<i>E. coli</i>	<i>S. aureus</i>
Blank Control	Growth	Growth	Growth	Growth
ZnS (Sigma Aldrich)	Growth	Growth	Growth	Growth
Degussa (Evonik) P25 TiO ₂	Growth	Growth	Growth	Growth
ZnS Microwave	No Growth	No Growth	No Growth	No Growth
0.2% Al – ZnS	No Growth	No Growth	No Growth	No Growth
0.4% Al – ZnS	No Growth	No Growth	No Growth	No Growth
0.8% Al - ZnS	No Growth	No Growth	No Growth	No Growth
1% Al – ZnS	No Growth	No Growth	No Growth	No Growth
2% Al - ZnS	No Growth	No Growth	No Growth	No Growth

Table 4.6 Anti-bacterial activity of gallium doped ZnS samples

Sample	Light Exposure		No Light Exposure	
	E. coli	S. aureus	E. coli	S. aureus
Blank Control	Growth	Growth	Growth	Growth
ZnS (Sigma Aldrich)	Growth	Growth	Growth	Growth
Degussa (Evonik) P25 TiO ₂	Growth	Growth	Growth	Growth
ZnS (Microwave)	No Growth	No Growth	No Growth	No Growth
0.2% Ga – ZnS	No Growth	No Growth	No Growth	No Growth
0.4% Ga – ZnS	No Growth	No Growth	No Growth	No Growth
0.8% Ga - ZnS	No Growth	No Growth	No Growth	No Growth
1% Ga – ZnS	No Growth	No Growth	No Growth	No Growth
2% Ga - ZnS	No Growth	No Growth	No Growth	No Growth

Table 4.7 Anti-bacterial activity of indium doped ZnS samples

Sample	Light Exposure		No Light Exposure	
	E. coli	S. aureus	E. coli	S. aureus
Blank Control	Growth	Growth	Growth	Growth
ZnS (Sigma Aldrich)	Growth	Growth	Growth	Growth
Degussa (Evonik) P25 TiO ₂	Growth	Growth	Growth	Growth
ZnS (Microwave)	No Growth	No Growth	No Growth	No Growth
0.2% In – ZnS	No Growth	No Growth	No Growth	No Growth
0.4% In – ZnS	No Growth	No Growth	No Growth	No Growth
0.8% In - ZnS	No Growth	No Growth	No Growth	No Growth
1% In – ZnS	No Growth	No Growth	No Growth	No Growth
2% In - ZnS	No Growth	No Growth	No Growth	No Growth

As demonstrated in Chapter 3, the microwave prepared zinc sulfide samples showed a bacteriostatic effect towards *E. coli* and *S. Aureus*, both when irradiated with light and when not.

4.4 Temperature Study

The effect of temperature on the physical properties, optical properties, crystal structure and photocatalytic activity was carried out. Samples were calcined in a furnace in air at various temperatures up to 600 °C for 2 hours covered in a crucible.

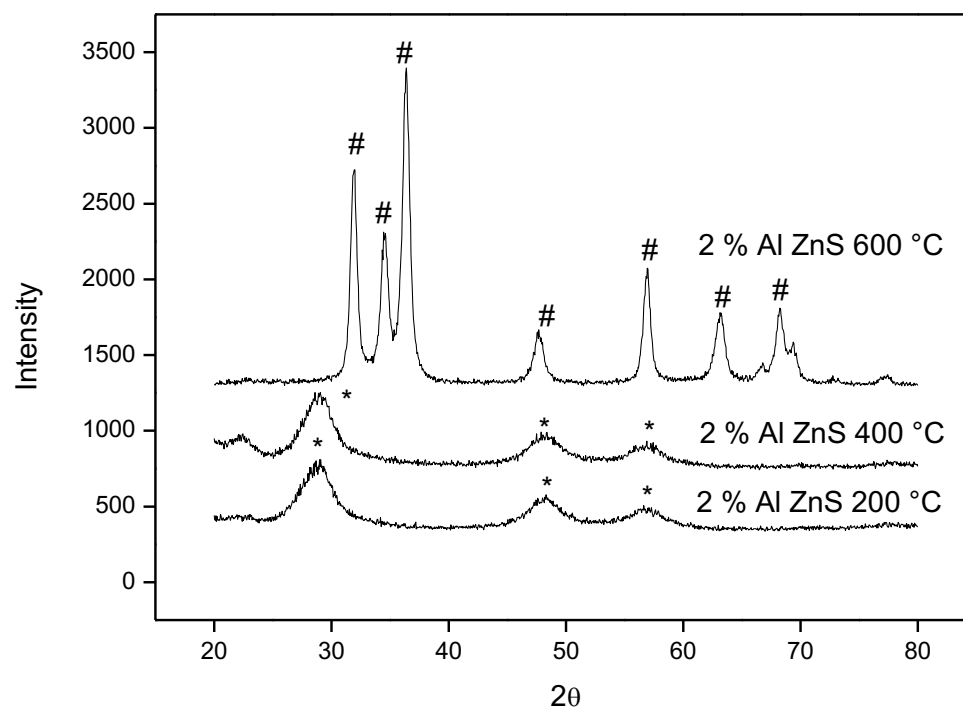


Fig 4.10. X-ray diffraction patterns of 2 % Al – ZnS calcined at 200, 400 and 600 °C for 2 h (# = ZnO wurtzite peak, * = ZnS sphalerite peak)

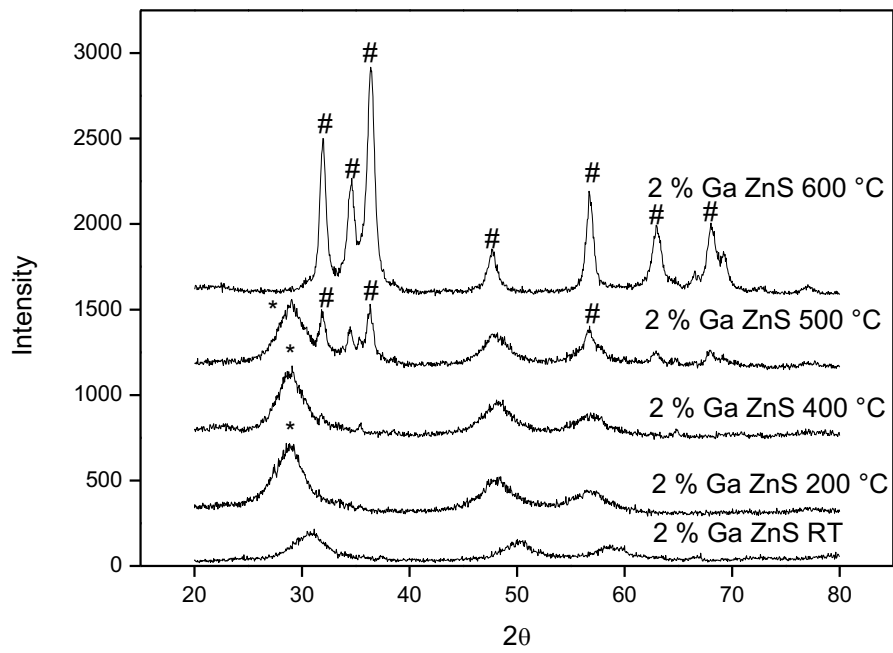


Fig 4.11. X-ray diffraction patterns of 2 % Ga – ZnS prepared at room temperature and calcined at 200, 400, 500 and 600 °C for 2 h (# = ZnO wurtzite peak, * = ZnS sphalerite peak)

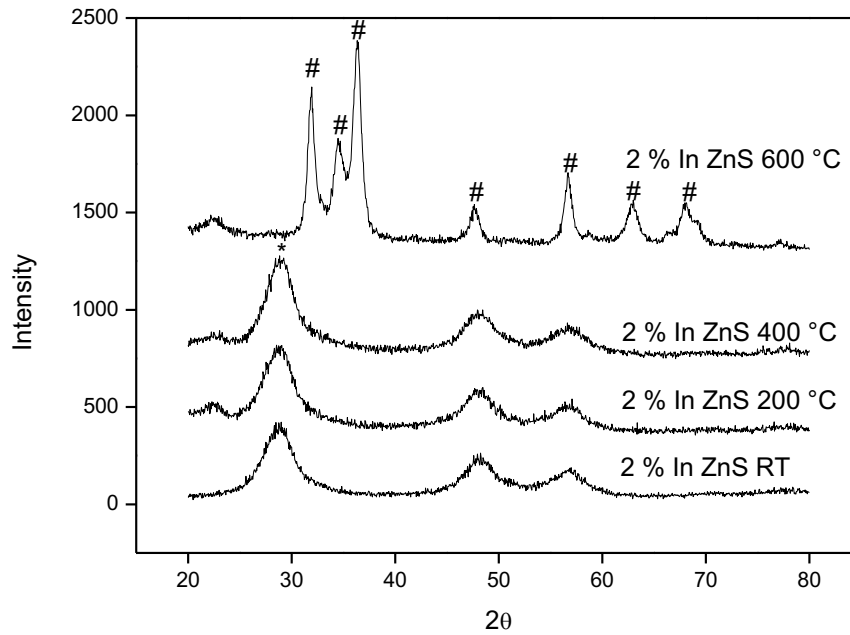


Fig 4.12. X-ray diffraction patterns of 2% In – ZnS prepared at room temperature and calcined at 200, 400 and 600 °C for 2 h (# = ZnO wurtzite peak, * = ZnS sphalerite peak)

The x-ray diffraction investigation of the calcined Al-, Ga- and In – ZnS samples follow a similar pattern indicating the metal has no effect on the calcination of the semiconductor. In each sample, up to 400 °C the only crystal phase present was cubic blende zinc sulfide. At 500 °C, in the Ga – ZnS samples (figure 4.11) there was a mix of cubic blende zinc sulfide and wurtzite zinc oxide present. The transformation to zinc oxide occurs due to oxidation of ZnS at a temperature above 400 °C. At 600 °C, there are no peaks observed in any of the doped ZnS samples for ZnS, with complete transformation to wurtzite phase zinc oxide occurring.

The diffuse absorbance spectra of the samples calcined at 200 °C and 400 °C are also very similar to that of the uncalcined samples with no change in the apparent band gaps of the samples or an increase in the absorption shoulders into the visible light region.

Table 4.8 Photocatalytic rates of group 13 metal doped ZnS samples pre-calcined at room temperature, 200 °C, 400 °C and 600 °C.

Sample	Photocatalytic Degradation Rate (min⁻¹) of as prepared samples	Photocatalytic Degradation Rate (min⁻¹) of samples calcined at 200 °C	Photocatalytic Degradation Rate (min⁻¹) of samples calcined at 400 °C	Photocatalytic Degradation Rate (min⁻¹) of samples calcined at 600 °C
ZnS	0.0048	0.0096	0.0113	0.0000
0.2% Al ZnS	0.0045	0.0085	0.0083	0.0000
0.4% Al ZnS	0.0072	0.0096	0.0090	0.0000
0.8% Al ZnS	0.0035	0.0094	0.0087	0.0000
1% Al ZnS	0.0047	0.0087	0.0080	0.0000
2% Al ZnS	0.0040	0.0074	0.0071	0.0000
0.2% Ga ZnS	0.0043	0.0075	0.0072	0.0000
0.4% Ga ZnS	0.0065	0.0089	0.0098	0.0000
0.8% Ga ZnS	0.0030	0.0085	0.0111	0.0000
1% Ga ZnS	0.0050	0.0089	0.0077	0.0000
2% Ga ZnS	0.0026	0.0065	0.0063	0.0000
0.2% In ZnS	0.0046	0.0092	0.0058	0.0000
0.4% In ZnS	0.0075	0.0089	0.0087	0.0000
0.8% In ZnS	0.0058	0.0093	0.0065	0.0000

ZnS				
1% In ZnS	0.0042	0.0110	0.0060	0.0000
2% In ZnS	0.0046	0.0123	0.0054	0.0000

Photocatalytic testing was carried out in the calcined samples in the same manner as the room temperature prepared samples with methylene blue used the model pollutant. It is shown in table 4.8 that there is an increase in the photocatalytic activity of all samples calcined at 200 °C, the same increase in the Al- and Ga – ZnS samples at 400 °C but a reversion to the room temperature photocatalytic rates in the In – ZnS samples. At 600 °C, all samples including the undoped ZnS sample are fully converted to wurtzite phase zinc oxide, which shows no photocatalytic activity under irradiation from the 60 W bulb.

The rises in photocatalytic activity of samples calcined at 200 °C can be explained by increased crystallinity due to calcination. Although there is no crystal growth in the samples, any amorphous powder left after the 30 minutes microwave irradiation will be converted to crystalline ZnS and the increased amount of crystalline powder present in the samples leads to higher photocatalytic activity. At 400 °C, the photocatalytic activity is maintained for the aluminium and gallium samples but the indium doped samples photocatalytic activity is similar to the room temperature samples. The reason for this is thought to be due to the difference in incorporation of the aluminium, gallium and indium ions into the ZnS samples. As the aluminium and gallium ions are smaller than the zinc ions, these ions can be doped into the interstitial sites in the ZnS crystal.^{145,159} As the indium ions are larger than the zinc ions, the indium doping occurs as substitution of the Zn²⁺ ions. As the temperature increases there is likely an increase in the amount of In₂S₃ present in the ZnS, even though it is below the limit of detection

of the XRD, and this will reduce the amount of sites on the ZnS crystal available for photocatalysis.¹⁶¹

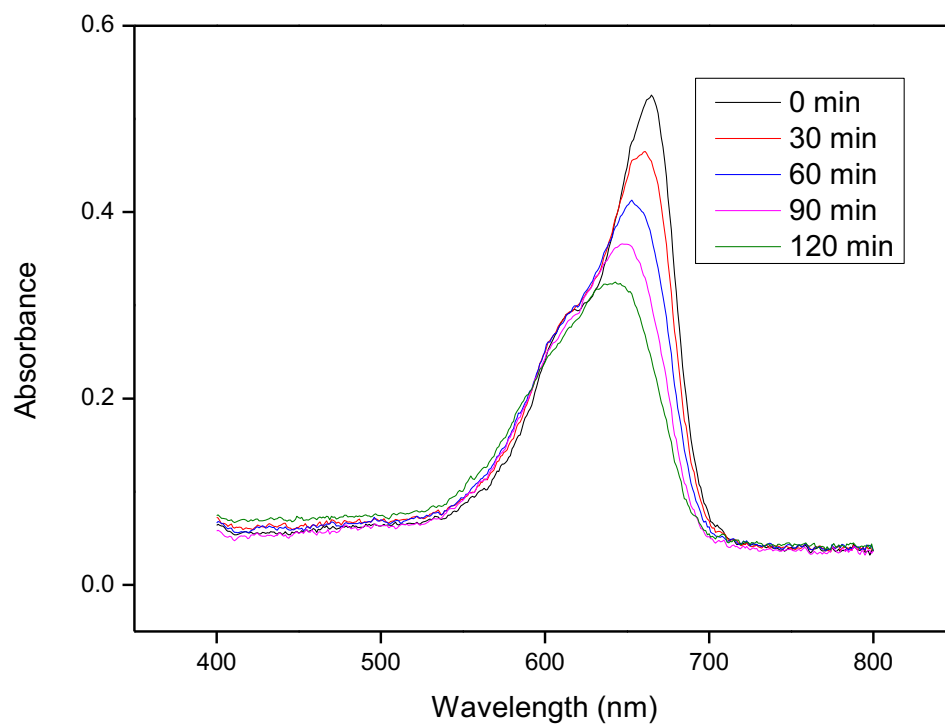


Fig 4.13. Photocatalytic degradation of methylene blue under irradiation from a 60 W light bulb in the presence of 0.8% In ZnS calcined at 400 °C

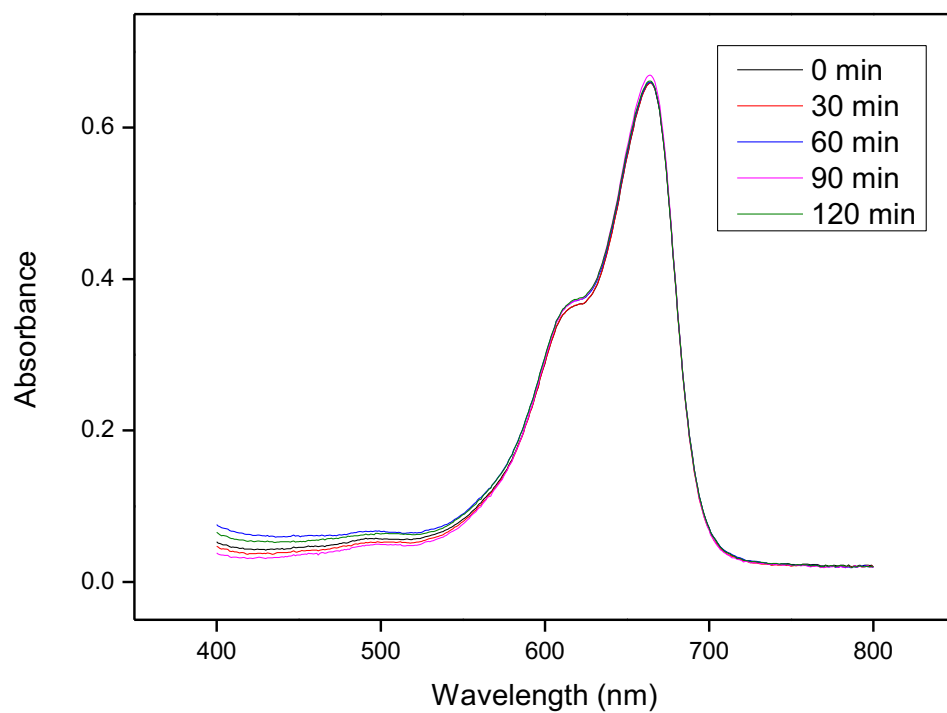


Fig 4.14. Photocatalytic degradation of methylene blue under irradiation from a 60 W light bulb in the presence of 0.4% Ga ZnS calcined at 600 °C

4.5 Conclusions

ZnS doped with aluminium, gallium and indium were successfully prepared using a microwave assisted irradiation technique. The samples prepared all had a particle size of around 4 nm and showed via the x-ray diffraction pattern to be a cubic blende zinc sulfide crystal phase.

The aluminium and gallium doped samples showed no change to the optical properties of the undoped zinc sulfide sample, however the indium doping caused an shoulder to appear in the absorbance spectra which extended into the visible light region and a reduction in the measurable band gap of the indium doped samples. Photoluminescence studies showed that there was no change in the emission spectra of the aluminium or gallium doped samples compared to the undoped ZnS samples but that there was a reduction in the emission intensity with increasing amounts of indium in the samples.

Photocatalytic degradation studies on methylene blue under irradiation from indoor light showed an increase in the photocatalytic activity of the doped samples with 0.4 % found to be the optimum concentration.

Anti-bacterial studies were carried out on the metal doped samples and they were found to have a bacteriostatic effect, inhibiting the growth of CFU's of both *E. coli* and *S. aureus* compared to control semiconductor photocatalyst, TiO₂ and sigma-aldrich ZnS. The bacteriostatic effect was also present when the bacteria were grown in dark conditions due to the material being toxic to the bacterium.

Temperature studies show that all samples are converted to zinc oxide when calcined at 600 °C for 2 h. When calcined at 200 °C and 400 °C, the samples remain as ZnS and improved photocatalytic activity is observed due to an increased crystallinity in the samples.

Chapter 5: Silver and Indium co-doped ZnS

5.1 Introduction

In this chapter, the effect of varying silver concentrations added to 0.4% In – ZnS was investigated. Work from this group has already shown that doping photocatalysts, such as TiO₂¹⁶² and ZnO,¹⁶³ with silver leads to an increase in the photocatalytic ability. It is generally considered that silver acts as an electron capture site on the surface of the photocatalyst and this can reduce the recombination rate of the electron hole pair.^{164,165,166,167}

Silver was chosen as a modifier for ZnS to improve the anti-microbial activity. Silver has been used for centuries as an anti-microbial agent. The Phoenicians used to store water in silver bottles to keep it clean,¹⁶⁸ silver dollars were added to milk bottles to prevent them from spoiling and fresh water was kept in ‘silvered’ containers on ships for long voyages. In 1884, the practice of adding drops of aqueous silver nitrate to newborn children’s eyes to prevent transmission of *N. gonorrhoeae* during childbirth.¹⁶⁹ During the following years, the antibacterial effectiveness of various metals has been studied and silver has been shown to be the most effective while being the least toxic toward animal cells.¹⁷⁰

The discovery and use of anti-biotics in the 1940’s led to a reduction in the use and investigation of silver for its antibacterial properties but since the rise of anti-biotic resistance strains of bacteria, research has begun to refocus on alternative technologies including silver and silver based systems such as intravenous devices like silver coated cardiac devices, catheters and surgical tools.¹⁷¹

ZnS exists in two structural polymorphs, cubic blende sphalerite and hexagonal wurtzite. Of the two polymorphs, the cubic blende is considered as the stable phase at standard temperature and pressure. Cubic blende ZnS has a face centered cubic structure in which both the zinc and sulfur atoms are tetrahedrally coordinated. Wurtzite phase

ZnS is more thermodynamically stable at temperatures above 1020 °C, but can exist as a metastable phase at standard temperature and pressure. The wurtzite phase has a hexagonal close packed structure in which the Zn and S atoms are also tetrahedrally coordinated. In nanosized materials, many factors can change the phase transition temperature, including the small size, increased pressure, surface modification, and precipitation rates during the synthesis of the semiconductor.

A low temperature preparation of hexagonal ZnS is desirable because the prepared wurtzite nanostructures can meet thermal stability required for reliable optoelectronic device operation, including the incorporation of these materials in flexible substrates such as plastics. The hexagonal structure is often cited as the more desirable structure for its optical properties than the cubic blende structure.^{54,172,173} It has been shown based on surface energy measurements that nanoparticles of wurtzite phase ZnS is more thermodynamically stable than nanoparticles of sphalerite ZnS.¹⁷⁴ Phosphors of ZnS are synthesised in the wurtzite phase to optimise the luminescence at temperatures of 1000 °C or more. Mixed phased systems are also desirable as in the case of electroluminescent materials.⁵³

In this chapter, the preparation and characterisation of silver and indium co-doped ZnS and the effect of these dopants on the photocatalytic activity and antibacterial action is discussed. The phase change from the cubic blende phase to hexagonal wurtzite phase with increasing amounts of silver is also presented. The results of this chapter were published in the journal *Nanotechnology* as ‘Novel microwave assisted synthesis of ZnS nanomaterials’ – D. W. Synnott, M. K. Seery, S. J. Hinder, J. Colreavy and S. C. Pillai, *Nanotechnology* **24** (2013) 045704

5.2 Characterisation

Silver and indium co-doped ZnS samples were prepared by microwave synthesis at an irradiation power of 600 W and an irradiation time of 30 minutes. As shown in chapter 4, an indium doping level of 0.4% was the optimum level for improving the photocatalytic activity of the ZnS sample. For the silver indium co-doping study, the level of indium was kept at 0.4% across all samples while the level of silver was varied from 0.4% to 8%. Samples were prepared in an open beaker by adding 200 mL of aqueous zinc acetate dihydrate and 200 mL of aqueous thiourea solution together. To this 4 mL of 0.04 M indium acetate and varying amount of 0.04 M silver nitrate solution were added. As the amount of silver nitrate was increased the solution turned from clear to slightly brown in colour. The solution were mixed and exposed to the microwave irradiation. After the 30 minutes irradiation time and the 5 minute cool down period had elapsed, a dry powder was collected and used without further treatment. The powders had a yellow colour which changed to a deep brown as increasing amounts of silver were added to the samples.

5.2.1 X-ray Diffraction

The crystal structure of the as-prepared samples was investigated by X-ray diffraction. Figure 5.1 shows that the zinc sulfide samples and samples prepared with up to 2 % silver doping are cubic blende form of ZnS with peaks at 28.55 °, 47.55 ° and 56.3 ° corresponding to the (111), (200) and (220) planes respectively. When the mol % of silver is increased to 4 % and 8 % the peaks at 27.15 °, 28.75 °, 30.7 °, 47.7 °, 51.75 ° and 56.45 ° are observed which correspond to the (100), (002), (101), (102), (110), (103) and (112) planes respectively, and indicate that the wurtzite hexagonal phase of ZnS is present.

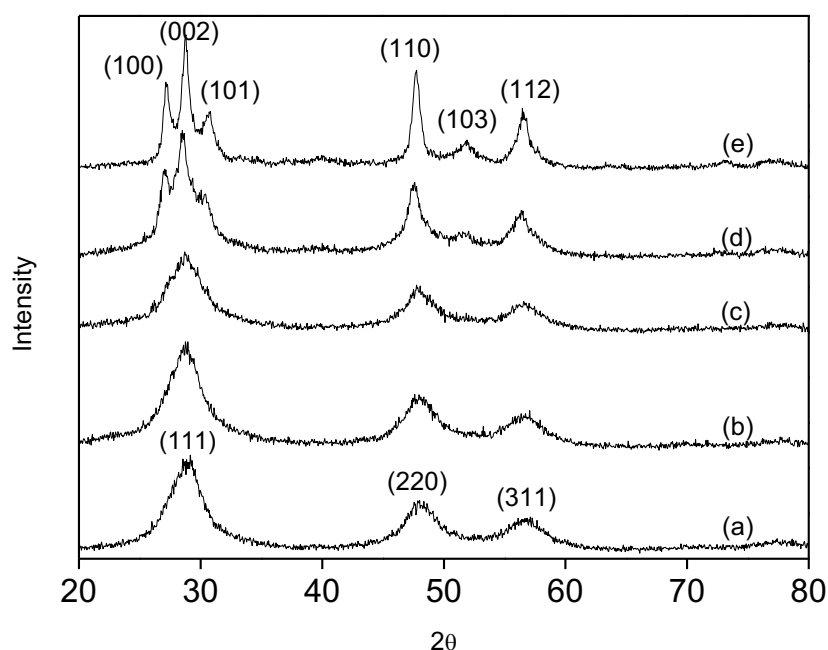


Fig 5.1. X-ray diffraction patterns of (a) ZnS (b) 1% Ag – ZnS (c) 2% Ag – ZnS (d) 4% Ag – ZnS and (e) 8% Ag – ZnS

In the XRD patterns no peaks showing the presence of AgS or AgInS₂ are observed, which suggest that the silver and indium ions are added into the lattice or on the surface of the ZnS crystal and the solid solution of (AgIn)_xZn_{2(1-x)} is not formed.¹⁷⁵ The particle

size of the samples is estimated from the X-ray diffraction patterns using the Scherrer equation,¹⁷⁶ by measuring the line broadening of the (111) peak in the cubic blende ZnS and the (002) peak in the wurtzite ZnS. For samples up to 4 mol % silver the particle size is estimated to be $4 \text{ nm} \pm 1$ and at 8 mol % silver the particle size increases to 8 nm. The broadening of the peaks suggests that the particles are nanosized and the small particles sizes are consistent with literature reports of ZnS prepared via microwave synthesis.¹⁷⁷

5.2.2 X-ray Photoelectron Spectroscopy

X-ray photoelectron spectroscopy (XPS) was carried out on the silver and indium co-doped samples at the University of Surrey by Dr. Steven Hinder. XPS was employed to characterise the ionic phase of the silver and indium dopants on the surface and to look for changes in the zinc and sulfur spectra relative to the undoped samples. No peak was detected for indium in any of the samples due to the level of doping being below the detection limit of the instrument. Silver below 2% could also not be detected. In all samples at 2 % silver and above, peaks for silver were detected at $368.7 \pm 0.2 \text{ eV}$ and $374.6 \pm 0.3 \text{ eV}$. Figure 5.4 shows the Ag-3d peaks for 4 % Ag – 0.4 % In ZnS. These peaks are consistent with those of Ag 3d peaks and the spin-orbit splitting of the 3d doublet of 5.8 eV is characteristic of metallic silver.^{178,179}

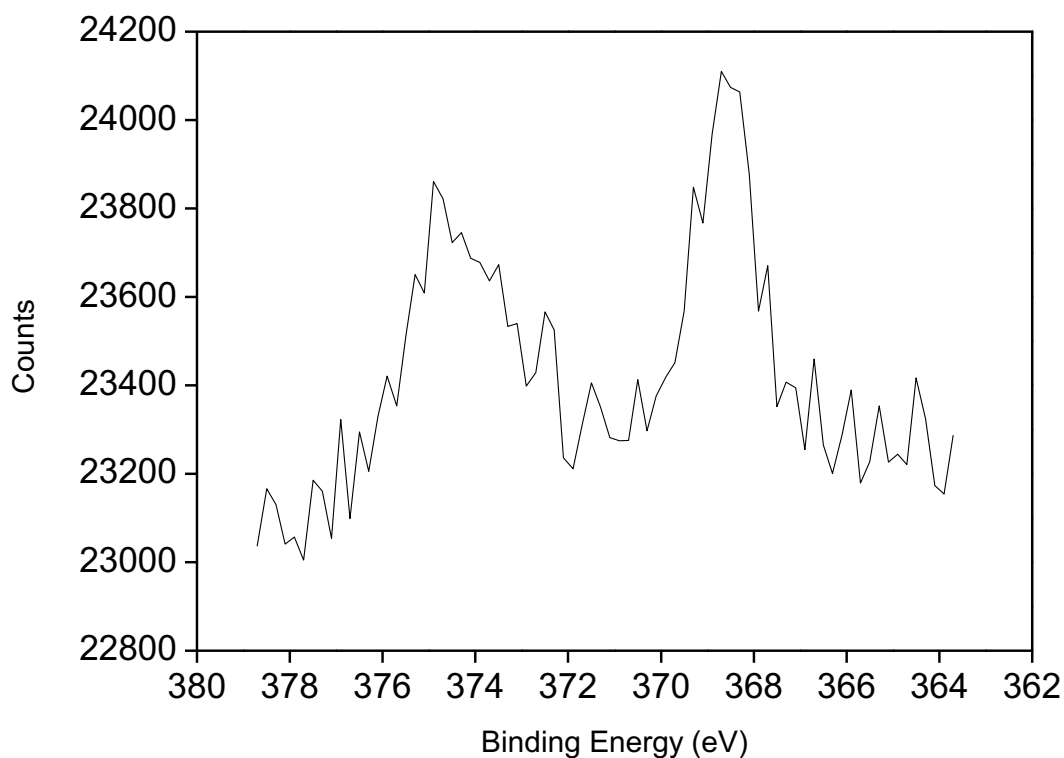


Fig 5.2. X-ray photoelectron spectrum of Ag-3d for 4% Ag – 0.4% In ZnS

Peaks for the silver and indium co-doped samples were also present at 1045.5 ± 0.2 eV, 1022.5 ± 0.2 eV and 162.5 ± 0.6 eV. These peaks correspond to the binding energy of Zn 2p_{1/2}, Zn 2p_{3/2} and S 2p_{1/2} electrons respectively and indicate the presence of ZnS without any modifications occurring due to the presence of the doping. A summary of the XPS peaks is presented in Table 5.1.

Table 5.1. X-ray photoelectron binding energies for silver and indium co-doped samples.

Sample Name	Binding Energies (eV)					
	S 2p1	Zn 2p1/2	Zn 2p3/2	In	Ag 3d5	Ag 3d5
0.4% Ag – 0.4% In ZnS	162.3	1045.3	1022.3	-	-	-
1% Ag – 0.4% In ZnS	162.4	1045.4	1022.4	-	-	-
2% Ag – 0.4% In ZnS	162.5	1045.5	1022.5	-	368.5	374.3
4% Ag – 0.4% In ZnS	161.9	1045.5	1022.5	-	368.7	374.9
8% Ag – 0.4% In ZnS	163.1	1045.7	1022.7	-	368.9	374.7

5.2.3 Scanning Electron Microscopy

Scanning electron microscopy images, figure 5.3 shows a significant difference between the samples containing 0.4% Ag and 8% Ag. In the 0.4% - 0.4% In ZnS, the agglomerates are less than 1 μm in size with regular shapes. The 8% Ag – 0.4% In ZnS sample shows much larger agglomerates, with irregular shapes.

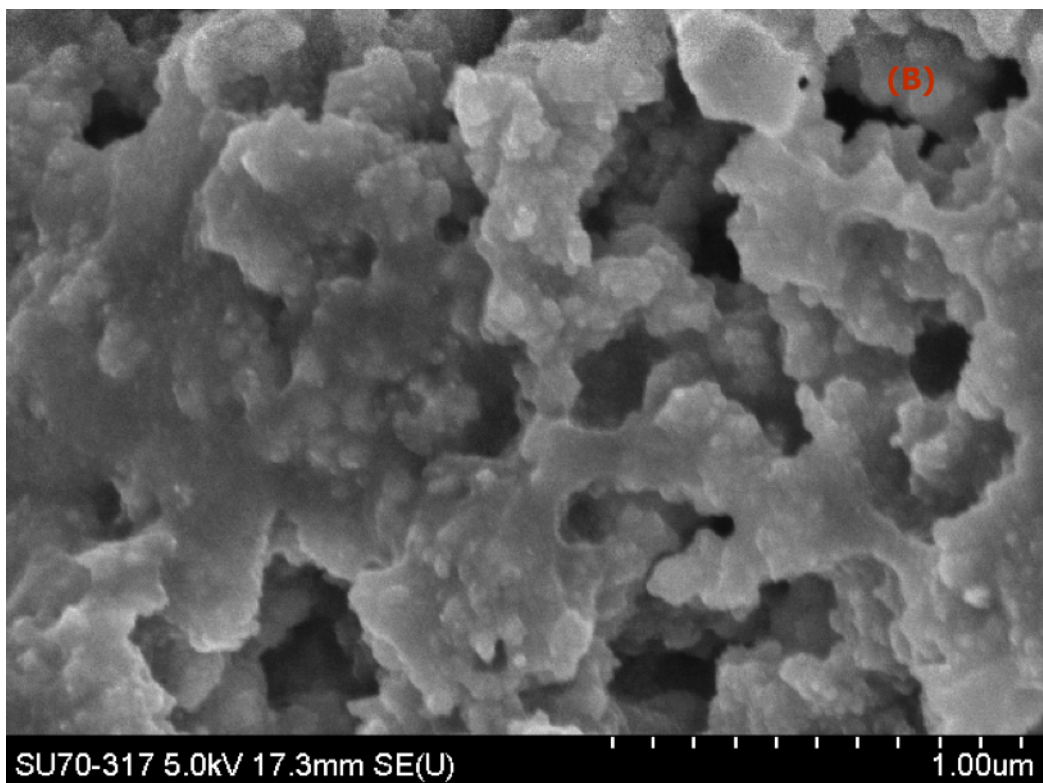
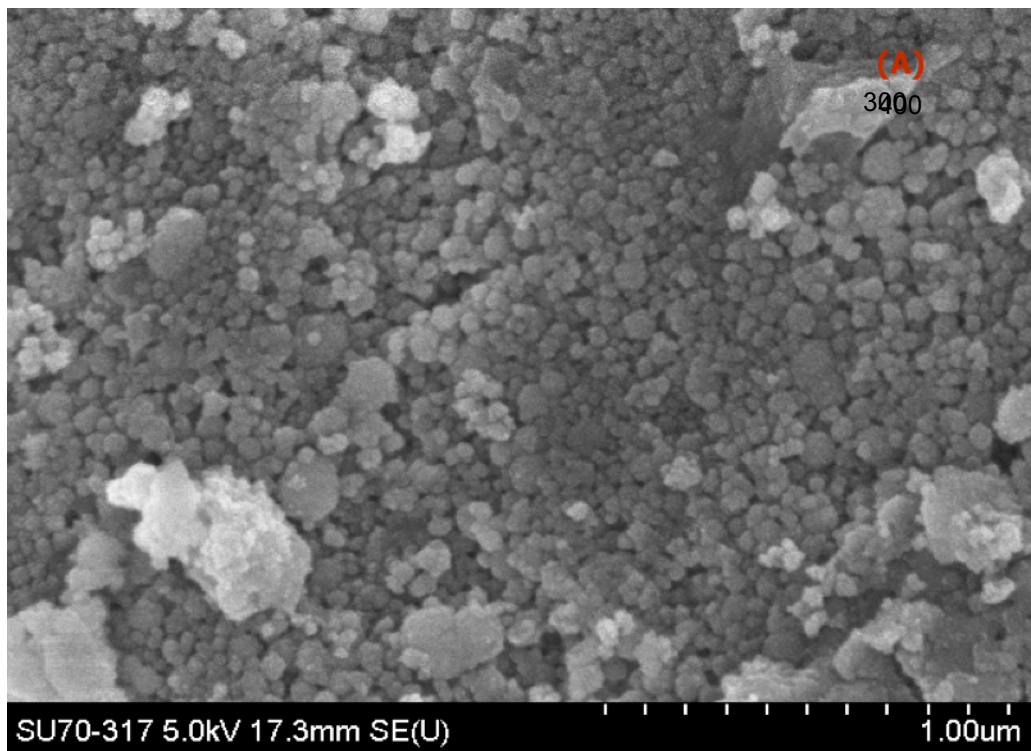


Fig 5.3. SEM images of (A) 0.4% Ag-0.4% In ZnS and (B) 8% Ag-0.4% In ZnS

5.2.4 Optical Characterisation

UV-Vis diffuse absorbance spectroscopy was used to determine the band gap of the semiconductor and to look at the characteristics of the absorption spectra of the samples. In Figure 5.4 ZnS and samples containing up to 2% silver there is an absorption edge at 319 nm, which equates to a band gap of 3.9 eV. This band gap is greater than that of bulk ZnS, 3.7 eV, due to the quantum confinement effect associated with nanometre sized particles. For the samples containing 0.4 mol % and 1 mol % silver there is a shoulder in the absorption spectra which stretches to 500 nm and up to 570 nm for the sample containing 2 mol % silver. These shoulders show that the samples absorb light in the visible region, as supported by the yellow to orange colours of these samples. The samples containing 4 and 8 mol % silver are brown coloured powders and the diffuse absorbance spectra complete absorbance up to 800 nm.

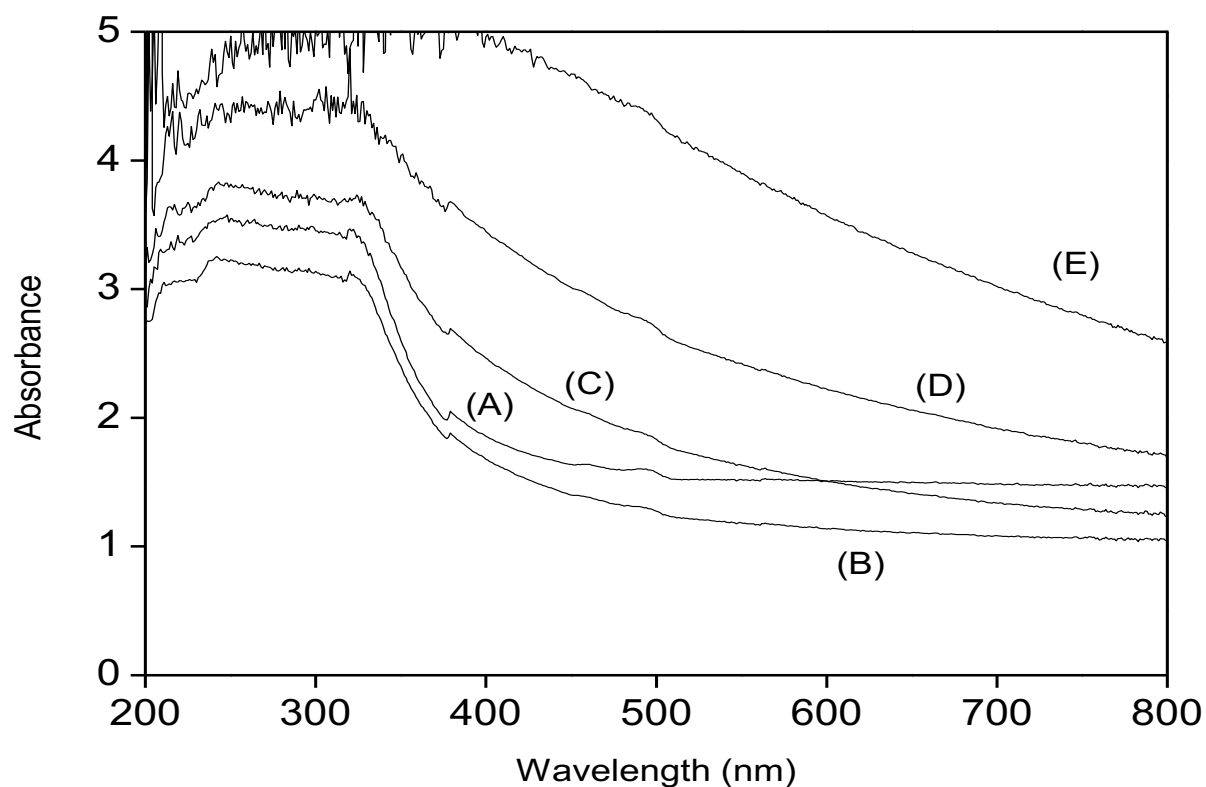


Fig 5.4. Diffuse absorbance spectra of (A) 0.4% Ag - 0.4% In ZnS, (B) 1% Ag - 0.4% In ZnS, (C) 2% Ag - 0.4% In ZnS, (D) 4% Ag - 0.4% In ZnS and (E) 8% Ag - 0.4% In ZnS

The phase transition from cubic blende to wurtzite has effects on the luminescence spectroscopy of ZnS. Figure 5.5 shows the luminescence emission spectra of 0.4% Ag - 0.4% In ZnS and that of the 8% Ag - 0.4% In ZnS. The spectra of the 0.4% Ag - 0.4% In ZnS shows emission peaks of 385, 427 and 489 nm, which correspond to three point defects within in the ZnS crystal. The peak at 385 nm is related to the interstitial zinc, the peak at 427 nm related to sulphur vacancies and the peak at 489 nm relating to zinc vacancies. Peng *et al.*⁹⁸ showed that these defect sites act as interband donor levels and reduce the energy required to promote an electron to the conduction band and leave a hole in the valence band and this induces photocatalysis. These peaks were also observed in the undoped zinc sulfide as demonstrated in figure 3.8. Conversion to hexagonal wurtzite in the 4 mol % and the 8 mol % doped ZnS causes a 10 nm redshift in the peak associated with the interstitial Zn. This shift is due to a rearrangement of the atomic structure when the phase changes from cubic blende to hexagonal wurtzite.

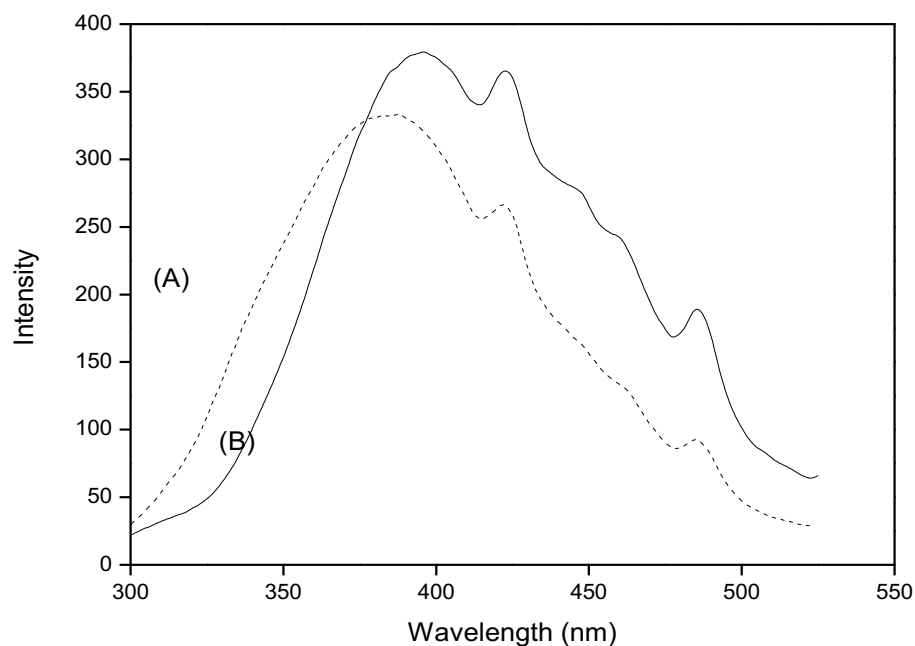


Figure 5.5. Emission spectra of (A) 0.4% Ag – 0.4% In ZnS and (B) 8% Ag – 0.4% In ZnS

Figure 5.6 shows the proposed energy levels of the ZnS with the vacancies of Zn and S providing steps for the electron to be promoted from the valence band to the conduction band by light of a lower energy than that of the band gap (3.9 eV). These extra energy levels within the band gap allow for excitation of the electron with visible light, with wavelengths up to 495 nm (2.5 eV).

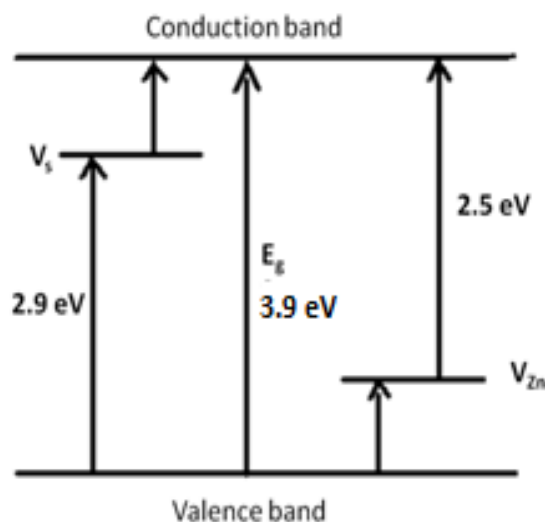


Fig 5.6. Proposed band structure of ZnS with the defects caused by zinc and sulfur vacancies acting as donor levels in the band gap

5.3 Photocatalysis Testing

Photocatalysis testing was carried out by measuring the degradation of methylene blue, a model dye, in the presence of photocatalyst under irradiation from a 60 W incandescent light bulb. The samples containing silver showed greater photocatalytic activity than the unmodified ZnS sample and Degussa P25 titanium dioxide, a commercially available photocatalyst. The results in Table 5.2 show that 2% Ag – 0.4% In ZnS had the highest photocatalytic activity while the sample containing 8 mol % silver showed no photocatalytic activity. The increase in the activity can be attributed to the role of silver as an electron scavenger.^{180,181,182} Efficient photocatalysis requires a lower recombination rate of the photo-induced electrons and holes. The holes in the valence band are primarily responsible for the formation of hydroxyl radicals, which degrade the pollutant on the surface of the photocatalyst. The optimum level of silver was found to be 2 mol %. Above this concentration the photocatalytic activity begins to

drop and at 8 mol % the photocatalytic activity is reduced completely. This is due to excess silver blocking photocatalytic sites on the surface of the photocatalyst. Indium and silver both have roles to play in the improved photocatalytic activity of the co-doped samples. Indium has two roles in improving the activity. The first is to provide n type doping by inserting a band in the semiconductor close to the valence band. This allows electrons to be promoted to the conduction band from the indium at lower wavelengths than is required for the promotion of an electron from the valence band to the conduction band. The second mechanism for indium is to increase the number of defects in the crystal. Indium incorporation into the ZnS crystal lattice can lead to an increase in faults and in lattice distortion. This is due to the difference in ionic radii of the trivalent indium ions (0.80 Å) and the bivalent zinc ion (0.74 Å).¹⁸³ The difference in the valence of the Zn^{2+} and In^{3+} also leads to an increase in the number of sulfur vacancies, which themselves act as stepping stones for the electrons travelling from the conduction band to the valence band. The role of silver on the photocatalytic activity affects the surface of the ZnS particle. Silver particles have been shown to act as electron traps,^{184,185,186,187} and this effect reduces the recombination rate of the electron-hole pair.

Table 5.2 Photocatalytic rates of microwave prepared ZnS and standard samples

Sample Name	Photocatalytic Rate (min⁻¹, x 10⁻³)
Degussa P25 TiO ₂	2.9
ZnS	5.0
0.4% Ag – 0.4% In ZnS	5.0
1% Ag – 0.4% In ZnS	6.5
2% Ag – 0.4% In ZnS	8.3
4% Ag – 0.4% In ZnS	6.1
8% Ag – 0.4% In ZnS	1.2

5.4 Role of Silver in Phase Change

The role of silver is significant in the phase change of ZnS from cubic blende to hexagonal wurtzite. It is known that the phase transition temperature can be reduced when the particles are nanosized and that the addition of additional elements also affects the transition temperature.¹⁸² In order to understand the phase change of ZnS, the Ag-In-ZnS prepared under microwave conditions were annealed at various temperatures in a chamber furnace. When the cubic blende phase 2% Ag – 0.4% In ZnS prepared by microwave was heated, for 2 hours, at temperatures up to 600 °C, no phase transition to hexagonal ZnS occurs. At 200 and 400 °C the ZnS remained in the cubic blende phase. At 500 °C, there was a mix of cubic blende zinc sulfide and zinc oxide. The ZnO formed as oxidation occurred at higher temperatures. At 600 °C, the ZnS had completely transformed to ZnO. The XRD patterns for these samples are shown in Figure 5.7.

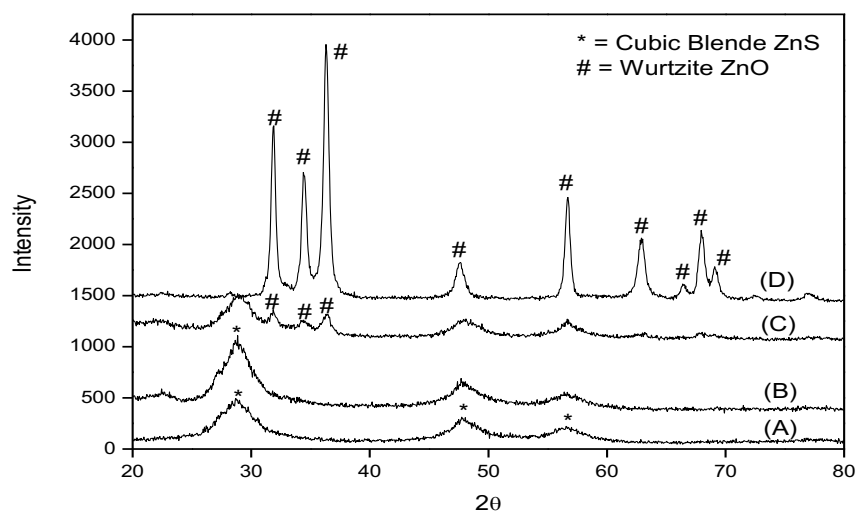


Fig. 5.7. XRD spectra of (A) 2% Ag-0.4% In ZnS, (B) 2% Ag-0.4% In ZnS calcined at 400 °C, (C) 2% Ag - 0.4% In ZnS calcined at 500 °C and (D) 2% Ag – 0.4% In ZnS calcined at 600 °C

It is therefore postulated, that silver is the key to the phase transition from cubic blende to hexagonal. A study on silver doped ZnS without indium present was carried out to add further evidence to this. It was found that the patterns match those of the silver and indium co-doped material in that when levels of silver at 4 mol % and above are used that hexagonal wurtzite is formed. Below this level cubic blende ZnS is formed. It is believed that during the microwave irradiation, metallic silver is formed as evidenced by the XPS data and the silver particles act on the surface of the crystal and affect the surface energy, lowering it to produce wurtzite phase particles as opposed cubic blende phase particles.

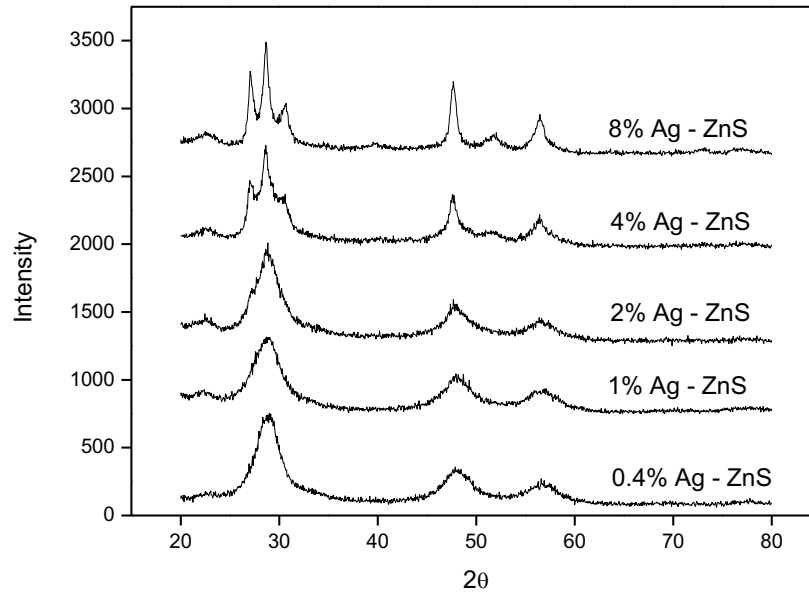


Fig 5.8. X-ray diffraction patterns of ZnS samples doped with silver at varied amounts

5.5. Anti-bacterial Activity

The ZnS samples prepared by microwave were shown to be both bacteriocidal and bacteriostatic in Chapter 3. Anti-bacterial tests were carried out on the silver and indium co-doped samples to show this characteristic was retained. Testing was carried out as described in Section 2.6.1, the agar plate method. All samples were shown to be antibacterial toward both *E. coli* and *S. aureus* as shown in Table 5.3.

Table 5.3 Anti-bacterial testing results for silver and indium codoped ZnS and controls

Sample Name	<i>E. coli</i>		<i>S. aureus</i>	
	Light	Dark	Light	Dark
Degussa P25 TiO ₂	Growth	Growth	Growth	Growth
ZnS (Sigma Aldrich)	Growth	Growth	Growth	Growth
ZnS (microwave)	No growth	No growth	No growth	No growth
0.4% Ag – 0.4% In ZnS	No growth	No growth	No growth	No growth
1% Ag – 0.4% In ZnS	No growth	No growth	No growth	No growth
2% Ag – 0.4% In ZnS	No growth	No growth	No growth	No growth
4% Ag – 0.4% In ZnS	No growth	No growth	No growth	No growth
8% Ag – 0.4% In ZnS	No growth	No growth	No growth	No growth

The effectiveness of the antimicrobial activity of the microwave synthesised ZnS is not enhanced due to the addition of indium and silver co-doping, however the ability to retain antibacterial activity while changing other properties is very important. This allows for the preparation of ZnS materials with varying optical properties to be produced for a wide range of optoelectronic and sensing devices which would remain sterile allowing for this material to be used in personal wearable devices and also medical devices which are inserted inside the body.

5.6 Conclusions

ZnS co-doped with silver and indium was studied using X-ray diffraction, X-ray photoelectron spectroscopy, Raman spectroscopy and optically using UV-Vis diffuse absorbance and luminescence. The indium concentration was kept constant at the optimum level, while the concentration of silver was varied from 0.4 mol % to 8 mol %. It was found from X-ray photoelectron spectroscopy that silver formed as metallic silver on the surface of the nanoparticles and that at concentrations above 4 mol % that this caused wurtzite ZnS to be formed. It was postulated that the silver particles reduce the surface energy of the crystals as they are forming and this allows for wurtzite to form at a much lower temperature than seen in bulk ZnS, 1020 °C.

At 2% Ag – 0.4% In, the samples showed a slight improvement in the photocatalytic activity compared to indium doping alone and greatly improved activity over undoped ZnS. The improvements come from the modification of the crystal structure by trivalent indium ions leading to increased defects and from silver on the surface acting as an electron trap and reducing the recombination rate of the electron-hole pair.

The silver and indium co-doping showed no change to the antibacterial activity of ZnS and this allows for antibacterial wurtzite phase devices to be prepared at low temperature and low cost.

Chapter 6: Future Work

The main focus of this work was on the development of an ambient pressure microwave assisted synthesis method for photocatalytic semiconductors. This work focused on the preparation of zinc sulphide based materials and their applications for anti-bacterial technology.

A natural expansion of the work would be to take this methodology and apply it other semiconductors including titanium dioxide, zinc oxide and more complex materials such as the delafossite class of materials. Titanium dioxide and microwave-assisted synthesis has been well explored,^{188,189} but using the ambient pressure system developed in this thesis would be an interesting route for industrial applications. The material produced may be a mix of amorphous and crystalline TiO₂ but could have interesting effects on the formation of anatase and an impact to the anatase to rutile transition during calcination of the microwave prepared materials.¹⁹⁰

Another interesting application of the synthesis technique could be to develop a ZnO/ZnS heterojunction by changing the ratio of zinc and sulfur starting materials to encourage the formation of ZnO crystals at the same time as the formation of the ZnS crystals to form a heterojunction. Heterojunctions are formed by the coupling of two different semiconductors to encourage interparticle electron transfer, where one of semiconductos acts like a dye in dye-assisted sensitisation of semiconductors.¹⁹¹ Titanium dioxide has been used as a base semiconductor on many occasions since first proposed by Serpone *et al.*¹⁹² and prepared with CdS^{193,194}, Bi₂S₃^{193,194} and CuAlO₂.¹⁹⁵

Kim *et al.*¹⁹⁶ prepared a visible light absorbing material based on ZnO and ZnS which was called zincoxysulfide (ZnO_xS_{1-x}) through a co-precipitation method which was used

to degrade organic pollutants. While typically a heterojunction utilises a narrow band gap semiconductor such as Bi_2S_3 (1.3 eV)¹⁹⁴ to absorb visible light and cause an electron to transfer to the wide band gap semiconductor, the use of two wide band gap semiconductors in ZnS (3.8 eV) and ZnO (3.2 eV) due to the variation in the locations of the respective valence bands (+1.4 eV for ZnS and +3.0 eV for ZnO) and conduction bands (-2.3 eV for ZnS and -0.2 eV for ZnO)¹⁹¹ versus the NHE allows interparticle transitions at lower excitation energies than would be required for the wide band gap in a single semiconductor.

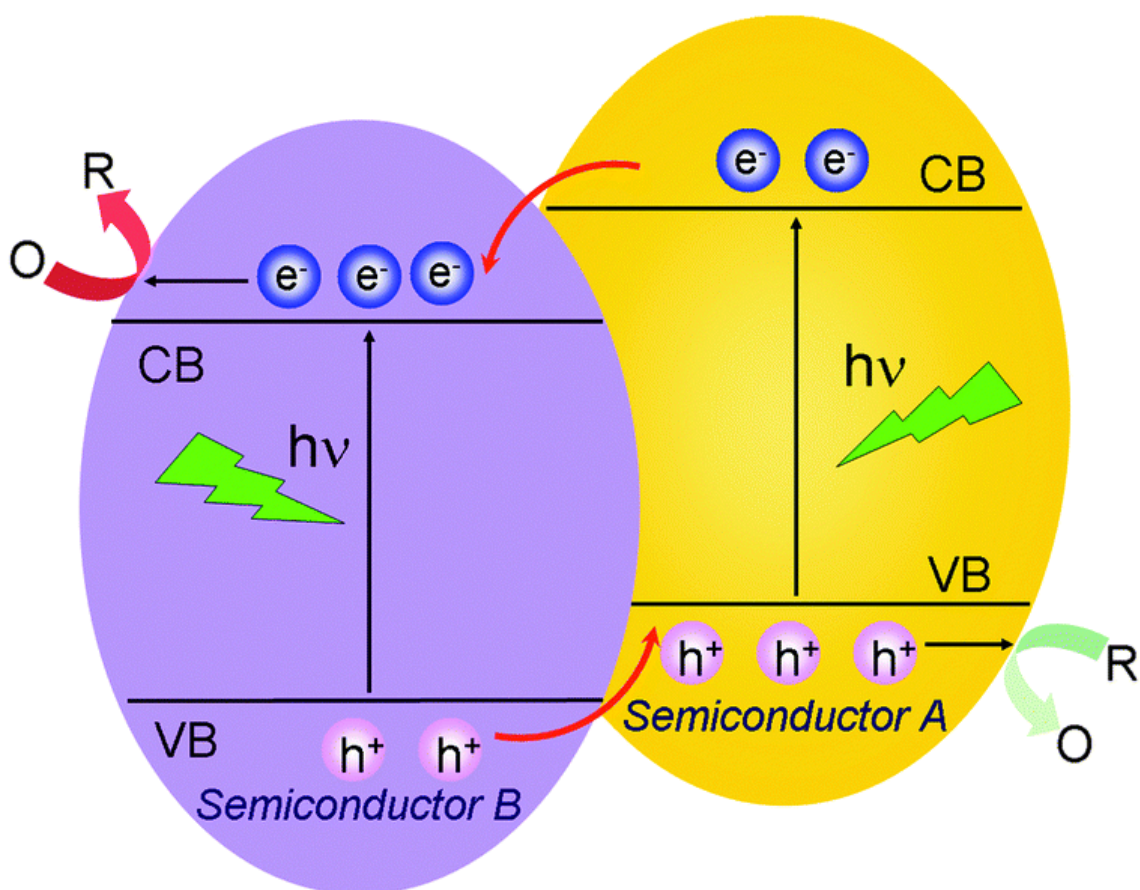


Fig 6.1 General view of a semiconductor-semiconductor heterojunction¹⁹⁷

Initial work carried out as part of this project into the creation of a heterojunction between a wide band gap semiconductor (ZnS / 3.7 eV) and a narrow band gap

semiconductor (Bi_2S_3 / 1.3 eV) provided limited success with initial synthesis efforts showing crystalline ZnS material being formed in analysis of the powders by X-ray diffraction (Figure 6.2) with additional crystalline material being formed as the microwave time increased.

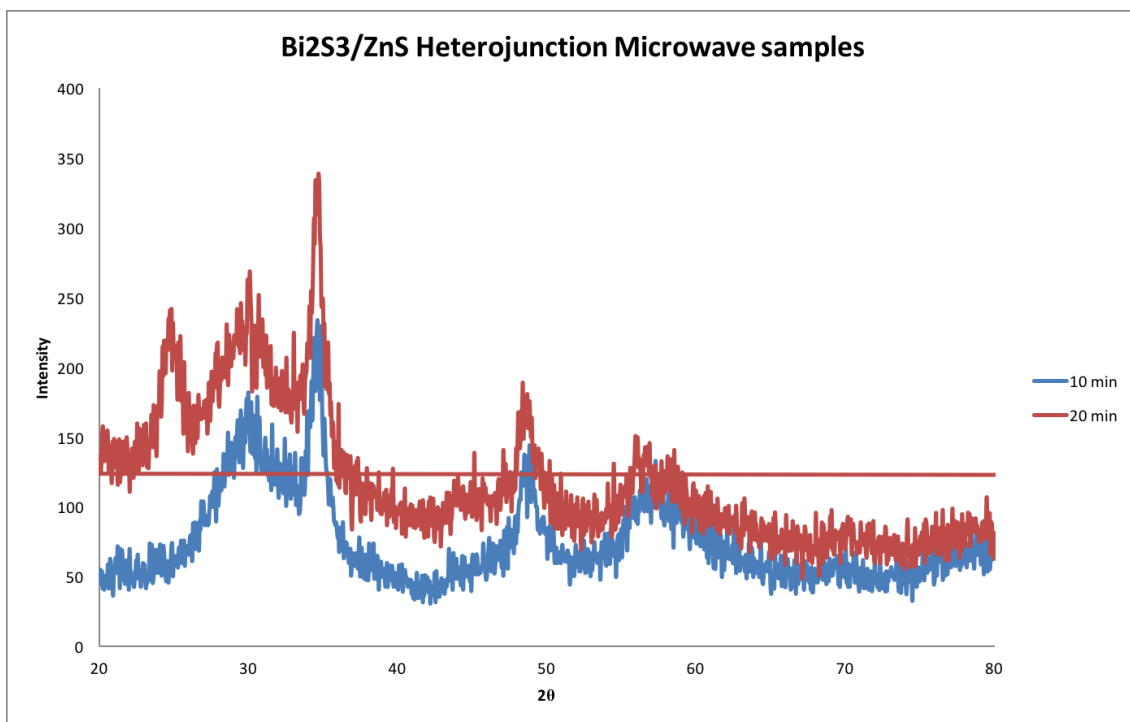


Fig 6.2. Example of XRD data for a $\text{ZnS}/\text{Bi}_2\text{S}_3$ heterojunction prepared in the microwave at 600 W for period of 10 and 20 min

Initial photocatalytic testing using this combination $\text{ZnS}/\text{Bi}_2\text{S}_3$ material showed a reduction in the activity compared to the ZnS by itself. It is hypothesised that this was due to the reduced crystallinity compared to ZnS prepared under the same conditions. Further work to optimise the synthesis conditions and characterisation of the material would lead to an interesting visible light photoactive material.

Further metal dopants to be explored as part of this work include cerium. Cerium like the group 13 metals studied in chapter 4 has a 3+ oxidation state and like indium has a ionic radius larger (1.03 Å) than the Zn^{2+} (0.74 Å) potentially leading to interesting doping activity for enhanced luminescence and photocatalytic activity.⁸² The future work involving cerium would include synthesis of a series of cerium doped ZnS at different levels, characterisation of the materials and determination of the photocatalytic activity to determine the optimum dopant level.

Work on coating of the prepared powders as thin films on glass was in the preliminary phases upon completion of the project including incorporating the powders into dispersion mediums and synthesis of thin films directly onto glass in the microwave. For the use of the prepared powders, they were reduced to a finer powder in a pestle and mortar and dispersed in polyethylene glycol and then a dip-coating technique used to prepare the films. Further study is required to determine the optimum conditions including concentration of ZnS in the PEG medium, number of dips, withdrawal rate and drying temperatures to figure out the optimum photocatalytic

For the microwave synthesis directly onto glass slides, the glass slides were inserted at an angle into the precursor solution inside the microwave. The conditions used were the optimum ZnS conditions, namely 600 W, 0.2 M precursor concentration and an irradiation time of 30 mins. At the end of the irradiation period, there was powder at the base of the beaker and on the glass slides there was residue with a milky white appearance. X-ray diffraction of these glass slides showed a similar pattern to the blank glass slides showing either no crystalline material was deposited on the glass slides or any material that was there wasn't in sufficient quantity to be identified by the XRD.

One further class of materials whose synthesis could be explored by the ambient pressure microwave synthesis using aqueous dissolvable starting materials is the delafossite class of materials. Delafossite structured oxides are denoted by ABO_2 (figure 6.3) which include d^{10} metals ions such Cu^+ or Ag^+ .¹⁹⁸ Delafossite materials such as $CuGaO_2$ and $AgGaO_2$, $AgLi_{1/3}Ti_{2/3}O_2$ for various applications such as hydrogen production by degradation of H_2S ¹⁹⁹, photocatalytic degradation of pollutants¹⁹⁸, and photocatalytic water splitting.²⁰⁰

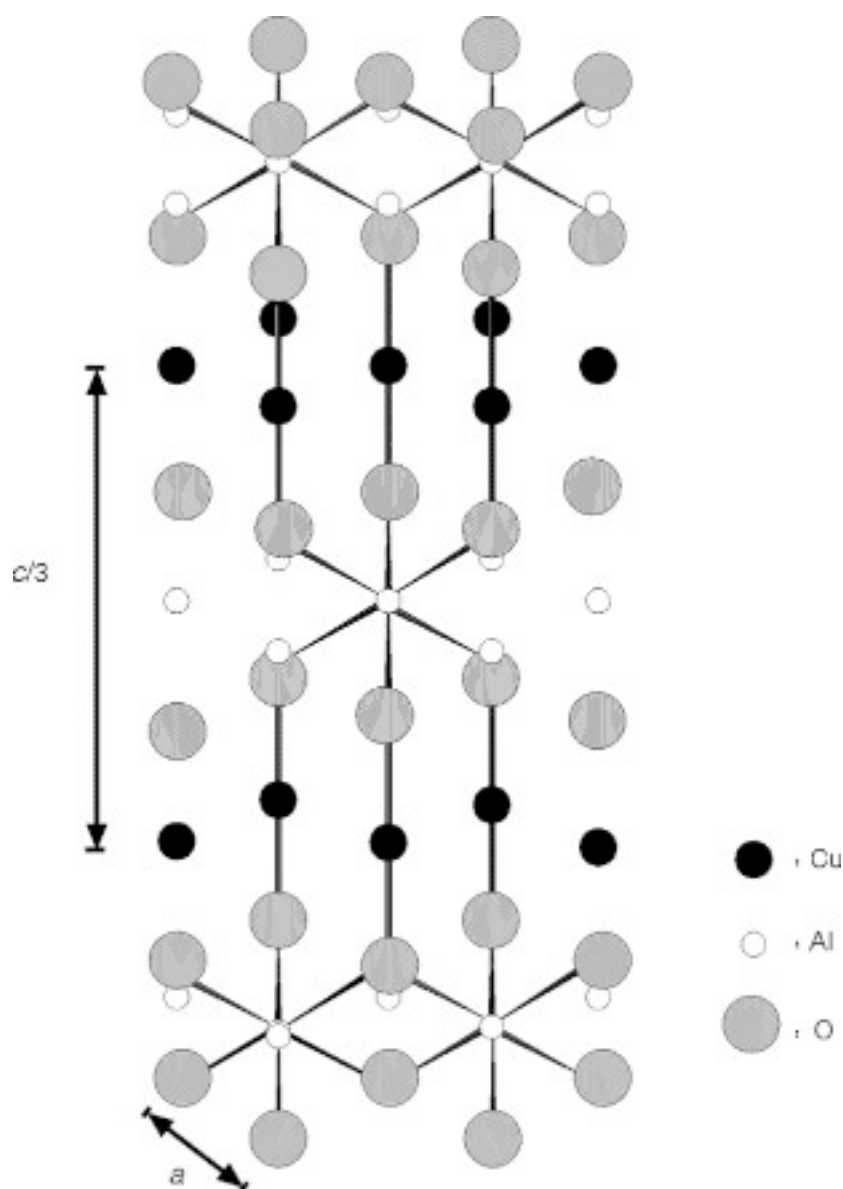


Fig 6.3. Structure of Delafossite material demonstrated with $CuAlO_2$

Delafossite based materials have been shown to be visible light active and do not require dopants or sensitizers to be active in indoor light conditions. The delafossite materials prepared by the ambient pressure microwave synthesis technique were based on Ag in A position and In/Ga in the B position of the ABO_2 structure. These were prepared by varying the concentration of the indium and gallium based precursor material. Figure 6.4 shows the X-ray diffraction patterns obtained for these materials which is consistent with previously reported patterns.^{198,199}

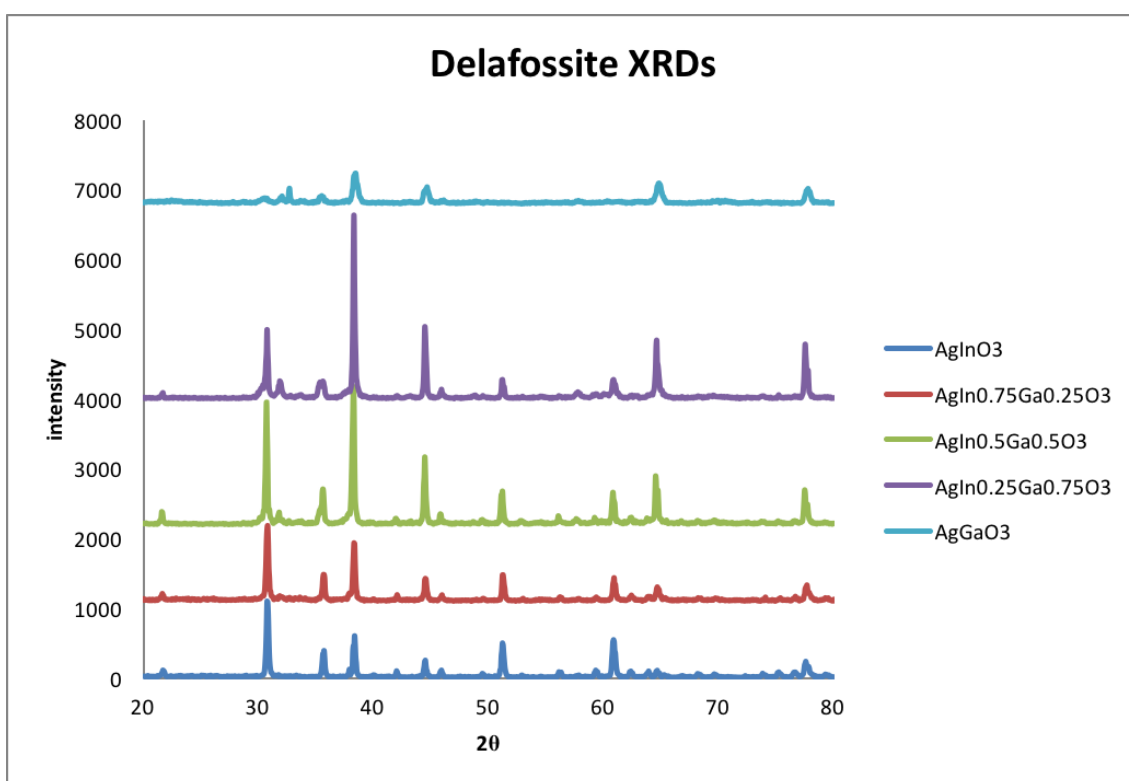


Fig 6.4. X-ray diffraction patterns for AgInO₂ and AgGaO₂ and combinations of In and Ga in the B position for delafossites.

Diffuse reflectance showed that these materials showed visible light absorbance up to 500 nm characterised by the yellow to brown colour of the powders generated by the synthesis. Preliminary photocatalytic activity studies using methylene blue proved difficult due to absorption of the dye onto the materials. Further work is required to

complete the characterisation of these materials including XPS, electron microscopy and the development of an appropriate photocatalytic test.

Publications by the Author

- Chapter 3 - Anti-bacterial activity of indoor-light activated photocatalysts
Damian W. Synnott, Michael K. Seery, Steven J. Hinder, Georg Michlits, Suresh C. Pillai, *Applied Catalysis B: Environmental* 130– 131 (2013) 106– 111
- Chapter 5 - Novel microwave assisted synthesis of ZnS nanomaterials
Damian W Synnott, Michael K Seery, Steven J Hinder, John Colreavy and Suresh C Pillai, *Nanotechnology* 24 (2013) 045704
- Effect of N-doping on the photocatalytic activity of sol–gel TiO₂
NT Nolan, DW Synnott, MK Seery, SJ Hinder, A Van Wassenhoven, S Pillai, *Journal of Hazardous Materials* 211 (2012) 88-94
- Evaluating the Mechanism of Visible Light Activity for N,F-TiO₂ using Photoelectrochemistry
JWJ Hamilton, JA Byrne, PSM Dunlop, DD Dionysiou, M. Pelaez, K O’Shea, D Synnott, S. Pillai, *Journal of Physical Chemistry C*, 118 (2014) 12206-12215
- An effective method for the preparation of high temperature stable anatase TiO₂ photocatalysts
R. Fagan, DW Synnott, DE McCormack, SC Pillai, *Applied Surface Science*, 371 (2016) 447-452
- First author of Chapter 13 “Self-cleaning Tiles and Glass for Eco-Efficient Buildings” in *Nanotechnology In Eco-Efficient Construction* edited by F. Pacheco-Torgal *et al.*
Published by Woodhead Publishing in April 2013

Presentations by the Author

- A Novel Microwave Assisted Synthesis of Doped ZnS for the Development of Indoor Light Activated Anti-Bacterial Materials
 - Chemistry Colloquium, Queens University, Belfast 2010 – Applied Chemistry Best Talk Winner

References

- ¹ A. Pal, S. O. Pehkonen, L. E. Yu, M. B. Ray, *J. Photochem. Photobio. A: Chemistry*, 2007, **186**, 335-341
- ² A. Kubacka, M. Ferrer, A. Martinez-Arias, M. Fernandez-Garcia, *Appl. Catal. B. Env*, 2008, **84**, 87-93
- ³ C.J. Chung, H.I. Lin, H.K. Tsou, Z.Y. Shi, J.L. He, *J. Biomed Mater Res B Appl Biomater*, 2008, **85**, 220-224
- ⁴ L. B. Gasink, E. Lautenbach, *Med Clin N Am*, 2008, **95**, 295-313
- ⁵ P. W. Stone, D. Braccia, E. Larson, *Am J Infect Control*, 2005, **33**, 501-509
- ⁶ Prevention and Control of Methicillin-Resistant Staphylococcus aureus (MRSA) National Clinical Guideline No. 2 – ROI Department of Health 2013
- ⁷ Point prevalence survey of healthcare-associated infections and antimicrobial use in European long-term care facilities, May 2013, European Centre for Disease Prevention and Control
- ⁸ R. Kock, K. Becker, B. Cookson, J. E. van Gemert-Pijnen, S. Harbarth, J. Kluytmans, M. Mielke, G. Peters, R. L. Skov, M. J. Struelens, E. Tacconelli, W. Witte, A. W. Friedrich, *Eurosurveillance*, 2014, **19**, 23-49
- ⁹ I. M. Gould, *Journal of Hospital Infection*, 2005, **61**, 277-282
- ¹⁰ European Antimicrobial Resistance Surveillance System annual report, 2003
- ¹¹ D. J. Diekeme, B.J. Bootsmler, T. E. Vaughan, *Clin Infect Dis*, 2004, **38**, 78-85
- ¹² B. P. Howden, P. B. Ward, P. G. P. Charles, *Clin Infect Dis*, 2004, **38**, 521-528
- ¹³ S. Kim, W. Park, K. Lee, *Clin Infect Dis*, 2003, **37**, 794-799
- ¹⁴ E. Donnellan, *Irish Times*, 24-08-2005
- ¹⁵ L. Lukasiak, A. Jakubowski, *JTIT*, 2010, **1**, 3-9
- ¹⁶ Inorganic Chemistry, 2nd Edition, G. L. Miessler, D. A. Tarr, Prentice Hall
- ¹⁷ H. Fujiwara, H. Hosokawa, K. Murakoshi, Y. Wada, S. Yanagida, *Langmuir*, 1998, **14**, 5154-5159
- ¹⁸ A. Fujishima, K. Honda, *Nature*, 1972, **238**, 37-38
- ¹⁹ K. Sunada, Y. Kikuchi, K. Hashimoto, A. Fujishima, *Environmental science and Technology*, 1998, **32**, 726-728
- ²⁰ R. N. Bhargava, D. Gallagher, *Phys. Rev. Lett.* 1994, **72**, 416
- ²¹ H. Hu, W. Zhang *Optical Materials*, 2006, **28**, 536-550
- ²² Z. He, Y. Su, Y. Chen, D. Cai, J. Jiangm L. Chen *Materials Research Bulletin*, 2005, **40**, 1308-1313
- ²³ W. Q. Peng, G. W. Cong, S. C. Qu, Z. G. Wang, *Optical Materials*, 2006, **29**, 313-317
- ²⁴ T. Arai, S. Senda, Y. Sato, H. Takahashi, K. Shinoda, B. Jeyadevan, K. Tohji, *Chem. Mater.* 2008, **20**, 1997-2000
- ²⁵ M. Muruganandham, Y. Kusumoto *J. Phys. Chem. C*, 2009, **113**, 16144-16150
- ²⁶ Y. Gou, Z. Su, Z. Xue, *Materials Research Bulletin*, 2004, **39**, 2203-2208
- ²⁷ G. Ghosh, M. K. Naskar, A. Patra, M. Chatterjee, *Optical Materials*, 2006, **28**, 1047-1053
- ²⁸ C. Bi, L. Pan, M. Xu, J. Yin, L. Qin, J. Liu, H. Zhu, J. Q. Xiao, *Mater. Chem. And Phys.*, 2009, **116**, 363-367
- ²⁹ X. Fang, T. Zhai, U. K. Gautam, L. Li, L. Wu, Y. Bando, D. Golberg, *Progress in Materials Science*, 2011, **56**, 175-287

-
- ³⁰ G. Li, J. Zhai, D. Li, X. Fang, H. Jiang, Q. Dong, E. Wang, *J Mater Chem*, 2010, **20**, 9215
- ³¹ J. Geng, B. Liu, F. N. Hu, J. J. Zhu, *Langmuir*, 2007, **23**, 10286
- ³² G. Z. Shen, Y. Bando, J. Q. Hu, D. Golberg, *Appl. Phys. Lett.* 2007, **90**, 123101
- ³³ J. S. McCloy, R. Korenstein, B. Zelinski, *J Am Chem Soc*, 2009, **92**, 1725
- ³⁴ Y. C. Chen, C. H. Wang, H. Y. Lin, B. H. Li, W. T. Chen, C. P. Liu, *Nanotechnology*, 2010, **21**, 455604
- ³⁵ M. Salavati-Niasari, M. R. Loghman-Estarki, F. Davar, *Journal of Alloys and Compounds*, 2009, **475**, 782-788
- ³⁶ D. Denzler, M. Olschewski, K. Sattler, *J. Appl. Phys.*, 1998, **84**, 2841-2845
- ³⁷ H. Zhang, B. Chen, B. Gilbert, J. F. Banfield, *J. Mater. Chem.*, 2006, **16**, 249-254
- ³⁸ C. Y. Yeh, Z. W. Lu, S. Froyen, A. Zunger, *Phys Rev B*, 1992, **46**, 10086-10097
- ³⁹ Y. C. Zhang, G. Y. Wang, X. Y. Hu, W. W. Chen., *Materials Research Bulletin*, 2006, **41**, 1817-1824
- ⁴⁰ H. Y. Sun, X. H. Li, W. Li, F. Li, B. T. Liu, X. Y. Zhang, *Nanotechnology*, 2007, **18**, 115604-115607
- ⁴¹ C. Jiang, W. Zhang, G. Zou, W. Yu, Y. Qian, *Materials Chemistry and Physics*, 2007, **103**, 24-27
- ⁴² J. S. Jang, C. J. Yu, S. H. Choi, S. M. Ji, E. S. Kim, J. S. Lee, *Journal of Catalysis*, 2008, **254**, 144-155
- ⁴³ S. Kohtani, Y. Ohama, Y. Ohno, I. Tsuji, A. Kudo, R. Nakagaki, *Chemistry Letters*, 2005, **34**, 1056-1057
- ⁴⁴ H. Yin, Y. Wada, T. Kitamura, S. Yanagida, *Environ. Sci. Technol.*, 2001, **35**, 227-231
- ⁴⁵ X. Meng, H. Xiao, X. Wen, W. A. Goddard. S. Li, G. Qin, *Phys. Chem. Chem. Phys.*, 2013, **15**, 9531
- ⁴⁶ B. Liu, X/ Zhao, C. Terashima, A. Fujishima, K. Nakata, *Phys. Chem. Chem. Phys.*, 2014, **16**, 8751-8760
- ⁴⁷ X. Fang, L. Wu, L. Hu, *Adv. Mater.*, 2011, **23**, 585-598
- ⁴⁸ H. Shao, X. Qian, B. Huang *Materials Letters*, 2007, **61**, 3639-3643
- ⁴⁹ Z. Wang, L. L. Daemen, Y. Zhao, C. S. Zha, R. T. Downs, X. Wang, Z. L. Wang, R. J. Hemley *Nature Materials*, 2005, **4**, 922-927
- ⁵⁰ Y. Zhao, J. M. Hong, J. J. Zhu, *Journal of Crystal Growth*, 2004, **270**, 438-445
- ⁵¹ H. Y. Lu, S. Y. Chu, S. S. Tan, *Journal of Crystal Growth*, 2004, **269**, 385-391
- ⁵² Y. Y. Bacherikov, I. S. Golovina, N. V. Kitsyuk, *Physics of the Solid State*, 2006, **48**, 1872-1878
- ⁵³ T. Kryshtab, J. Palacios Gomez, M. Mazin, *Z. Kristallogr. Suppl.* 2006, **23**, 287-292
- ⁵⁴ H. Zhang, L. Qi, *Nanotechnology*, 2006, **17**, 3984-3988
- ⁵⁵ W. Chen, Z. Wang, Z. Lin, L. Lin, *J. Appl. Phys.*, 1997, **82**, 3111-3115
- ⁵⁶ I. Tsuji, H. Kato, A. Kudo, *Angew. Chem.*, 2005, **117**, 3631-3634
- ⁵⁷ J. H. Bang, R. J. Helmich, K. S. Suslick, *Adv. Mater.*, 2008, **20**, 2599-2603
- ⁵⁸ H.F. Shao, X. F. Qian, Z. K. Zhu, *Journal of Solid State Chemistry*, 2005, **178**, 3522-3528
- ⁵⁹ L. Dong, Y. Chu, Y. Zhang, Y. Liu, F. Yang *Journal of Colloid and Interface Science*, 2007, **308**, 258-264
- ⁶⁰ J. S. Hu, L. L. Ren, Y. G. Guo, H. P. Liang, A. M. Cao, L. J. Wan, C. L. Bai, *Angew. Chem.*, 2005, **44**, 1269-1273
- ⁶¹ M. Y. Lu, M. P. Lu, Y. A. Chung, M. J. Chen, Z. L. Wang, L. J. Chen, *J. Phys. Chem. C.*, 2009, **113**, 12878-12882

-
- ⁶² J. Yang, J. Peng, R. Zou, F. Peng, H. Wang, H. Yu, J. Lee, *Nanotechnology*, 2008, **19**, 255603-255609
- ⁶³ H. Zhang, X. Chen, Z. Li, J. Kou, T. Yu, Z. Zou, *Nanotechnology*, 2007, **40**, 6846-6849
- ⁶⁴ L. Wang, L. Chen, T. Luo, Y. Qian, *Mater. Lett.*, 2006, **60**, 3627-3630
- ⁶⁵ C. Jiang, W. Zhang, G. Zou, W. Yu, Y. Qian, *Mater. Chem and Phys.* 2007, **103**, 24-27
- ⁶⁶ Z. Li, W. Shen, L. Fang, X. Zu, *J. Alloys and Compounds*, 2008, **463**, 129-133
- ⁶⁷ C. Jiang, W. Zhang, G. Zou, W. Yu, Y. Qian, *Materials Chemistry and Physics*, 2007, **103**, 24-27
- ⁶⁸ Z. Li, B. Liu, X. Li, S. Yu, L. Wang, Y. Hou, Y. Zou, M. Yao, Q. Li, B. Zou, T. Cui, G. Zou, G. Wang, Y. Li, *Nanotechnology*, 2007, **18**, 255602-2255609
- ⁶⁹ Z. Li, W. Shen, L. Fang, X. Zu, *Journal of Alloys and Compounds*, 2008, **463**, 129-133
- ⁷⁰ S. Senthilkumar, R. Thamiz Selvi, *Appl. Phys. A*, 2009, **94**, 123-129
- ⁷¹ D. Denzier, M. Olschewski, K. Sattler, *J. Appl. Phys.*, 1998, **84**, 2841-2845
- ⁷² A. D. Dinsmore, D. S. Hsu, S. B. Qadri, J. O. Cross, T. A. Kennedy, H. F. Gray, B. R. Ratina *J. Appl. Phys.* 2000, **88**, 4985-4993
- ⁷³ M. K. Naskar, A. Patra, M. Chatterjee *Journal of Colloid and Interface Science*, 2006, **297**, 271 - 275
- ⁷⁴ S. K. Panda, A. Datta, S. Chaudhuri, *Chemical Physics Letters*, 2007, **440**, 235-238
- ⁷⁵ http://www.colorado.edu/physics/2000/waves_particles (accessed July 2012)
- ⁷⁶ H. Yu, X. Zhang, N. Ma, S. Chen H. Zhao, *Langmuir*, 2008, **24**, 7599-7604
- ⁷⁷ The Elements of Physical Chemistry, P. Atkins, Oxford Press, 3rd Edition, 2002
- ⁷⁸ R. N. Gedye, F. E. Smith, K.C. Westaway, H. Ali, L. Baldisera, L. Laberage and J. Rousell, *Tetrahedron Letters*, 1986, **27**, 279
- ⁷⁹ R. J. Giguere, *Organic Synthesis: Theory and Applications*, Vol 1, JAI Press Inc, 1989, 103-172
- ⁸⁰ R.N. Gedye, F.E. Smith, K.C. Westaway, *Canadian Journal of Chemistry*, 1998, **66**, 17
- ⁸¹ M. Tsuji, M. Hashimoto, Y. Nishizawa, M. Kubokawa, T. Tsuji *Chemistry A European Journal*, 2005, **11**, 440-452
- ⁸² H. Yang, C. Huang, X. Su, A. Tang, *Journal of Alloys and Compounds*, 2005, **402**, 274-277
- ⁸³ A.B. Panda, G. Glaspell, M.S. El-Shall, *J. Am. Chem. Soc.*, 2006, **128**, 2790-2791
- ⁸⁴ R. Zhai, S. Wang, H. Xu, H. Wang, H. Yan, *Materials Letters*, 2005, **59**, 1497-1501
- ⁸⁵ X. H. Liao, J. J. Zhu, H. Y. Chen *Materials Science and Engineering B*, 2001, **85**, 85-89
- ⁸⁶ J. Zhu, M. Zhou, J. Xu, X. Liao, *Materials Letters*, 2001, **47**, 25-29
- ⁸⁷ J. Q. Sun, Z. P. Shen, K. M. Chen, Q. Liu, W. Liu, *Solid State Communications*, 2008, **147**, 501-504
- ⁸⁸ Y. Zhao, J.M. Hong, J.J. Zhu, *Journal of Crystal Growth*, 2004, **270**, 438-445
- ⁸⁹ A.I. Onyia, H.I. Ikei, A.N. Nurobodo, *Journal of Ovonic Research*, 2018, **14**, 49-54
- ⁹⁰ R. Bhadra, V. N. Singh, B. R. Mehta, P. Datta, *Chalcogenide Letters*, 2009, **6**, 189-196
- ⁹¹ A. R. West, *Basic Solid Chemistry*, Wiley Press, 2nd Edition, 1999
- ⁹² Z. Wang, L.L. Daemen, Y. Zhao, C.S. Zha, R.T. Downs, Z. Wang, Z.L. Wang, R.J. Hemley, *Nature Materials*, 2005, **4**, 922
- ⁹³ P. Atkins, *Physical Chemistry*, Oxford University Press, 7th Edition, 2002
- ⁹⁴ P. Hu, Y.Cao, Y. Lou, B. Lu, M. Shao, J. Ni, M. Cao, *Advances in Materials Physics and Chemistry*, **2013**, 3, 10-18
- ⁹⁵ Brunauer S.; Emmet P. H.; Teller E. *J. Am. Chem. Soc.* **1938**, 60, 309
- ⁹⁶ Atkins, *Physical Chemistry*, 7th Edition, Oxford Press
- ⁹⁷ W. Chen, H. Xiao, H. Xu, T. Ding, *Int. J. of Photoenergy*, **2015**, 1

-
- ⁹⁸ Peng, W.Q.; Cong, G.W.; Qu, S.C.; Wang, Z.G. *Optical Materials*, **2006**, *29*, 313
- ⁹⁹ Bacaksiz, E.; Görür, O.; Tomakin, M.; Yanmaz, E.; Altunbas, M. *Materials Letters*, **2007**, *61*, 5239
- ¹⁰⁰ Jiang, C.; Zhang, W.; Zou, G.; Yu, W.; Qian, Y. *Materials Chemistry and Physics*, **2007**, *103*, 24
- ¹⁰¹ Feng, G.; Li, C.Z.; Wang, S.F.; Lü, M.K. *Langmuir*, **2006**, *22*, 1329
- ¹⁰² Li, Y.; Li, X.; Yang, C.; Li, Y. *J. Phys. Chem. B*, **2004**, *108*, 16002
- ¹⁰³ Gou, Y.; Su, Z.; Xue, Z. *Mater. Res. Bull.*, **2004**, *39*, 2203
- ¹⁰⁴ Wang, G.Z.; Geng, B.Y.; Huang, X.M.; Wang, Y.W.; Li, G.H.; Zhang, L.D. *Applied Physics A*, **2003**, *77*, 933
- ¹⁰⁵ Li, W. H. *Materials Letters*, **2008**, *62*, 243-245
- ¹⁰⁶ Liao, X. -H.; Wang, H.; Zhu, J. -J.; Chen, H. -Y.; *Mater. Res. Bull.*, **2001**, *36*, 2339-236
- ¹⁰⁷ Subhendu, K. P.; Dalta, A.; Chaudhari, S. *Chemical Physics Letters*, **2007**, *440*, 235-238
- ¹⁰⁸ Zhang, H.; Li, Q. *Nanotechnology*, **2006**, *17*, 3984-3988
- ¹⁰⁹ Y. Zhao, J.M. Hong, J.J. Zhu. *J. Crystal Growth*, 2004, **270**, 438-445
- ¹¹⁰ J. Zhu, M. Zhou, J. Xu, X. Liao, *Mater. Lett.*, 2001, **47**, 25-29
- ¹¹¹ C. M. Huang, K. W. Cheng, Y. R. Jhan, T. W. Chung, *Thin Solid Films*, 2007, **515**, 7935
- ¹¹² M. V. Limaye, S. Gokhale, S. A. Archarya, S. K. Kulkarni, *Nanotechnology*, 2008, **19**, 415602
- ¹¹³ S. K. Mehta, S. Kumar *J. Lumin.* **120** (2010) 2377
- ¹¹⁴ Y. Li, Y. Ding, Y. Zhang, Y. Qian, *J. Phys. Chem. Solids*, 1999, **60**, 13-15
- ¹¹⁵ M. Scocioreanu, M. Baibarac, I Baltog, I Pasuk, T. Velula *J. Solid State Chem.* **186** (2012) 217
- ¹¹⁶ G. Li, J. Zhai, D. Li, X. Fang, H. Jiang, Q. Dong, E. Wang *J. Mater. Chem.* **20** (2010) 9215
- ¹¹⁷ R. Brayer, R. Ferrari – Iliou, N. Brivois, S. Djediat, M. F. Benedetti, F. Fievet *Nano Lett.* **6** (2006) 866
- ¹¹⁸ K. M. Reddy, K. Feris, J. Bell, D. G. Wingett, C. Hanley, A. Punnoose *Appl. Phys. Lett.* **90** (2007) 213902
- ¹¹⁹ M. Pelaez, P. Falcras, V. Likodimos, A. G. Kontos, A. A. De la Cruz, K. O’ Shea, D. D. Dionysiou *Appl. Catal. B* **99** (2010) 378
- ¹²⁰ A. G. Rincón, C. Pulgarin *Appl. Catal. B* **49** (2004) 99
- ¹²¹ Kiwi, J.; Nadtochenko, V. *Langmuir* **21** (2005) 4631
- ¹²² A. Kudo, R. Niishiro, A. Iwase, H. Kato, *Chemical Physics*, 2007, **339**, 104-110
- ¹²³ T. Arai, S. Senda, Y. Sato, H. Takahashi, K. Shinoda, B. Jeyadevan, K. Tohji, *Chem. Mater.* 2008, **20**, 1997-2000
- ¹²⁴ S. Kohtani, Y. Ohama, Y. Ohno, I. Tsuji, A. Kudo, R. Nakagaki, *Chemistry Letters*, 2005, **34**, 1056-1057
- ¹²⁵ C. Xing, Y. Zhang, W. Yan, L. Guo, *International Journal of Hydrogen Energy*, 2006, **31**, 2018-2024
- ¹²⁶ R.N. Bhargava, D. Gallangher, T.Welker, *J. Luminescence* **60** (1991) 275
- ¹²⁷ T. Igarashi, T. Isobe, M. Senna, *Phys. Rev. B* **56** (1995) 6444
- ¹²⁸ A.A. Bol, A. Meijerink, *Phys. Rev. B* **58R** (1998) 15997
- ¹²⁹ N. Murase, R. Jagannathan, Y. Kanematsu, M.Watanabe, A. Kuritha, K. Hirata, T. Yazawa, T. Kushida, *J. Phys. Chem. B* **103** (1999) 754

-
- ¹³⁰ O. A. Korotchenkov, A. Cantarero, A. P. Shpak, Y. A. Kunitskii, A. I. Senkevich, M. O. Borovoy, A. B. Nadtochii, *Nanotechnology*, 2005, **16**, 2033-2038
- ¹³¹ S. W. Lu, H. K. Schmidt, *Materials Research Bulletin*, 2008, **43**, 583-589
- ¹³² Q. Zhai, J. Li, J. S. Lewis, K. A. Waldrip, K. Jones, P. H. Holloway, M. Davidson, N. Evans, *Thin Solid Films*, 2002, **414**, 105-112
- ¹³³ W. Jian, J. Zhuang, W. Yang, Y. Bai, *Journal of Luminescence*, 2007, **126**, 735-740
- ¹³⁴ N. Karar, *Solid State Communications*, 2007, **142**, 261-264
- ¹³⁵ H. Yang, C. Huang, X. Su, A. Tang, *Journal of Alloys and Compounds*, 2005, **402**, 274-277
- ¹³⁶ T. V. Butkhuzi, T. G. Tchelidze, E. G. Chikoidze, N. P. Kekelidze, *Phys. Stat. Sol.*, 2002, **229**, 365-370
- ¹³⁷ C. Bi, L. Pan, M. Xu, J. Yin, L. Qin, J. Liu, H. Zhu, J. Q. Xiao, *Materials Chemistry and Physics*, 2009, **116**, 363-367
- ¹³⁸ P. Yang, M. Lu, D. Xu, D. Yuan, C. Song, G. Zhou, *Journal of Physics and Chemistry of Solids*, 2001, **62**, 1181-1184
- ¹³⁹ R. Sakar, C. S. Tiwary, P. Kumbhakar, A. K. Mitra, *Physica B: Condensed Matter*, 2009, **404**, 3855-3858
- ¹⁴⁰ K. Manzoor, S. R. Vadera, N. Kumar, T. R. N. Kutty, *Materials Chemistry and Physics*, 2003, **82**, 718-725
- ¹⁴¹ S. Shinoya, W.M. Yen, Phosphor Handbook, CRC Press, Washington, DC, 1999
- ¹⁴² A.A. Khosrav, M. Kundu, L. Jatwa, S.K. Deshpande, V.A. Bhgawat, M. Shastry, S.K. Kulkarni, *Appl. Phys. Lett.* 67 (1995) 2705
- ¹⁴³ M. Wang, L. Sun, X. Fu, C. Liao, C. Yan, *Solid State Commun.* 115 (2000) 493
- ¹⁴⁴ C. Corrado, Y. Jiang, F. Oba, M. Kozina, F. Bridges, J. Z. Zhang, *J. Phys. Chem. A*, 2009, **113**, 3830-3839
- ¹⁴⁵ P. Yang, M. Lu, D. Xu, D. Yuan, J. Chang, G. Zhou, M. Pan, *Appl. Phys. A*. 2002, **74**, 257-259
- ¹⁴⁶ H. Soni, M. Chawda, D. Bodas, *Materials Letters*, 2009, **63**, 767-769
- ¹⁴⁷ P. H. Borse, N. Deshmukh, R. F. Shinde, S. K. Date, S. K. Kukarni, *Journal of Materials Science*, 1999, **34**, 6087-6093
- ¹⁴⁸ S.C. Qu, W.H. Zhou, F.Q. Liu, N.F. Chen, Z.G. Wang, *Appl. Phys. Lett.* 80 (2002) 3605
- ¹⁴⁹ W. Chen, J.O. Malm, V. Zwiller, R. Wallenberg, J.O. Bovin, *J. Appl. Phys.* 89 (2001) 2671
- ¹⁵⁰ J. Planelles-Arago, B. Julian-Lopez, E. Cordocillo, P. Escribano, F. Pelle, B. Viana, C. Sanchez, *J. Mater. Chem.*, 2008, **18**, 5193-5199
- ¹⁵¹ E.M. Nasir, *International Journal of Innovative Research in Science Engineering and Technology*, 2007, **3**, 8114-8120
- ¹⁵² F. A. La Porta, M.M. Ferrer, Y.V.B. de Santana, C.W. Raubach, V.M. Longo, J.R. Sambrano, E. Longo, J. Andres, M.S. Li, J.A. Varela, *Journal of Alloys and Compounds*, 2013, **556**, 153-159
- ¹⁵³ N. Soltani, E. Saion, M. Erfani, K. Rezaee, G. Bahmanrokh, G.P.C. Drummen, A. Bahrami, M.Z. Hussein, *Int. J. Mol. Sci.*, 2012, **13**, 12412-12427
- ¹⁵⁴ S. Shen, J. Chen, X. Wang, L. Zhao, L. Guo, *Journal of Power Sources*, 2011, **196**, 10112-10119
- ¹⁵⁵ K. Nagamani, N. Revathi, P. Prathap, Y. Lingappa, K. T. Ramakrishna Reddy, *Current Applied Physics*, 2012, **12**, 380-384
- ¹⁵⁶ W. Q. Peng, G. W. Cong, S. C. Qu, Z. G. Wang, *Optical Materials*, 29 (2006) 313

-
- ¹⁵⁷ M. Scocioreanu, M. Balbarac, I. Baltog, I. Pasuk, T. Velula, *Journal of Solid State Science*, 186 (2012) 217
- ¹⁵⁸ S. K. Mehta, S. Kumar, *Journal of Luminescence* 120 (2010), 2377
- ¹⁵⁹ P. Yang, M. Lu, D. Xu, D. Yuan, M. Pan, G. Zhou, *Materials Research Bulletin*, 2001, **36**, 1301-1306
- ¹⁶⁰ E. Pal, V. Hornok, A. Oszko, I. Dekany, *Colloids and Surfaces A: Physicochemical and Engineering Aspects*, 340 (2009) 1-9
- ¹⁶¹ Y. Li, G. Chen, C. Zhou, J. Sun, *ChemComm*, 15 (2009) 2020-2022
- ¹⁶² R. Georgekutty, M. K. Seery, P. Floris, S. C. Pillai, *J. Photochem. and Photobiol. A: Chemistry*, 2007, **189**, 258-263
- ¹⁶³ R. Georgekutty, M. K. Seery, S. C. Pillai, *J. Phys. Chem. B.*, 2008, **112**, 13563-13570
- ¹⁶⁴ W. Smith, S. Mao, G. Lu, A. Catlett, J. Chen, Y. Zhao, *Chemical Physics Letters*, 2010, **485**, 171-175
- ¹⁶⁵ B. Sumana, K. Sarayu, B. Bruno, R. Udhaya, S. Sandhya, *International Journal of Environmental Sciences*, 2013, **4**, 106-112
- ¹⁶⁶ W. Xie, Y. Li, W. Sun, J. Huang, H. Xie, X. Zhao, *Journal of Photochemistry and Photobiology A: Chemistry*, 2010, **216**, 149-155
- ¹⁶⁷ A. Kafizas, C.W. Dunnill, I.P. Parkin, *Phys. Chem. Chem. Phys.* 2011, **13**, 13827-13838
- ¹⁶⁸ J.W. Alexander, *Surgical Infections*, 2009, **10**, 289-292
- ¹⁶⁹ G. Schneider, *Can. Med. Assoc. J.*, 1984, **131**, 375-398
- ¹⁷⁰ Guggenbichler et al., *Infection*, 1999, **1**, S16-S23
- ¹⁷¹ A.B. Iansdown. *Curr. Probl. Dermatol.* 2006, **33**, 33-
- ¹⁷² L. Yin, Y. Bando, *Nature Materials*, 2005, **4**, 883-884
- ¹⁷³ Z. Wang, L.L. Daemen, Y. Zhao, C.S. Zha, R.T. Downs, X. Wang, Z.L. Wang, R.J. Hemley, *Nature Materials*, 2005, **4**, 922-927
- ¹⁷⁴ H. Zhang, F. Huang, B. Gilbert, J.F. Banfield, *J. Phys. Chem. B.*, 2003, **107**, 13051-13060
- ¹⁷⁵ X.H. Liao, H. Wang, H. Y Chen, *Sci. Eng. B – Solid.* 2001, **85**, 85
- ¹⁷⁶ E. Omurzak, T. Mashimo, S. Sulaimankulova, S. Takebe, L. Chen, Z. Abdullaeva, C. Iwamoto, Y. Oishi, H. Ihara, H. Okudera, A. Yoshiasa, *Nanotechnology*, 2011, **22**, 365602
- ¹⁷⁷ Limage M V, Gokhale S, Acharya S A and Kalkarni S K 2008 *Nanotechnology* **19** 451602
- ¹⁷⁸ C. Cheng, G. Xu, H. Zhang, J. Cao, P. Jiao, X. Wang, *Mater. Lett.* 2006, **60**, 3561
- ¹⁷⁹ X. Wang, J. Shi, Z. Feng, M. Li, C. Li, *Phys. Chem. Chem. Phys.* 2011, **13**, 4715
- ¹⁸⁰ D. Banhemann, *Sol. Energy*, 2004, **77**, 445
- ¹⁸¹ T. Kryshtab, J. Palacios Gomez, M. Marin, *Krist.Suppl.* 2006, **23**, 287
- ¹⁸² Y. Li, G. Chen, C. Zhou, J. Sun, *Chem. Commun.*, 2009, **15**, 2020
- ¹⁸³ T. Guo, Y. Chen, L. Liu, Y. Cheng, X. Zhang, B. Ma, M. Wei, *Cryst. Res. Technol.*, 2012, **47**, 449
- ¹⁸⁴ R. Georgekutty, M. K. Seery, S. C. Pillai, *J. Phys. Chem.C*, 2008, **112**, 13563
- ¹⁸⁵ M. K. Seery, R. George, P. Floris, S. C. Pillai, *J. Photochem. Photobiol. A*, 2007, **189**, 258
- ¹⁸⁶ M. Pelaez et al, *Appl. Catal. B*, 2012, **125**, 331
- ¹⁸⁷ N. T. Nolan, M. K. Seery, S. J. Hinder, L. F. Healy, S. C. Pillai, *J. Phys. Chem. C*, 2010, **114**, 13026

-
- ¹⁸⁸ P. Shen, C-M. Tseng, T-C. Kuo, C-K. Shih, M-H. Li, P. Chen, *Solar Energy*, 120 (2015) 345-356
- ¹⁸⁹ D. Monti, A. Ponrouch, M. Estruga, M.R. Palacín, J.A. Ayllón, A. Roig, *J. Mater. Res.*, 28 (2013) 340-347
- ¹⁹⁰ R. Fagan, D.W. Synnott, D.E. McCormack, S.C. Pillai, *Applied Surface Science*, 371 (2015) 447-452
- ¹⁹¹ D. Robert, *Catalysis Today*, 122 (2007) 20-26
- ¹⁹² N. Serpone *et al.* *J. Chem. Soc Chem Commun*, (1984) 342-344
- ¹⁹³ L. Ge, M. Xu, H. Fang, *J. Sol-Gel Sci. Techn.* 40 (2006) 65-73
- ¹⁹⁴ Y. Bessekhoud, D. Robert, J.V. Weber, *Journal of Photochemistry and Photobiology A: Chemistry*, 163 (2004) 569
- ¹⁹⁵ R. Brahim, Y. Bessekhoud, A. Bouguelia, M. Trari, *Journal of Photochemistry and Photobiology A: Chemistry*, 186 (2007) 242-247
- ¹⁹⁶ C. Kim, S.J. Doh, S.G. Lee, H.Y. Kim, *Applied Catalysis A: General*, 330 (2007) 127-133
- ¹⁹⁷ H. Wang, L. Zhang, Z. Chen, J. Hu, S. Li, Z. Wang, J. Liu, X. Wang, *Chem. Soc. Rev.*, 43 (2014) 5234-5244
- ¹⁹⁸ Y. Maruyama, H. Irie, K. Hashimoto, *J. Phys. Chem. B*, 110 (2006) 23271-23278
- ¹⁹⁹ K. Gurunathan, J.O. Baeg, S.M. Lee, E. Subramanian, S.J. Moon, K.J. Kong, *Catalysis Communications*, 9 (2008) 395-402
- ²⁰⁰ A. Kudo, Y. Miseki, *Chemical Society Reviews*, 38 (2009) 253-278